



Universität Hamburg

DER FORSCHUNG | DER LEHRE | DER BILDUNG

Calcium Release Upon Photothermal Heating of Gold Nanostars in Jurkat T Cells

DISSERTATION

for the attainment of a doctoral degree at the Faculty of Mathematics,
Informatics and Natural Sciences
in the Department of Chemistry

submitted by
Maria Pozzi

Hamburg
May 2024

These experimental studies were carried out under supervision of Prof. Dr. Wolfgang Parak at the Institute of Nanostructure and Solid-State Physics (Faculty of Mathematics, Informatics and Natural Sciences) of the University of Hamburg between November 2020 and March 2024.

Date of Submission:	29.05.2024
Thesis examiners:	Prof. Dr. Wolfgang J. Parak Dr. Florian Schulz
Date of Disputation:	20.09.2024
Disputation Committee:	Prof. Dr. Wolfgang J. Parak (Chair) Prof. Dr. Andreas H. Guse (Vice Chair) Dr. Neus Feliu Torres (Simple Member)

*The Road goes ever on and on
Down from the door where it began.
Now far ahead the Road has gone,
And I must follow, if I can,
Pursuing it with weary feet,
Until it joins some larger way,
Where many paths and errands meet.
And whither then? I cannot say.*

J.R.R. Tolkien

Contents

List of publications	II
Notations	V
Abstract	1
Zusammenfassung	3
1 Introduction	5
1.1 T lymphocytes and their role	5
1.2 Ca^{2+} storage and signaling in T cells	7
1.3 Methods to study Ca^{2+} spreading and fluctuation	12
1.4 Gold nanoparticles: SPR and photothermal characteristics	15
2 Materials and Methods	19
2.1 Synthesis of Gold Nanostars	19
2.1.1 Characterization of Gold Nanostars	20
2.2 Petri coating	21
2.3 Cell line	22
2.4 Cell treatment	22
2.5 LSM880 microscope set up	23
2.6 ICP-MS	23
2.7 Data analysis	24
3 Results	29
3.1 Characterization of T cells response to photo-thermal stimulation	29
3.1.1 Time evolution on mean intensity	29
3.1.2 Reiteration of the signal	31
3.1.3 Effects of Hoechst on cells response	31
3.1.4 Role of the laser spot dimension	32
3.1.5 Responsiveness	34
3.2 Ca^{2+} dynamics	35
3.3 Ca^{2+} depletion	42
3.3.1 Extracellular Ca^{2+} depletion: PBS without Ca^{2+} and Mg^{2+}	43
3.3.2 Extracellular Ca^{2+} depletion: Synta66	44
3.3.3 Ca^{2+} storage depletion: Thapsigargin	46
3.4 Effect of Ca^{2+} release on cell dimension	48
4 Discussion, conclusions and outlooks	51

5	In silico drug discovery	57
5.1	Introduction	57
5.2	<i>In silico</i> pipeline	57
5.3	Case study	60
A	List of GHS substances	83
	Acknowledgements	84
	Declaration of Authorship	87

List of publications

1. Liu, Z., Zimpel, A., Lächelt, U., **Pozzi, M.**, Gonzalez, M.G., Chakraborty, I., Wuttke, S., Feliu, N. and Parak, W.J., 2023. Uptake and Intracellular Fate of Fluorophore Labeled Metal–Organic-Framework (MOF) Nanoparticles. *Environment and Health*, 1(4), pp.270-277.
2. **Pozzi, M.**, Dutta S.J., Kuntze M., Schulz F., Bading J., Rüssbült J.S., Fabig C., Langfeldt M., F. Schulz, P. Horcajada, Parak W.J., Visualization of the high surface-to-volume ratio of nanomaterials and its consequences. *Submitted to The Journal of Chemical Education*.
3. Ahmed A.A.A., Alegret N., Almeida B., Alvarez-Puebla R., Andrews A.M., Ballerini L., Barrios J.J., Becker C., Blick R.H., Bonakdar S., Chakraborty I., Chen X., Cheon J., Chilla G., Coelho Conceicao A.L., Delehanty J., Dulle M., Efros A.L., Epple M., Fedyk M., Feliu N., Feng M., Fernández-Chacón R., Fernandez-Cuesta I., Fertig N., Förster S., Garrido J.A., George M., Guse A.H., Hampp N., Harberts J., Han J., Heekeren H.R., Hofmann U.G., Holzapfel M., Hosseinkazemi H., Huang Y., Huber P., Hyeon T., Ingebrandt S., Ienca M., Iske A., Kang Y., Kasiaczka G., Kim D.H., Kostarelos K., Jae-Hyun Lee J.H., Link.W., Liu S., Liu X., Liu Y., Lohr C., Mailänder V., Maffongelli L., Megahed S., Mews A., Mutas M., Nack L., Oertner T.G., Offenhäuser A., Oheim M., Otange B., Otto F., Patrono E., Peng B., Picchiotti A., Pierini F., Pötter-Nerger M., **Pozzi, M.**, Pralle A., Prato M., Qi B., Ramos-Cabrer P., Genger U.R., Ritter N., Rittner M., Roy S., Santoro F., Schuck N.W., Schulz F., Şeker E., Skiba M., Sosniok M., Stephan H., Wang R., Wang T., Wegner D.K., Weiss P.S., Xu M., Yang C., Zargarian S.S., Zeng Y., Zhao Y., Zhu D., Zierold R., Parak W.J., Towards Interfacing the Brain: How Nanotechnology Can Contribute. *In preparation*.

Secondments

1. Laboratory of prof. T. Devic at Centre national de la recherche scientifique (CNRS), Nantes (France); June - July 2021 (7 weeks).
2. Laboratory of prof. P. Horcajada at IMDEA Energy Institute, Madrid (Spain); May - July 2022 (9 weeks).
3. In silico drug discovery section with dr. A. Peña at Pharmidex, Hatfield (United Kingdom); April - May 2023 (7 weeks).

Workshops

1. "Plasmonic NPs: synthesis, characterization and applications", 15-17th March 2021 (Online).
2. "Introduction to MOFs and structural characterization of solids", 18-19th March 2021 (Online).
3. "Dissemination of research results and ethics", 5-7th July 2021 (Online).
4. "Magnetic Nanoparticles", 23-25th May 2022 (IIT - Genoa, Italy).
5. "Innovative methods for nanoMOF synthesis and characterization", 13-17th June 2022 (IMDEA - Madrid, Spain).
6. "EMAT TEM Workshop", 20-22nd June 2022 (EMAT - Antwerp, Netherlands)
7. "Drug Delivery Systems", 24-26th October 2022 (UHAM - Hamburg, Germany). Organized by **M. Pozzi**.

Notations

Acronyms and abbreviations

Abs	Antibodies
APC	Antigen Presenting Cell
ATP	Adenosine Triphosphate
AuNPs	Gold Nanoparticles
AuNSs	Gold Nanostars
cADPR	Cyclic ADP-ribose
Ca _v	Voltage-activated Ca ²⁺ channels
CRAC	Ca ²⁺ release-activated Ca ²⁺ channels
DAG	Diacyl Glycerol
DUOX2	Transmembrane Dual Oxidase 2
ER	Endoplasmic Reticulum
HN1L	Neurological Expressed 1-like Protein
ICP-MS	Inductively Coupled Mass Spectrometry
IL-2	Interleukin-2
Ins(1,4,5)P ₃	Inositol-1,4,5-triphosphate
IP ₃	Inositol-1,4,5-triphosphate
InsP ₃ R	Inositol-1,4,5-triphosphate receptor
IP ₃ R	Inositol-1,4,5-triphosphate receptor
JPT2	Jupiter Microtubule-associated Homolog 2
LL	Large Laser
LSPR	Localized Plasmon Resonance
MCU	Mitochondrial Ca ²⁺ Uniporter
MHC	Major Histocompatibility Complex
NAADP	Nicotinic Acid Adenine Dinucleotide Phosphate
NFAT	Nuclear Factor of Activated T cells
NIR	Near-InfraRed
NPs	Nanoparticles
P2X ₄	Purogenic Ion Channel
PANX1	Pannexin-1 hemichannels
PBS	Phosphate-buffered Saline
PIP ₂	Phosphatidylinositol 4,5 bisphosphate
PKC \emptyset	Protein Kinase \emptyset
PLC _{γ}	Phospholipase C γ
PM	Plasma Membrane
PMA	Phorbol 12-myristate 13-acetate
PMCA _s	PM Ca ²⁺ ATPases
ROS	Reactive Oxygen Species
RYR1/2	Ryanodine Receptor type 1/2
SEM	Scanning Electron Microscopy
SERCA _s	Sarcoplasmic/ER ATPases
SL	Small Laser
SOCE	store-operated Ca ²⁺ entry
SPR	Surface Plasmon Resonance
STIM1/2	Stromal Interaction Molecule 1/2
TCR	T cell Receptor
TEM	Transmission Electron Microscopy
TRP	Transient Receptor Potential channels
ZAP70	ζ -chain-associated protein kinase of 70 kDa

Chemical formulas

AgNO ₃	Silver Nitrate
Au	Gold
BSA	Bovine Serum Albumine
DMSO	Dimethyl Sulfoxide
HAuCl ₄	Chloroauric Acid
HCl	Chloridric Acid
HNO ₃	Nitric Acid
NaOH	Sodium Hydroxide

Abstract

Calcium, an ion abundant in various eukaryotic cells, plays a central role in numerous cellular processes. It serves as a critical signaling molecule, regulating key cellular functions such as motility, mitochondrial activity, gene expression, cell viability and proliferation. In T cells, calcium is involved in their activation, triggering the activation of several transcription factors. Because of its importance, extensive research has been conducted to elucidate the relationship between T cell stimulation, intracellular calcium dynamics, and the cellular consequences of intracellular calcium elevation. Calcium in T cells is sequestered in the extracellular space or in intracellular stores (such as the endoplasmic reticulum, mitochondria, and lysosomes). T cell activation is triggered by the binding of the T cell receptor to its co-stimulatory proteins on the surface of antigen-presenting cells. Binding initiates a signaling cascade that leads to the release of calcium from the endoplasmic reticulum and its influx from the extracellular space through calcium channels. The increase in calcium activates several second messengers, including the transcription factors of the genes involved in T cell activation.

Several methods have been developed to visualize calcium inside cells. One of the most commonly used is the use of fluorophores that are able to bind calcium. Upon binding, the fluorescence of the molecule increases. The use of these fluorophores has made it possible to monitor calcium spreading in real time and with great precision using a confocal microscope. Calcium signaling can be stimulated by different strategies, such as chemical stimulation and biological stimulation. Chemical stimulation is based on the treatment or injection of a chemical compound that triggers the release of calcium. Biological stimulation is based on the activation of the T cell receptor via co-stimulatory proteins, either attached to a bead or a surface or dissolved in a buffer.

In recent years, nanoparticles have gained more and more interest. Among them, plasmonic nanoparticles, especially gold nanoparticles, have been intensively studied because of their unique properties. In particular, they are able to interact with the light in the visible spectrum. This interaction induces an oscillatory motion of the surface electrons, called surface plasmon resonance. When the gold nanoparticles interact with the appropriate wavelength they are able to convert the energy absorbed from light into heat in a process called photothermal heating. Among the different shapes that nanoparticles can have, the star-shaped gold nanoparticles are the ones that show the highest efficiency as photothermal vectors due to their sharp tips in which surface plasmon resonance can better localize. Gold nanostars were used by Zhu and coworkers to induce calcium signaling and release calcium from lysosomes in two cancer cell lines.

In the work presented in this dissertation, calcium release was induced in the Jurkat T cell line by exploiting the photothermal property of gold nanostars. After the treatment with the nanostars, Jurkat T cells were irradiated with a laser at the appropriate wavelength. The gold nanostars, localized in the endolysosomes, increased

in temperature. The temperature increase was transmitted to the nanoparticles' surrounding, causing the formation of a transient pore in the lysosomal membrane, leading to the release of calcium. The calcium released from the lysosome induces the global calcium signaling inside the cell. The use of a calcium-binding fluorophore made it possible to spatially and temporally visualize and study the calcium. By conducting statistical analysis and assessing various conditions, the existence of a maximum peak was confirmed, which exhibits considerable variability in intensity, while the time to reach the peak remained consistent across each condition tested. While these findings imply that the method proposed in this paper is a promising approach for studying calcium release and spreading, offering a simpler and more precise alternative to biological or chemical methods, further research is necessary to fully comprehend the cellular effects of photothermal heating.

Zusammenfassung

Calcium, ein in verschiedenen eukaryontischen Zellen reichlich vorhandenes Ion, spielt bei zahlreichen zellulären Prozessen eine zentrale Rolle. Es dient als entscheidendes Signalmolekül, das wichtige Zellfunktionen wie Motilität, Mitochondrienaktivität, Genexpression, Zellebensfähigkeit und Proliferation reguliert. In T-Zellen ist Calcium an ihrer Funktion beteiligt und löst die Aktivierung verschiedener Transkriptionsfaktoren aus. Aufgrund seiner Bedeutung wurden umfangreiche Forschungsarbeiten durchgeführt, um die Beziehung zwischen der Stimulation von T-Zellen, der intrazellulären Calciumdynamik und den zellulären Folgen der intrazellulären Calciumerhöhung zu klären. Calcium in T-Zellen wird im extrazellulären Raum, oder in intrazellulären Speichern (wie dem endoplasmatischen Retikulum, Mitochondrien und Lysosomen) sequestriert. Die Aktivierung der T-Zellen wird durch die Bindung des T-Zell-Rezeptors an seine Co-Stimulationsproteine auf der Oberfläche der Antigen-präsentierenden Zellen ausgelöst. Die Bindung setzt eine Signalkaskade in Gang, die zur Freisetzung von Calcium aus dem endoplasmatischen Retikulum und zum Einstrom von Calcium aus dem extrazellulären Raum über Calciumkanäle führt. Der Calciumanstieg aktiviert mehrere Botenstoffe, darunter die Transkriptionsfaktoren der Gene, die an der Aktivierung der T-Zellen beteiligt sind.

Es wurden mehrere Methoden entwickelt, um Calcium im Zellinneren sichtbar zu machen. Eine der am häufigsten verwendeten Methoden ist die Verwendung von Fluorophoren, die Calcium binden können. Bindet das Fluorophor an Calcium, erhöht sich die Fluoreszenz des Moleküls. Die Verwendung dieser Fluorophore hat es ermöglicht, die Ausbreitung von Calcium mit Hilfe eines konfokalen Mikroskops in Echtzeit und mit großer Präzision zu verfolgen. Die Calciumsignalkaskade kann durch verschiedene Strategien stimuliert werden, wie z. B. durch chemische- und biologische Stimulierung. Die chemische Stimulation basiert auf der Injektion einer chemischen Verbindung, die die Freisetzung von Calcium auslöst, oder einer chemischen Behandlung, die das selbige erzielt. Die biologische Stimulierung beruht auf der Aktivierung des T-Zell-Rezeptors durch kostimulierende Proteine, die entweder an ein Bead, oder eine Oberfläche gebunden sind, oder in einem Puffer aufgelöst vorliegen.

In den letzten Jahren haben Nanopartikel immer mehr an Interesse gewonnen. Unter ihnen wurden plasmonische Nanopartikel, insbesondere Goldnanopartikel, aufgrund ihrer einzigartigen Eigenschaften intensiv untersucht. Sie sind insbesondere in der Lage, mit dem Licht im sichtbaren Spektrum zu interagieren. Diese Wechselwirkung führt zu einer oszillierenden Bewegung der Oberflächenэлектроnen, der sogenannten Oberflächenplasmonenresonanz (surface plasmon resonance). Wenn diese Gold-Nanopartikel mit der entsprechenden Wellenlänge interagieren, können sie die vom Licht absorbierte Energie in Wärme umwandeln, was als photothermische Erwärmung bezeichnet wird. Unter den verschiedenen Formen, die Nanopartikel haben können, sind sternförmige Gold-Nanopartikel diejenigen, die aufgrund ihrer scharfen Spitzen, in denen sich die Oberflächenplasmonenresonanz

besser lokalisieren kann, die höchste Effizienz als photothermische Vektoren aufweisen. Goldnanosternchen wurden von Zhu und Mitarbeitern verwendet, um in zwei Krebszelllinien Calciumsignale zu induzieren und Calcium aus Lysosomen freizusetzen.

In der in dieser Dissertation vorgestellten Arbeit wurde die Calciumfreisetzung in der Jurkat-T-Zelllinie durch Ausnutzung der photothermischen Eigenschaft von Goldnanosternen induziert. Nach der Behandlung mit den Nanosternen wurden die Jurkat-T-Zellen mit einem Laser der entsprechenden Wellenlänge bestrahlt. Die Goldnanostars, die in den Endolysosomen lokalisiert waren, erhöhten ihre Temperatur. Der Temperaturanstieg wurde auf die umgebenden Nanopartikel übertragen und führte zur Bildung einer vorübergehenden Pore in der lysosomalen Membran, was zur Freisetzung von Calcium führte. Das aus dem Lysosom freigesetzte Calcium löst die globale Calcium-Signalisierung innerhalb der Zelle aus. Die Verwendung eines calciumbindenden Fluorophors ermöglicht es, das Calcium räumlich und zeitlich zu visualisieren und zu untersuchen. Durch statistische Analysen und Bewertung verschiedener Bedingungen wurde die Existenz eines maximalen Peaks bestätigt, der eine beträchtliche Variabilität in der Intensität aufweist, während die Zeit bis zum Erreichen des Peaks bei jeder getesteten Bedingung gleich blieb. Diese Ergebnisse deuten darauf hin, dass die in dieser Arbeit vorgeschlagene Methode ein vielversprechender Ansatz zur Untersuchung der Calciumfreisetzung und -ausbreitung ist und eine einfachere und präzisere Alternative zu biologischen oder chemischen Methoden bietet.

Chapter 1

Introduction

In this introductory chapter, the concepts needed to better comprehend the work are explained in details. The chapter begins by describing T lymphocytes and elucidating their diverse functions within the immune system. Following that, the calcium storage and signaling within T cells is explored, uncovering the molecular mechanisms governing their activation and function. Various methodologies utilized in studying calcium dynamics within these cells are scrutinized, shedding light on techniques such as fluorescence imaging and electrophysiological tools. Lastly, the chapter concludes with an examination of gold nanoparticles exploited in the presented work, elucidating their distinct surface plasmon resonance (SPR) and photothermal characteristics.

1.1 T lymphocytes and their role

T lymphocytes, also known as T cells, are circulating white blood cells that play a pivotal role in the adaptive immunity, which is responsible for mounting a highly specific and coordinated immune response against pathogens and other foreign substances. T cells are able to specifically recognize an antigen, maintaining a memory of a previously encountered pathogen, while at the same time lacking self-reactivity [1, 2].

Both B and T lymphocytes come from a common lymphoid precursor which is produced in the bone marrow. T cells differ from B cells because they express on their surface the T cell receptor (TCR). These lymphocytes undergo maturation inside the thymus, a gland located in the chest between the lungs [3]. At the beginning of their maturation T cells express on their surface neither CD4 or CD8 glycoproteins coreceptor, that will later be used as markers to identify their functional specialization. During the maturation, T cells migrate throughout the thymus and undergo to a two-step selection: positive and negative [4]. These processes are needed to select active cells while removing autoreactive ones. After the positive selection, T lymphocytes express either CD4 or CD8 glycoprotein and are reactive to both foreign and self-antigens. The negative selection induces the apoptosis of self-reactive lymphocytes and protect the host from autoimmune diseases. After maturation the naïve T cells migrate through the secondary lymphoid organ (spleen, lymph nodes and mucosal-associated lymphoid tissue) where they are then activated in presence of a pathogen.

The ability of T lymphocytes to recognize a specific antigen is conveyed by the T cell receptor. TCR is a transmembrane heterodimer protein complex that is encoded

by four sets of genes. The recombination of these genes, during T cells development, is responsible for TCR specificity and commits the cell to a precise antigen for its entire lifetime. The TCR is able to recognize antigens presented as processed peptides and loaded on a heterodimer transmembrane protein called the major histocompatibility complex (MHC), expressed on the antigen presenting cell (APC) plasma membrane (PM) [5]. The link between TCR and MHC starts the activation of the T cells. However, the bonding between TCR and MHC is not sufficient to complete the activation: a co-stimulatory signal is also required. This signal is obtained with the interaction of other surface proteins on both T cells and APCs (i.e. CD28 on T cells and B7.1 on APCs) that strengthen and prolong the contact between the two cells, creating the immunological synapse [6]. After the co-stimulation, T cells activation is carried out only in the presence of interleukin-2 (IL-2), a signaling protein that is produced and secreted by activated T cells themselves. Without the presence of IL-2, T cells enter in a state of anergy where they became unresponsive to further stimulation [7]. Activated cells start to clonally expand amplifying the number of lymphocytes specific to the invading pathogens [8]. As aforementioned, the functional specialization of the T cells depends, among other things (like the cytokines present in the microenvironment and the antigen concentration), on the glycoprotein expressed on their surface. Upon activation, cells that express CD8 glycoprotein are able to produce cytotoxic proteins (such as perforin and granzymes) and secrete them to kill a target cell. CD8⁺ T cells are therefore known as cytotoxic T cells [5]. On the other hand, CD4⁺ T cells can differentiate into multiple different specialized effector cells [9]. The various cellular subsets can be categorized based on the production of distinct cytokines and effector functions. CD4⁺ activated T cells have two major roles in immune response: help to mount it or regulates it. The lymphocytes that help to mount the immune response are called helper T cells. The principal helper T cells are: Th1, Th2 and Th17. Th1 cells are associated with organ-specific autoimmunity and are involved in the elimination of intracellular pathogens through macrophages activation [10]. Th2 cells supports the activation of the immune response against the extracellular parasites facilitating B cell antibody responses [10]. Due to this interlink with B cells, Th2 cells are also involved in induction and persistence of asthma and other allergic diseases [11]. Lastly, Th17 cells are involved not only in the mounting of the immune response against extracellular bacteria and fungi, but also in the development of autoimmune diseases [12, 13, 14]. T cells CD4⁺ involved in the regulatory processes of the adaptive immunity are called regulatory T cells or Treg. Their role is to maintain the immunologic tolerance to self and foreign antigens by negatively regulate the immune response after the clearance of the pathogens [15, 16].

After the dramatic clonal expansion as resulting from the activation of naïve T cells, the cells undergo to an impressive shrinking of the population induced by apoptosis following the eradication of the infection. As a result, just a few are able to survive. These surviving T cells are known as memory T cells. Memory T cells are divided in different subsets that can be found inside the lymphoid or circulating in peripheral tissue. The main function of these cells is to remember a pathogen and, when the infection reoccur, arise the immune response faster, proliferating and creating a new round of effector cells [17, 18].

T cells are small, round-shaped cells with an average dimension of 5-10 μm . A large part of the cell is filled by the nucleus, that present a singular bean-like shape (**Figure 1.1A**). On the surface numerous flexible protrusions of the plasma membrane called microvilli can be found (**Figure 1.1B**). The role of the microvilli is not completely understood but they are involved in the cell extravasion towards the site of infection and play a key role in the antigen recognition by strengthening the inter-

action with APCs [19].

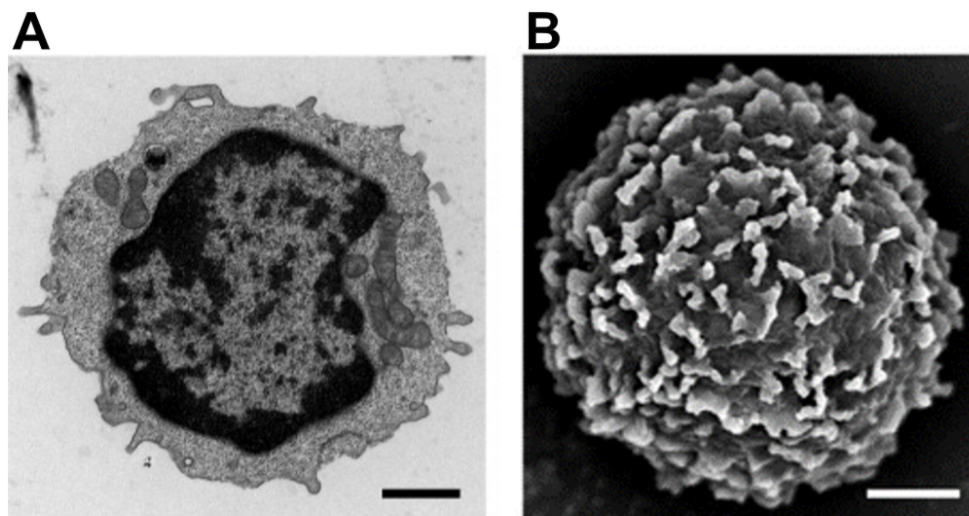


Figure 1.1: Transmitted electron microscopy (A) and Scanned electron microscopy (B) of T lymphocyte. Scale bar: 2 μm . The image was adapted from reference [20].

One of the most commonly used immortalized T cell lines to study the TCR activation and signaling cascade is Jurkat T cell line [21]. In the early 1980s, the cell biologists used primary cells derived either from human or murine source. Over time, the demand for immortalized cell lines, capable of enduring *in vitro* conditions for extended periods of time and to be genetically modified for studying their functionality, increased significantly. The solution came when John Hansen, while screening various leukemic cell lines [22, 23], discovered that Jurkat (cells derived from the peripheral blood of a 14 years old male acute leukemia patient) exhibited a robust production of IL-2 when appropriately stimulated [24]. From the Jurkat cell lines, multiple randomly mutagenized cell lines were created and used to better understand TCR and T cells activation. Despite some drawbacks (especially regarding the profile of expression of few proteins), Jurkat T cells are still used in immunological labs today and, over few decades, helped to deepen our knowledge of T cells functionality.

1.2 Ca^{2+} storage and signaling in T cells

For a wide range of eukaryotic cells, not only human and animal but also plant cells, calcium is a key signaling ion [25]. Calcium signaling pathways are involved in numerous pivotal cell functions [26], such as: motility and contraction [27], mitochondrial function [28], viability and cell proliferation [29], gene transcription and signaling [30]. In general, when a cell is stimulated, there is an increase in intracellular calcium concentration that lasts until the stimulus ends. The calcium level then returns to background. The extent of this increase depends on the intensity and duration of the stimulus. It is important to notice that, although the increase of intracellular calcium is essential to carry on cellular response, the amount of Ca^{2+} released must remain under a defined threshold. Large increase in calcium can lead to unwanted side effects like reactive oxygen species (ROS) production, organelle remodeling and mitochondria permeability, resulting in cell apoptosis [31, 32]. While

an excess of calcium in the cell has catastrophic effects, an excessive decrease also affects the behavior of the cell and its survival [33, 34]. Since this ion holds a great importance in the cells' activity, its concentration must be precisely controlled by the cell. The calcium concentration in the cytosol of cells ranges between 50 to 100 nM, while the extracellular concentration is much higher, around 1-2 mM. This imbalance in concentration allows the maintenance of the plasma membrane potential to approximately -55 mV. Calcium can also be stock inside intracellular storage. The main storage sites in the cells are: endoplasmic reticulum (ER), mitochondria and endolysosomes. All these organelles can store different concentrations of calcium and therefore are differently involved in its release in the cytosol. ER contains 300 μM -1 mM calcium, mitochondria 0.1 nM-1mM and endolysosomes 400-600 μM .

The fine tuning of calcium concentration inside the cell is mediated by a large range of transmembrane proteins, called calcium channels [35]. Calcium channels can be found ubiquitously in the cells and allow the movement of the ions across the cell membranes. These channels can react to different stimuli. For example, the different concentration of the ion across a membrane is a chemical stimulus. In the presence of a concentration imbalance straddling a cell membrane, the channels can allow the movement of the Ca^{2+} following its gradient. Another stimulus is the change in the voltage, especially of the plasma membrane (PM). The calcium channels that respond to this stimulus are called voltage-activated Ca^{2+} channels (Ca_V channels). Ca_V channels are mainly located at the PM and are generally associated with excitable cells like muscle cells [36] and neurons, nevertheless they also take part in T cells functions and activation [37, 38]. Lastly, highly specialized channels can be opened by the binding to a specific ligand (i.e. neurotransmitters) or when a physical stimulus, such as stretch or increase in temperature, occurs. When the Ca^{2+} ions have to be transported against the electrochemical gradient, the ion pumps use energy, in the form of adenosine triphosphate (ATP), to extrude them. Two crucial calcium ion pumps are PM Ca^{2+} ATPases (PMCA) [39, 40] and sarcoplasmic/ER ATPases (SERCA) [41], that can be found at the PM and ER respectively. These pumps pull out the calcium from the cytosol into the extracellular space (PMCA) or the ER (SERCA). Taken together these ion channels and pumps are essential to maintain calcium homeostasis inside the cell.

The role of calcium in T cells has been extensively studied because of its link with their activation [42]. Upon engagement of the TCR by the MHC, the intracellular domains of the receptors (ITAMs) are phosphorylated leading to the activation of ζ -chain (TCR) associated protein kinase 70 (ZAP70) and phospholipase $\text{C}\gamma 1$ ($\text{PLC}\gamma 1$). $\text{PLC}\gamma 1$ hydrolyses phosphatidylinositol 4,5 bisphosphate (PIP_2) to produce inositol-1,4,5-triphosphate ($\text{Ins}(1,4,5)\text{P}_3$ or IP_3) and diacyl glycerol (DAG). Both IP_3 and DAG act as second messengers. DAG activates two major downstream pathways involving Ras protein and protein kinase θ ($\text{PKC}\theta$) [43]. Both these pathways lead to the activation of transcription factors: Ras protein mediated pathway activates AP-1 [44] while $\text{PKC}\theta$ pathway activates NF_κB [45]. AP-1 and NF_κB transcriptional factors are involved in the activation of various genes involved in: cell growth (AP-1), cell functions, survival and homeostasis (NF_κB). On the other hand, IP_3 binds to its receptor (InsP_3R or IP_3R located on the ER) triggering the release of Ca^{2+} from the ER store (Figure 1.2).

The depletion of Ca^{2+} from ER, activates the ER Ca^{2+} sensors stromal interaction molecule 1 (STIM1) and STIM2. STIM1 and STIM2 are localized on the ER and possess a luminal Ca^{2+} -binding domain that acts as a sensor of the ion concentration within the ER. IP_3 -induced calcium release triggers STIM1 clustering and movement to junctional zones where the ER and PM are in close contact, typically within 10-25 nm. When calcium release is modest, STIM2 is activated, whereas when release is

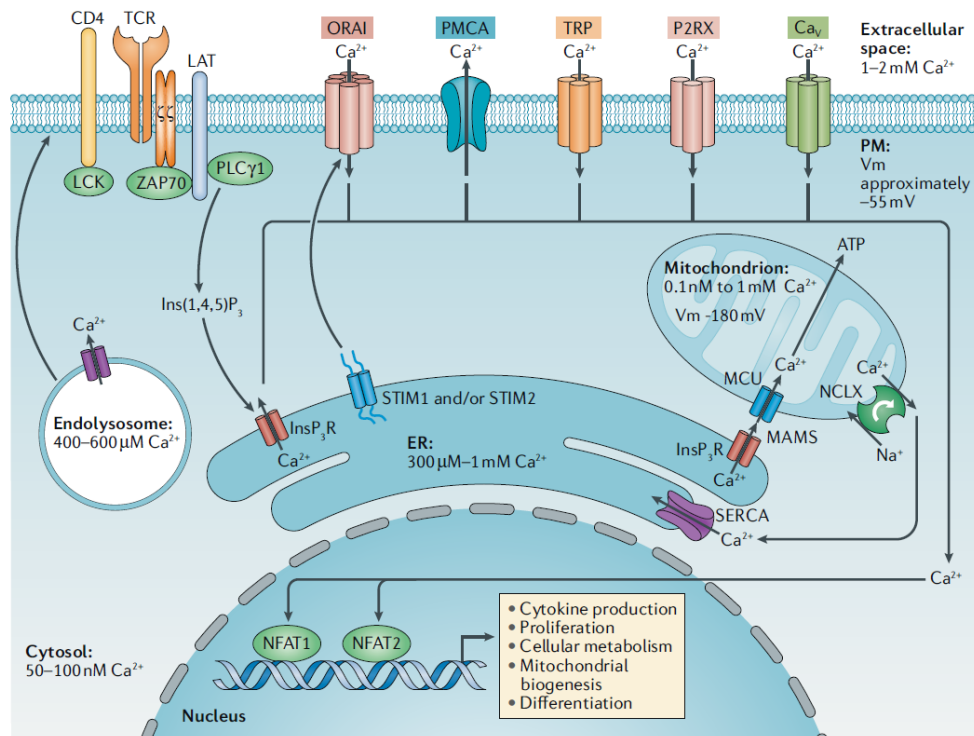


Figure 1.2: Calcium signaling in T cells. Stimulation of T cell receptor (TCR) leads to the activation of phospholipase $\text{C}\gamma$ ($\text{PLC}\gamma$). $\text{PLC}\gamma$ produces inositol-1,4,5-triphosphate ($\text{Ins}(1,4,5)\text{P}_3$) that binds its receptor (InsP_3R) on the surface of the endoplasmic reticulum (ER). The binding induces the release of Ca^{2+} from ER and the activation of stromal interaction molecule 1 and 2 ($\text{STIM1}/2$). $\text{STIM1}/2$ activates ORAI1 localized at the plasma membrane (PM) and stimulates store-operated Ca^{2+} entry (SOCE). SOCE activates Calmoduline, which in turn activates nuclear factor of activated T cells 1 and 2 ($\text{NFAT1}/2$). $\text{NFAT1}/2$ translocate in the nucleus and transcribe the genes involved in cytokine production, proliferation, cellular metabolism, mitochondrial biogenesis and differentiation. On the PM are located other channels involved in the Ca^{2+} influx during T cells activation: non-selective transient receptor potential (TRP) channels, purinergic ionotropic receptors (P2RXs) and voltage-activated Ca^{2+} (Ca_V) channels. The Ca^{2+} released by InsP_3R is uptaken by mitochondria via mitochondrial Ca^{2+} uniporter (MCU). InsP_3R and MCU co-localized at a contact site called mitochondria-associated membranes (MAMs). In mitochondria, Ca^{2+} is used to produce ATP and to uptake Na^+ via mitochondrial $\text{Na}^+/\text{Ca}^{2+}/\text{Li}^+$ exchanger (NCLX). PM Ca^{2+} ATPases (PMCA) and sarcoplasmic/ER Ca^{2+} ATPases (SERCAs) maintain Ca^{2+} homeostasis pumping the ions in the extracellular space and in lumen of ER respectively. Lat, linker for activation of T cells; V_m , membrane potential; ZAP70, ζ -chain-associated protein kinase of 70 kDa. Image from reference [42].

more substantial, STIM1 is activated [46]. At the junction site, STIM1 interacts with ORAI1 , a calcium channel situated at the PM, forming a high selective ion channel complex that allows the entry of the extracellular calcium to replenish the stores [47]. This pathway of calcium entry is known as store-operated Ca^{2+} entry (SOCE), while the channels (STIM1 and ORAI1) involved are known as Ca^{2+} release-activated Ca^{2+}

(CRAC) channels [48]. SOCE activates the second messenger calmodulin. Calmodulin is a Ca^{2+} -sensing protein [49] that is able to activate different downstream enzymes and transcription factor, the most significant of which are the isoforms of the nuclear factor of activated T cells (NFAT1 and 2) [50]. Once activated by Calmodulin, NFAT translocates inside the nucleus and start the transcription of different genes involved in: cytokines production, proliferation, mitochondrial biogenesis, cellular metabolism and differentiation.

The global rise of the intracellular Ca^{2+} concentration induced by SOCE activates not only NFAT and other transcriptional factors (like NF_κB and AP-1) but also mitochondrial metabolism [51] and cytoskeletal mobilization [52].

Mitochondria have a role in the calcium storage and buffering. On the surface of these organelles it is present the mitochondrial Ca^{2+} uniporter (MCU). MCU moves the calcium ions from the cytoplasm across the inner mitochondrial membrane [53]. The removal of the Ca^{2+} , carried out by MCU, has two major effects. The first is to avoid the inactivation of the IP_3R , as a negative feedback of the calcium release itself. The second is to reduce the amount of Ca^{2+} available to SERCAs to replenish the ER. Taken together these two events induce the need to acquire calcium from the extracellular space and thus to the opening of CRAC channels (STIM1 and ORAI1) [54, 55]. In addition, increasing the concentration of calcium ions inside the mitochondria activates calcium-dependent enzymes involved in the Krebs cycle and complexes involved in the electron transport chain, resulting in enhanced ATP production [56, 57]. The newly synthesized ATP plays also a role in Ca^{2+} influx thus contributing in amplifying the global signaling and T cells activation [58, 59, 60]. ATP is transported from the mitochondria into the cytosol, where a small amount is then released outside the cell through pannexin-1 hemichannels (PANX1) [61]. The released ATP triggers the activation of P2X4 and P2X7 purinergic ion channels [62, 63, 64] in a autocrine way [65], causing an influx of calcium ions, thereby increasing its intracellular concentration (**Figure 1.3**). In turn, the increased production of ATP and the presence of calcium influence the production of reactive oxygen species (ROS) [66]. Interestingly, moderate levels of ROS are necessary for optimal T cell activation, as they are required for cytokine production and metabolic functions [67]. On the other hand, excessive levels of ROS have the opposite effect by blocking the activation of the transcription factor NFAT and consequently the production of IL-2 [68].

Calcium is able to regulate the cytoskeleton thanks to capping proteins (like gelsolin [69]) that are activated by the increasing in the ion concentration. After the activation of TCR and the release of Ca^{2+} , a rapid (within seconds) rearrangements of actin and the microtubules towards the region of contact of T cell and APC can be observed. These reorganizations help, over time, to translocate all the necessary proteins and organelles to create the immunological synapse. A continuous stimulation stabilize the immunological synapse and allow the cytoskeleton to help the clustering of STIM1 and ORAI1, resulting in SOCE. Moreover, the microtubules are able to relocate mitochondria in the proximity of the synapse where they will suppress Ca^{2+} -dependent inactivation of CRAC channels, and thereby prolong their activity reinforcing the entry of calcium [52].

As discussed in detail above, a global increase in intracellular calcium concentration is pivotal for T cells activation. The in-depth study of this global signal has shed light on its origin as well as on the Ca^{2+} behavior during cell resting state. In several different cell types (such as neuronal [70], cardiac [71] and T cells [72]), it has been observed that, not only in stimulated but also in unstimulated state, calcium does not remain confined in the store or outside the cell, but it is released in the cytosol in the form of so-called Ca^{2+} microdomains [73]. Ca^{2+} microdomains can be described as small and localized calcium signals that are usually transient and fluctuating. Al-

though at first glance these signals could be regarded as noise, they can play a crucial role in originating a global increase in intracellular calcium. It is important to underline that not all the microdomains are able to trigger the global signaling activation and they can simply be physiological fluctuation in calcium density inside the cell. Usually the microdomains localize in close proximity with a calcium channel or a cluster of channels and, therefore, can be found near the plasma membrane or the ER. Interestingly, Ca^{2+} ions can poorly diffuse in the cytosol in a range of approximately 200 nm due to cytosols' buffering capacity [74, 75, 76]. Therefore, when the Ca^{2+} ions are actively involved in the T cell activation, a second messenger is needed for the Ca^{2+} to be able to activate more distant calcium release and/or entry channels and arise a global calcium signaling [77].

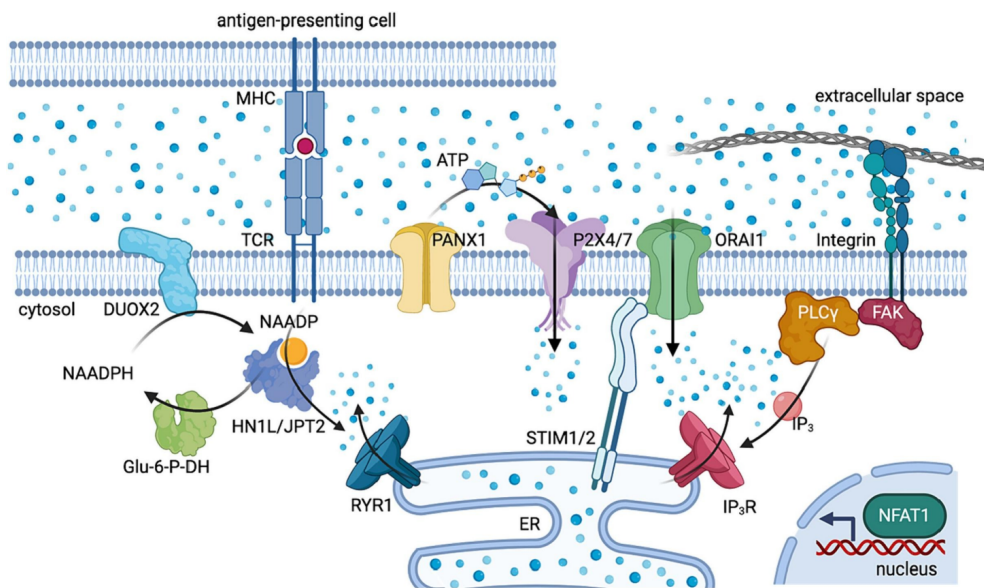


Figure 1.3: Formation of the Ca^{2+} microdomains upon TCR binding to MHC. Upon activation of T cell receptor (TCR) via binding major histocompatibility complex (MHC), dual oxidase 2 (DUOX2) generates nicotinic acid adenine dinucleotide phosphate (NAADP) by NAADPH. NAADP binds to neurological expressed 1-like protein (HN1L) also called Jupiter microtubule-associated homolog 2 (JPT2) and the complex interacts with ryanodine receptor type 1 (RYR1) on the endoplasmic reticulum (ER). RYR1 is activated and releases Ca^{2+} in the cytosol evoking the Ca^{2+} microdomains. The microdomains stimulate further influx of calcium into the cytosol via activation of ORAI1 through stromal interaction molecule 1/2 (STIM1/2). Phospholipase $C\gamma$ (PLC γ), here represented linked to integrin, produces inositol-1,4,5-triphosphate (IP_3). IP_3 interacts with its receptor IP_3R further increasing the release of calcium into the cytosol and store-operated Ca^{2+} entry (SOCE). Moreover, the release of ATP in the extracellular space via pannexin-1 hemichannels (PANX1) activates P2X4/7. P2X4/7 channels open and allow the influx of more calcium ions. The global calcium signaling results in the activation and translocation of the nuclear factor of activated T cells (NFAT1), leading to the complete activation of T cells. NAADP is restored to its oxidized form, NAADPH, by glucose-6-phosphate dehydrogenase (Glu-6-P-DH). Image from ref. [78]

The second messengers involved in the microdomain formation are three: nicotinic acid adenine dinucleotide phosphate (NAADP), IP_3 and cyclic ADP-ribose (cADPR)

(**Figure 1.3**). After TCR activation by binding MHC, the transmembrane dual oxidase 2 (DUOX2) is activated and it generates NAADP by oxidating its reduced form NAADPH [79]. NAADP reaches its maximum concentration inside the cell 10 sec after TCR activation. NAADP binds either to the binding protein neurological expressed 1-like protein (HN1L) also called Jupiter microtubule-associated homolog 2 (JPT2) [80, 81] or Lsm12 [82]. Once linked to either HN1L/JPT2 or Lsm12, NAADP can binds different calcium channels: two-pore channel 1 (TPC1) and 2 (TCP2) [83, 84], localized on the endolysosomes, and/or ryanodine receptor type 1 (RYR1) [85, 86], localized on the ER. Both TCP1/2 and RYR1, once bound to NAADP complex, open to release calcium in the cytosol creating the calcium microdomains exploiting Ca^{2+} induced Ca^{2+} release mechanism. NAADP is the first second messenger to be produced, IP_3 and cADPR are produced later on, reaching their peak in concentration after 2-5 min and 10 min after TCR activation. IP_3 is produced, as already described above, by $\text{PLC}\gamma$ and it activates IP_3R on the ER inducing the release of Ca^{2+} and the subsequent activation of the CRAC channels inducing SOCE. cADPR binds an isoform of RYR called RYR3. Both IP_3 and cADPR are needed to sustain the increase of intracellular Ca^{2+} and, therefore, inducing a global signaling. NAADP, on the other hand, acts as a co-agonist of them bringing the cell out of its pre-activated state through the rise of calcium microdomains. When Ca^{2+} microdomains are actively involved in T cells activation, they present the following defined features. They are localized at the site of stimulation and they present an amplitude of approximately 260-420 nM [86]. Moreover, they display a spatial spread of circa 450 nm [85, 86]. Ca^{2+} microdomains last few seconds before merging into the global Ca^{2+} signal and became indistinguishable.

1.3 Methods to study Ca^{2+} spreading and fluctuation

Given the importance of calcium in T-cell function, its release, fluctuation, and spreading have been studied in detail, and numerous techniques have been developed over time. The first step to be undertaken in the study of calcium fluctuation *in vitro* is to elicit its intracellular increase. To accomplish that, two different approaches can be exploited.

The first one is to induce the T cell activation while the second is to directly stimulates the influx of calcium. Over the years different methods have been developed to activates T cells. The co-culture method involves the culturing APCs loaded with an antigen and naïve T cells [87]. This is a more physiological approach, nevertheless it requires the preparation of APCs prior the addition of T cells and an appropriate antigen. Another method is antibodies stimulation. This method exploits antibodies (Abs) that target the co-stimulatory glycoproteins CD-3 and CD-28, present on the surface of the T cells, that are directly involved in T cells activation. The binding of the antibodies with their respective targets stimulates the lymphocytes. Interestingly, the antibodies can be delivered to the cells through different strategies. Anti-CD3 and anti-CD28 antibodies can be administered to T cells as a solution [88]. Even though antibodies solution protocol is simpler than the others listed here, it often requires additional co-stimulatory signals to induce a proper activation and provides less cellular expansion. Another strategy is to coat a plate with the antibodies and, subsequently, plate the T cells [89]. The coated plate strategy has the advantage of controlling the interaction of the cells with the antibodies avoiding over stimulation that can lead to apoptosis and cell population failures. On the other hand, this protocol is suitable only for small scale experiments and it is non-scalable. The last antibodies stimulation methods is based on magnetic beads. The beads mimic the APCs

and are coated with Abs via covalent bonds. The beads are mixed with the T cells to induce activation [88, 90, 91]. When APC- and antibodies-based methods are not available, chemical compounds can be exploited. The most common pharmacological method to activate T cells is based on the administration of phorbol 12-myristate 13-acetate (PMA) in combination with the ionophore ionomycin [92, 93]. PMA and ionomycin synergistically activates PKC while, at the same time, increasing the intracellular calcium, leading to the activation of the T cell.

An alternative approach is to directly induce an increase of intracellular calcium, without necessary engaging TCR or co-stimulatory proteins and activating T cells. This goal is achieved mainly by treating the cells with compounds able to interact with different players involved in calcium signaling. It has been shown that adding ATP to T cells induces the activation of P2X_{4/7} (as explained in **Section 1.2**) causing the influx of calcium from the extracellular space [94]. Similarly, the intracellular injection of messengers physiologically involved in the calcium signaling pathway, such as IP₃, NAADP [95] and cADPR [96], leads to the increase in the ion concentration. The same result can be obtained using drugs such as ion channels modulators, like amiodarone, ioxapine and furosemide [97]. Recently, also nanoparticles have been used to elicit an increase of calcium. Calcium-based nanoparticles were exploited to reinforce the effect of immunostimulants in the acidic tumor microenvironment [98, 99]. Nanoparticles not based on calcium can also be used for this purpose, taking advantage of their physico-chemical properties. For example, the capacity of plasmonic nanoparticles to increase their temperature if stimulated with light has been utilized to increase the calcium concentration inside HeLa cells [100] and neurons [101].

To be able to visualize qualitatively and quantitatively the calcium flow, researchers have mainly used two techniques: patch clamp and confocal microscopy. Patch clamp allows to study and record the ion currents across the phospholipidic membranes. As described in **Section 1.2**, the voltage of the plasma membrane in resting T cell is around -55 mV and it is strictly linked to the intracellular concentration of several ions including Ca^{2+} . Upon cellular activation, the increasing concentration of Ca^{2+} induce a flow of ions across the plasma membrane leading to its hyperpolarization [102, 103]. The hyper- and depolarization can be detected and studied with patch clamp. Confocal microscopy, on the other hand, allows the real time and spatially resolved visualization of calcium and gives useful insight not only on the spreading of the signal but also on the calcium behaviors during cells' resting state. To be able to image calcium, various Ca^{2+} indicators were developed over time [104, 105]. Many of the most widely used dyes in recent years have been developed from calcium chelators, such as EGTA, APTRA and BAPTA, to which fluorophores have been incorporated [106, 107, 108]. The fluorophore groups carry a Ca^{2+} -binding domain that, in the presence of calcium, induces conformational changes capable of modifying the absorption and emission of the molecule. Currently, a large collection of fluorescent dyes is available that differs in calcium dissociation constant, binding kinetics, photostability, intracellular localization, fluorescence quenching characteristics, and excitation and emission wavelength [109]. It is important to note that the binding kinetics of the dye may affect the spatial resolution of the Ca^{2+} signal [110, 111, 112]. Since calcium signaling can often be localized and transient, the binding kinetics of the dye must be fast enough to resolve these signals with sufficient temporal precision [110]. Thus, dyes with slow binding kinetics are not suitable for the detection of calcium microdomains and can lead to inaccuracies. Moreover, the efficiency of these dyes is influenced by pH, temperature, protein binding and presence of other ions like Mg^{2+} [113, 114].

Ca^{2+} fluorescent dyes are divided in two categories: ratiometric and single wave-

length dye. Ratiometric dyes, such as Fura-2 [108, 115], Fura-Red [116] and Indo-1 [108], show a spectral shift in either the excitation or emission wavelength upon Ca^{2+} binding, often in conjunction with a change in fluorescence intensity. Because the Ca^{2+} -free and Ca^{2+} -bound forms can be clearly distinguished, these dyes can be used to measure calcium in the presence of uneven dye loading, dye leakage, photobleaching, compartmentalization, or cell thickness [117]. The main disadvantages of their use include increased photodamage to the cells and increased cellular autofluorescence. Unlike ratiometric dyes, single wavelength Ca^{2+} dyes don't show a shift in emission wavelength, but rather a brighter emission signal. However, the increase is directly correlated to the dye concentration, making quantification of Ca^{2+} dyes less accurate compared to ratiometric dyes. Nevertheless, quantification of calcium is still possible by loading a cell with a mixture of ratiometric and single wavelength dyes (such as Fluo-3 or Fluo-4 AM and Fura-Red) [118, 119]. Despite their unreliability in quantification, these dyes have significantly improved the fluorescent imaging not only of the global calcium signal but also of calcium microdomains. Among single wavelength dyes, Fluo-4, in its form with the addition of an acetate ester (AM) group, is of particular interest. Fluo-4 is a di-fluoro analog of Fluo-3 dye and has very similar spectral properties with a maximum absorption and emission at 494 and 516 nm, respectively [113]. Fluo-4 is brighter and more stable analogue of the dye Fluo-3. When bound to Ca^{2+} , its fluorescence increases of 100-fold allowing the use of a lower working concentration and shorter loading times. Fluo-4 is also been linked to AM group to improve its cell permeability. AM group hides the charges of the dye and thus made it more lipophilic. Once in the cytosol, the cytoplasmic esterases hydrolyse the AM group trapping the molecule inside the cell. In addition to chemical indicators, there are also biological indicators based on biosensors and fusion proteins, known as genetically encoded calcium indicators (GECIs) [120, 121, 122]. These indicators can be produced in a specialized organism (bacteria, insect or human cells) and then administered to the target cell or produced directly by the target cell into which the gene of interest is inserted. The main advantages of using these markers are their stability over long periods (even weeks) and their precise localization within the cell. However, they are more complicated to use and produce than chemical markers. In recent years, nanoparticles have been exploited to improve calcium sensing and enhancing the imaging of pre-existing dyes by improving their ability to sense high Ca^{2+} concentration (higher than 100 μM) [123]. However, nanoparticles are not commonly used and a lot needs to be studied to fully comprehend their potential in this field.

The Ca^{2+} signaling is generated by different players (such as cellular stores, plasma membrane channels, second messengers,... etc), as explained in detail in **Section 1.2**. Identifying the contribution of each of these players has shed light on the rise and maintenance of Ca^{2+} signaling. To achieve this, the player's contribution must be isolated from the global signaling. This can be obtain modifying the experimental condition or treating the cells with different chemical compounds.

Depletion of extracellular calcium enables isolation of calcium coming from the ER, lysosomes and mitochondria. The simplest way to remove extracellular calcium is to place the cells in Ca^{2+} -free buffer or to add chelating agents, such as EGTA or BAPTA, to the medium [124]. On the other hand, the use of specific inhibitors is necessary for the detailed study of membrane proteins that are involved in the influx of calcium in the cytosol. A wide range of calcium channel blockers (like Verapamil and Nifedipine) commonly used in the treatment of cardiovascular diseases also exhibit immunosuppressive properties [125, 126, 127, 128]. The disadvantage of these blockers is that they don't act on a specific target, but rather block multiple voltage-dependent channels at the same time. The same can be said for other compounds

that are not administered as drugs, like Gadolinium chloride. Gadolinium chloride has been used as a SOCE inhibitor and is able to block both voltage-dependent and mechano-sensitive channels [129, 130]. On the other hand, the Synta66 inhibitor shows selectivity towards the ORAI1 channel. Treatment of T cells with Synta66 enables blockade of CRAC channels, preventing SOCE without reducing cell viability [131, 132].

Depletion of intracellular storage (especially ER) allows to study the role of the calcium influx and its importance in arise the global signaling. SERCA inhibitors, Thapsigargin, cyclopiazonic acid (CPA) and tBHQ, made possible to IP₃-sensitive store and activate SOCE [133, 134]. Moreover, the inhibition of SERCA prevents also the refill of ER impairing the ability to the T cells of responding to the activation stimulus. Other inhibitors of the lysosome storage are under study to deepen the knowledge about the formation of Ca²⁺ microdomains. Taken together these strategies have allowed over the past decades to deepen our knowledge of T cells activation.

1.4 Gold nanoparticles: SPR and photothermal characteristics

Plasmonic nanoparticles (NPs) are metal-based nanoparticles (typically noble metals such as gold, silver, or copper) that display large electromagnetic fields at their surface when excited with light at the appropriate wavelength [135]. The oscillating electromagnetic field of the light induces a synchronized oscillation among the free electrons on the surface of the NPs (known as conduction band electrons). This electron oscillation around the surface of the particle generates a charge separation on the NPs' surface, resulting in an oscillating dipole aligned with the electric field direction of the light [136] (**Figure 1.4**). This phenomenon is known as surface plasmon resonance (SPR) [137, 138, 139] or localized plasmon resonance (LSPR) [140, 141]. Typically, the SPR is located in the ultraviolet (UV, from 10 to 400 nm) or near infrared (NIR, from 780 to 2500 nm) regions of the electromagnetic spectrum [142]. The wavelength and the intensity of the electromagnetic field inducing SPR depend on three factors: nanoparticles' size [143], shape, composition and the aggregation state [144].

Among plasmonic nanoparticles, gold nanoparticles (AuNPs) have been extensively studied because their SPR lies in the visible spectrum [146], and therefore any modification (in terms of size, shape, and surface functionalization) leads to a colorimetric change of the NPs dispersion [147, 148]. Over the time, AuNPs of different size (from 10 to 400 nm) and shape (sphere, rod, nanocube, nanoshell, nanostar, etc...) have been synthesized. Since SPR is dependent on these two parameters, researchers have been able to tune them to obtain particles that interact with the light in the NIR spectrum. The light in the NIR region holds a particular interest for bio-applications since it weakly interacts with biological tissue.

Gold nanostars (AuNSs) are particles with a plasmonic core (either a sphere, a rod or another shape) from which originates multiple sharp branches. Although the core plays a crucial role by providing electrons to the tips, thereby amplifying the electric field intensity as the nanoparticle grows, the primary plasmonic characteristics of AuNSs originate from the sharp tips, called "hot spots" [149, 150]. Nanostars can be synthesized following two different protocols: seedless and seed-mediated. The seedless method allows the production of nanoparticles in one-pot synthesis [151]. Although fast, simple, and high yield, this approach leads to the production of particles with a large polydispersity in size and shape. On the other hand, the

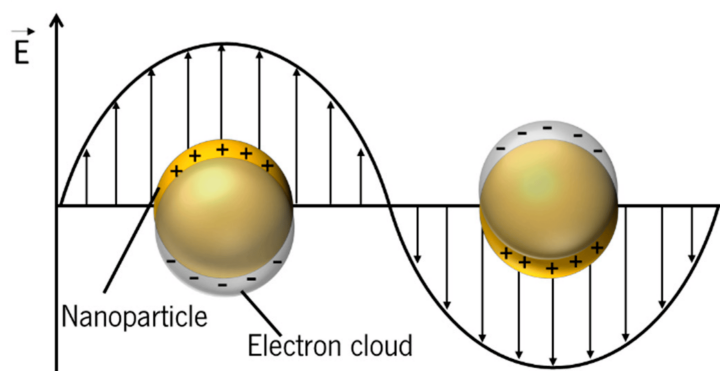


Figure 1.4: Scheme of the surface plasmon resonance (SPR) of a metal sphere. The electromagnetic field of the incident light induces a synchronized oscillation of the surfaces' electrons, creating a charge separation. Image adapted from ref. [145].

seed-mediated protocol requires two steps: first the synthesis of seeds and then the growth of the branches on their surface. Therefore, this approach is more complicated and time consuming but allows a better control over nanoparticles' shape and size [152, 153]. It is important to notice that the characteristics (especially crystallinity and size) of seeds play a huge role in this synthesis. For example, smaller seeds lead to the production of AuNSs with fewer but longer spikes, resulting in a narrower plasmonic band [154, 155]. Moreover, the time of addition of the seeds to solution is also important. If the seeds are added too early they will lead to an increase on polydispersity. Instead, if they are added too late they will induce nucleation, increasing the size of spherical nanoparticles without branches [154]. Finally, the ratio between the seeds and the gold precursors has to be taken into consideration since it will directly affect the nanostars characteristics [154]. Aqueous synthetic routes have been developed over the years and they have been proved efficient in increasing the biocompatibility of nanostars. Typically, ascorbic acid and silver nitrate (AgNO_3) are added to a solution of seeds in presence of chloroauric acid (HAuCl_4) and chloridric acid (HCl). Ascorbic acid is used as a reducing agent in combination with silver nitrate as a shape-guided agent. AgNO_3 is needed to block specific crystallographic planes on the surface of the seeds, allowing for the reduction of gold in the appropriate sites. The obtained AuNSs display well-defined tips. Nevertheless the number of tips per particle cannot be precisely controlled and it ranges from 1 to 6. This is probably due to the intrinsic crystallographic defects present on the seeds [156]. With this protocol, AuNSs with an average sizes ranging from 45 to 150 nm can be produced. While the corresponding plasmon resonance are between 630 and 900 nm [157, 158].

Due to their pointy shape, AuNSs are very efficient in converting the absorbed light into heat. When the nanostars are excited with the appropriate wavelength, SPR effect is induced and the surface electrons oscillates coherently. After few femtoseconds, electrons lose coherence and acquire thermal energy. This energy is transferred to the crystal lattice in form of phonons, increasing the temperature of the lattice of few tens of degrees [136, 159]. This feature of AuNSs is called photothermal heating and it is used for cancer treatment, catalysis and sensing [160].

Interestingly, Zhu *et al.* [100] have exploited AuNSs, embedded in a multi-layered polymer capsule, as thermal vector to induce the release of Ca^{2+} from lysosomes initiating the signaling cascade in MCF7 and HeLa cancer cells. The increase in temperature of the particles localized in the lysosomes induces the disruption (permanent or transient) of the membrane leading to the release of calcium from the organelle. The work reported in the present dissertation aims to apply this technique on T cells since the key role that calcium has in their functionality. Therefore, Jurkat lymphoma cells were treated with a photothermal vector and detailed studies on calcium spreading in the cytosol were carried out. Since the lymphocytes present different characteristics compared to the cells used by Zhu and co-workers, the experimental set-up was adapted accordingly. For example, in Zhu's paper AuNSs were embedded in a more complex structure called capsule. Capsules had a dimension of around 5 μm . Considering that the average diameter of T cells is 10 μm , it was unlikely that capsules could be uptaken by the cell. For this reason, in the present work plain AuNSs (of 200-250 μm dimension) were used.

Chapter 2

Materials and Methods

For the experiments, Jurkat T cell were treated with gold nanostars. The nanoparticles were produced in our lab following a well established protocol and characterized to keep their features constant. T cells were cultured as described and treated always with the same volume of nanostars. After the treatment, the cells were loaded with a dye to be able to visualize the Ca^{2+} release in real time. The videos obtained were analyzed using Fiji and MATLAB programs. ICP-MS was used to quantify the amount of elemental gold in both the nanoparticles batches and treated cells. In this chapter all the methods used and analysis performed were explained in detail.

2.1 Synthesis of Gold Nanostars

Gold nanoparticles with a low dispersity and a diameter of 12-13 nm were synthesized based on little adjustments to the Turkevich method from Schulz *et al.*[161].

Briefly, a buffer solution was prepared by mixing Trisodium citrate dihydrate (#S4641-500G, Sigma-Aldrich) with Citric acid (#251275-100G, Sigma-Aldrich) at a molar ratio of 75:25 in a 2000 mL beaker. The buffer was heated to its boiling point on a heated stirrer plate and covered with aluminum to reduce the evaporation of water. Separately, 200 ml of 812.5 μM trihydrate chloroauric acid ($\text{HAuCl}_4 \cdot 3\text{H}_2\text{O}$; #520918-5G, Sigma Aldrich) was prepared and heated to 90-100 $^\circ\text{C}$. The boiling time of the buffer solution before the precursor addition was 15 minutes. The precursor solution was added quickly under vigorous stirring (900 rpm) to the citrate buffer solution. After the color of the solution had changed into red, it was heated to boiling for an additional 20 min before the hot plate was switched off to let the solution cool to ≈ 70 $^\circ\text{C}$. The solution was then transferred into a glass bottle for storage. To improve the uniformity and dispersity of the AuNPs, 0.02 mM Ethylenediaminetetraacetic acid tetrasodium salt hydrate (EDTA; #E5134-500G) was added to the boiling citrate buffer before the precursor addition.

Gold Nanostars (AuNSs) were produced according to the protocol previously reported [100]. To 99 mL of MilliQ water at room temperature were added 2 mL of 25 mM $\text{HAuCl}_4 \cdot 3\text{H}_2\text{O}$, 950 μL of the above mentioned citrate-stabilized seed and 120 μL of 1 M Hydrochloric acid (HCL, 35 wt%, #X942.2, Carl Roth). After 1 min stirring, 1 mL of freshly prepared 2 mM Silver nitrate (AgNO_3 ; #204390, Sigma Aldrich) and 1 mL of freshly prepared 100 mM Ascorbic acid (#33034, Sigma Aldrich) were added simultaneously. The solution was stirred for 30 sec while its colour changed from light red to dark blue. The solution was then cooled down using an ice bath to stop the growing of the AuNSs. During the incubation in ice bath, 2 mL of 10

mg/mL HSC₂H₄CONH-PEG_{3kDa}-OC₃H₆COOH (MW = 3 kDa, #13300-4-32, Rapp Polymer) and 250 μ L of 2 M Sodium hydroxide (NaOH, #6771.1, Carl Roth) aqueous solution were added for ligand exchange. After 40 min incubation, the solution was left stirring overnight to return to room temperature. The day after, the solution was centrifuged at 8,000 rpm for 5 min, the supernatant was discarded and 40 mL of MilliQ water was added to redisperse the AuNSs. This procedure was repeated for 3 times. The last step consisted in redisperse the AuNSs in 15 mL of MilliQ water instead of 40 mL. The nanoparticles were then stored at 4 °C in a glass vial.

It is important to note that, since the grow of of the star-shaped nanoparticles is not precisely controlled, each batch can show slightly different features especially regarding the plasmon resonance absorption peak that can be varying from 810 nm to 825 nm.

2.1.1 Characterization of Gold Nanostars

The gold nanostars were characterized by UV-Vis spectrum measurement, TEM and SEM imaging.

The UV-Vis spectra of both Au seeds and star-shaped Au NPs are shown in **Figure 2.1**. These spectra were made with Cary 60 UV-Vis Spectrophotometer (Agilent). The absorption from 200 to 1100 nm was collected and the data were normalized on the absorbance at 400 nm. The seed Au NPs had the absorption peak is $\lambda_{\max} = 520$ nm. The surface plasmon resonance peak of the star-shaped NPs was from ~ 750 nm to 900 nm, with a $\lambda_{\max} = 825$ nm.

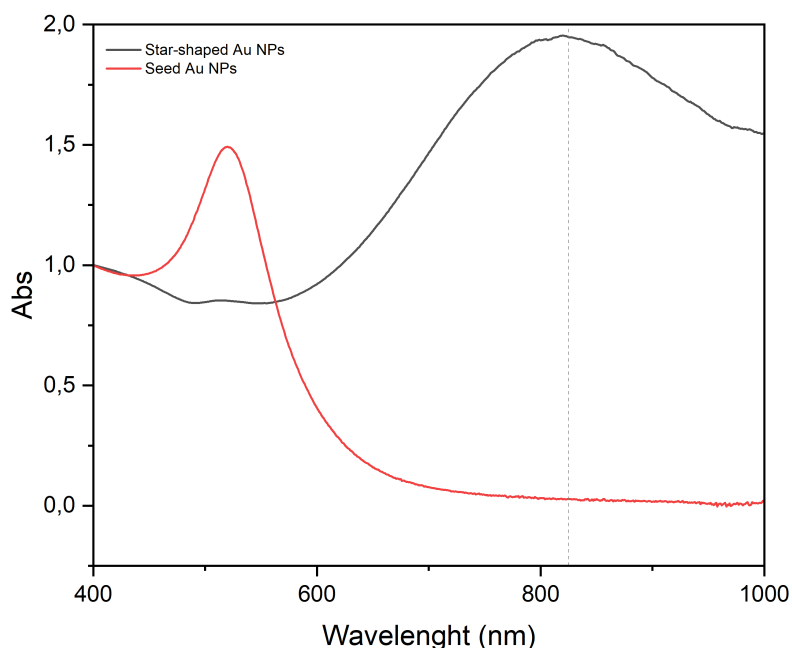


Figure 2.1: Normalized UV-Vis absorption spectra of seeds Au NPs and star shaped Au NPs in aqueous solution. The surface plasmon resonance peak $\lambda_{\max} = 825$ nm is shown as a dotted line.

Scanning electron microscopy (SEM) images were obtained using a Zeiss Sigma operated at an accelerating voltage of 10kV. To characterize the morphology of Au nanostars, the Au nanostars were directly deposited on a silicon substrate. High-resolution micrographs were obtained using the InLens detector. **Figure 2.2.**

Transmission electron microscopy (TEM) micrographs of AuNPs and Au nanostars were performed on a JEOL JEM-1011 microscope with an operating voltage of 100kV. The TEM samples were prepared by dropping 10 μ L of particle solution previously functionalized with PEG onto a carbon-coated TEM grid. The particle diameters were calculated by using the software Image J 1.53e. **Figure 2.3.**

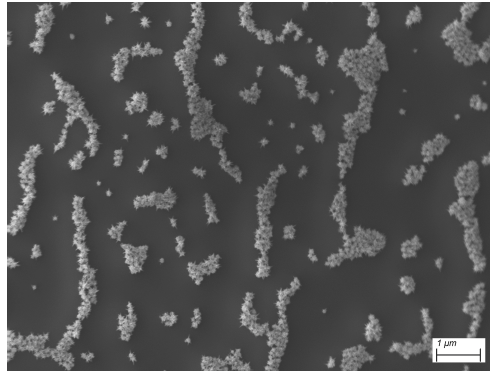


Figure 2.2: SEM image of AuNSs. Scale bar 1 μ m.

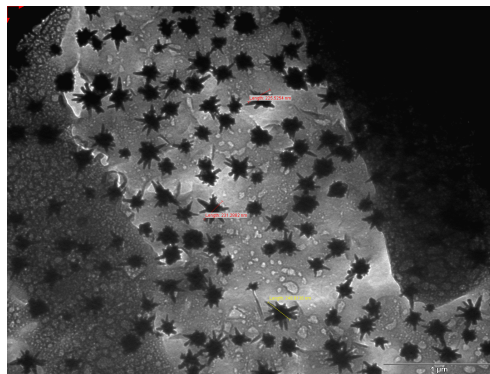


Figure 2.3: TEM image of AuNSs with dimension calculated on the image. Scale bar 1 μ m.

2.2 Petri coating

All the experiments were performed in μ -Dish 35 mm, high Glass Bottom Ibidi™ petri dishes (#81158, Ibidi) coated using the following protocol. 1 mL of 1 M HCl was added to the petri dish and left for 15 min at room temperature (RT). After that time, the HCl was discarded and the petri was washed three times with sterile Phosphate-buffered saline (PBS, #18912-014, ThermoFisher Scientific) and let it dry under a sterile hood. The glass section of the petri bottom was covered with 30 μ L of 5 mg/mL sterile filtered Bovine serum albumine solution (BSA, #A9647-10G, Sigma Aldrich) and let it dry under a sterile hood. Then, 100 μ L of 0.01 % poly-L-Lysine

(#P4832-50ML, Sigma Aldrich) was added and the petri was incubated for 30 min at RT. Finally, the petri was washed three times with sterile PBS. The petri was stored wet, with 1 mL of sterile PBS, at 4 °C sealed. Prior to use the liquid was removed and the dish was dried out under sterile hood.

2.3 Cell line

Jurkat T lymphocyte cell line was cultured in RPMI-1640 medium (#9091.1, Carl Roth) with 2 g/L Glucose and 2 mM Glutamine, supplemented with 10 % Bovine Calf Serum (#12133C-500ML, Sigma Aldrich) and 1 % Penicillin (50 IU/mL) and Streptavidin (50 mg/mL) (#11548876, Fisher Scientific). Cell doubling time is around 24 h. Cell concentration was kept between $0,3 \times 10^6$ and $1,2 \times 10^6$ cell/mL. They were left growing in suspension at 37 °C and 5% CO₂.

2.4 Cell treatment

50 µL of AuNSs was added to 1 mL of Jurkat T cells concentrated 100'000 cell/mL. The cells were placed in an Eppendorf tube inside the incubator over night at 37 °C, 5% CO₂. The day after, the cells were washed 3 times with sterile PBS, centrifuging at 300 rcf for 5 min, to eliminate the excess of AuNSs. Cells were stained with 5 µM Hoechst 33342 trihydrochloride trihydrate (#H1399, ThermoFisher Scientific) and 6.5 µM Fluo-4 AM [113] (#F14201, ThermoFisher Scientific) in sterile PBS for 30 min to avoid undesired subcellular compartmentalization. Then cells were washed 3 times with Calcium Buffer (140 mM NaCl, 5 mM KCl, 1 mM MgSO₄, 1 mM CaCl₂, 1 mM NaH₂PO₄, 20 mM HEPES, 5.5 mM glucose; pH 7.4; sterile filtered) and kept for 20 min at RT for de-esterification before the start of measurement.

After the staining, cells were either resuspended in different solutions or treated with different compounds, following the conditions listed below.

- To study the release of Ca²⁺ mimicking the *in vivo* conditions, cells were left inside the complete medium as source of extracellular calcium.
- To better visualize the contribution of the calcium storages (like ER) to the signal, cells were maintained in Ca²⁺ and Mg²⁺ free PBS.
- To stop the calcium entry from the extracellular space via inhibition of ORAI1 channel, cells were treated with 50 µM of Synta66 (#SML1949-5MG, Sigma Aldrich) in Calcium Buffer for 15 min before imaging.
- To prove that Synta66 was the solely responsible for the observed results, a volume of Dimethyl Sulfoxide (DMSO, #D2650, Sigma Aldrich) equal to the volume of Synta66 was added to the cells in Calcium Buffer.
- To confirm that Calcium Buffer didn't affect the experiment, cells were stimulated in Calcium Buffer without any treatment
- To suppress calcium release cascade by emptying the ER calcium storage, cells were treated with 1.67 µM of Thapsigargin (#T7458, ThermoFisher Scientific) in PBS wo Ca²⁺ and Mg²⁺ for 15 min before imaging.

Prior to image, the cells were placed in the coated petri dish and left undisturbed for 10 min to give them time to adhere to the surface.

2.5 LSM880 microscope set up

The real time imaging was performed using a confocal Laser Scanner Microscope 880 (LSM880) from Zeiss. Since the system is an upright microscope, the objective was directly immersed inside the sample. The water immersion objective W Plan-Apochromat 20×/1.0 DIC D = 0.17 (UV) VIS-IR M27 75mm was used. The samples were maintained inside the microscope incubator at 25 °C, for the entire duration of the measurement, from 1 to a maximum of 4 hours.

The cells were visualized using Argon 488 nm and Diode 405 nm lasers. Argon laser was used to excite Fluo4-AM, while Diode laser was used to visualize the transmitted light and to excite the nuclear fluorophore Hoechst, when present. Photothermal heating was achieved with MaiTai wide band, mode-locked Ti:Sapphire laser (Spectra Physics). This laser can produced a continuous laser wave ranging from 690-1040 nm. The MaiTai was set up at 825 nm to interact with the plasmonic resonance peak of the AuNSs and induced their increase in temperature.

T cells stained with Fluo4-AM and Hoechst were imaged as follow. Argon laser was set up at the 0.6 % of maximum laser power and filtered with a multi band pass filter (MBS 488/561/633). The emission signal was collected from 500 to 630 nm by a GaAsP PMT spectral detector (ChS1) and the digital gain was set at 720. Diode 405 nm laser was used at 0.4 % of the maximum laser power and filtered with a MBS (MBS -405/760+). Hoechst emission signal was collected from 450 to 499 nm by a GaAsP PMT spectral detector (Ch1). The digital gain was 250 for the transmitted light and 720 for the Hoechst signal. Modular MaiTai laser was set at 825 nm to interact with the surface plasmonic peak of the AuNSs and induce the local increase in temperature. MaiTai laser was used in a various range of laser power: 0.2, 0.5, 2 and 5 %. This was due to the biological variability of the different samples.

The image set up was optimized to obtain an high frame rate without excessively impairing the image resolution. The acquired field of view was 168x168 pixels, corresponding to an area of 23.6 μm × 23.6 μm (pixel size 0.14 μm). The choice of the field of view was dictated by the need of minimizing as much as possible the number of pixels to increase the acquisition frame rate while allowing the imaging of the entire projected area of one T cell. The bit depth was 16 bit and the scan mode was bidirectional. The maximum scan speed was applied to obtain a frame rate of approximately 25.63 msec.

The experiment was carried out using the built in bleaching mode of the software. The determined number of cycles, which means the numbers of frames, was 3000 without any interval between them since the scan speed was already at the desired frame rate. The entire measure lasted 1.30 min for each cell.

2.6 ICP-MS

To determine the mass concentration of AuNSs solution, in terms of elemental concentration, and their cellular uptake, inductively coupled mass spectrometry (ICP-MS) 7700 setup from Agilent with an integrated auto sampler was exploited.

To obtain the solution concentration, 50 μL of the gold nanostars (diluted 1:1, 2:1, 4:1, 8:1, 16:1, 32:1 and 64:1) were digested with 150 μL of freshly prepared *aqua regia* (mixture of HCl and Nitric Acid (HNO₃) in a 3:1 ratio) over night at room temperature inside the fume hood. The day after samples were further diluted with 1.8 mL of 2% HCl. Each sample was prepared in triplicate. The results were plotted against the volume, **Figure 2.4**.

To evaluate the uptake, 100'000 Jurkat T cells were pretreated with 50 μL of

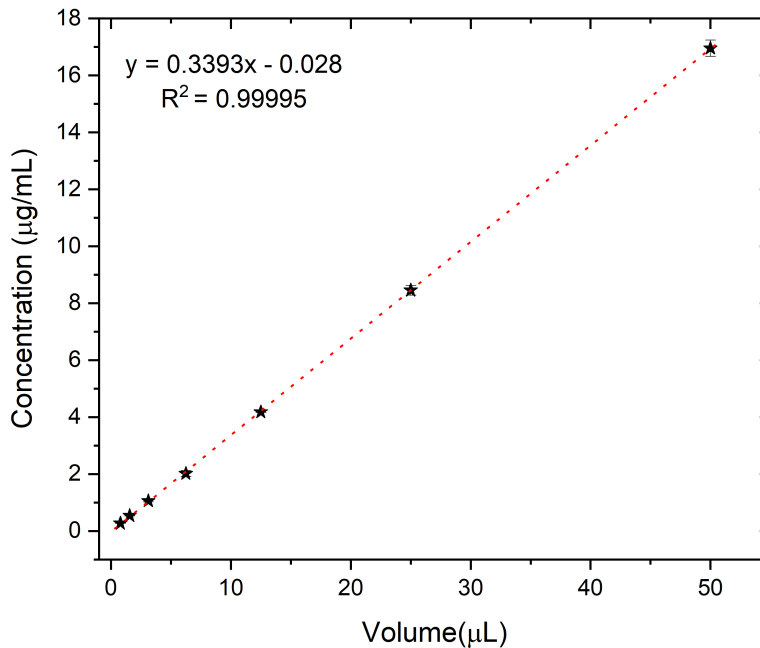


Figure 2.4: Standard curve of Gold Nanostar by ICP/MS

AuNSs for different time points: 2, 4, 6, 16, 24 and 48 hours. After the treatment cells were washed with PBS for three times and counted with Neubauer Counting Chamber. The samples were then pelleted, resuspended in 150 μL of freshly made *aqua regia* and left under the fume hood for 2 days at room temperature. The fully digested pellets were diluted with 1.85 mL of 2% HCl. Each sample was prepared in triplicate. Results are shown in **Figure 2.5**

The calibration curved used by the instrument was obtained using an elemental gold standard (1 mg/mL) diluted consecutively from 2500 to 10 parts per billion.

Based on ICP-MS results, the AuNSs solution concentration is 0.68 ± 0.016 mg/mL. Since T cells were treated with 50 μL of nanoparticles, the total amount of gold placed in each samples was 33.8 μg .

Regarding the uptake, the results in **Figure 2.5** show an increase in the concentration of gold in the cells until 24 h incubation. After that time, at 48 h incubation, the concentration decreases. The selected incubation time for the experiment, was 16 h and it will express from now on as "overnight incubation" (o/n).

2.7 Data analysis

The data obtained were firstly analyzed manually with Fiji software [162] and afterwards semi-automatically using MATLAB. Fiji was used to get the plot of the intensity of the cell *versus* time (by using "Plot z-axis Profile"), in this way a first screening could be made to discriminate between responsive and non responsive cells. From the plot, the time points of the experiments could also be retrieved. Moreover, Fiji allowed to convert the files from the Zeiss format (.czi) to Tiff, so that they could be

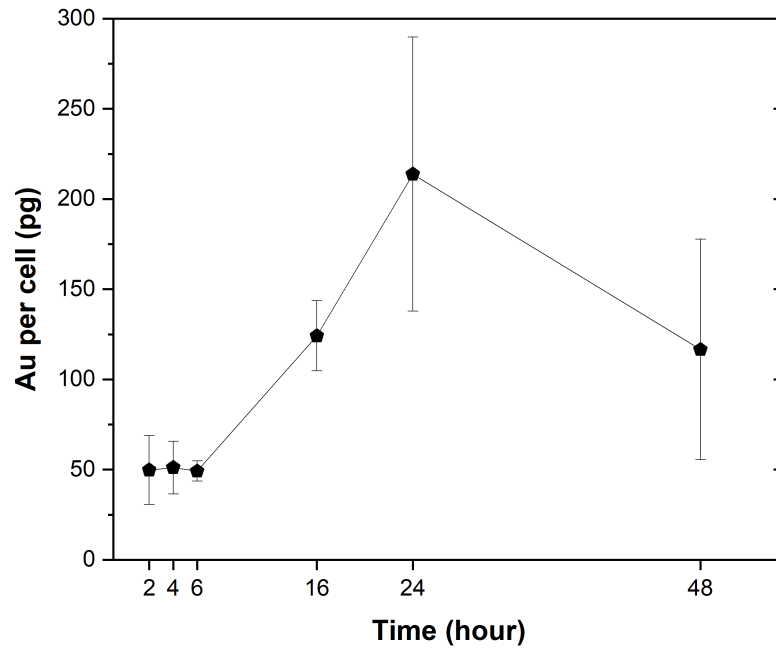


Figure 2.5: Uptake of AuNSs by Jurkat T cells

used by MATLAB software.

MATLAB software was exploited to perform data image analysis as followed:

1. Cell segmentation:

the analysis was performed via binarization. Threshold was determined creating a 10 pixels thick border of the frame, making sure that no part of the cell was accidentally taken into consideration. The average value (I_{bkg}) and the standard deviation (σ_{bkg}) of the intensity in the border was then computed on the first frame. Hence, the threshold was defined as:

$$I_{thresh} = 2 \cdot (I_{bkg} + \sigma_{bkg}) \quad (2.1)$$

To reduce white noise, a gaussian filter was applied with width equal to 3 pixels. The filtered first frame was then binarized using the intensity threshold I_{thresh} : all points with intensity larger than I_{thresh} were considered part of the cell (1), while all the others were considered part of the background (0). The above-mentioned procedure was then applied to at each recorder frame, using the segmentation of the first frame. The segmentation was performed only on the first frame and not on all of them for few reasons. Firstly, since the cell intensity greatly changed over time, also the signal to noise ratio would change accordingly. This made difficult to define a common threshold for all of the frames. Secondly, even if the cell could slightly modify its shape and size, the fluctuations of the area were minor and didn't affect significantly the overall data analysis. Lastly, tests made performing frame by frame new segmen-

tation didn't reveal significant differences from the results obtained with the described procedure.

Within the segmented cell the mean (I_{mean}) and maximum intensity and its standard deviation was evaluate frame by frame.

2. Image registration

In case the cell moved during the video recording (because of poor adhesion on the substrate), registration was possible. Registration was based on an area conservation criterium. Therefore, it could be exploited when the cell displacement was of few pixels and was mainly transitional. The registration was obtained following the steps described below. First, the cell area was obtained from the segmentation on the first frame: the number of pixels (N) constituting the cell was therefore obtained. The center of mass of the binarized cell (x_0, y_0) was also obtained. Then for each frame, the time average with the over 9 frames was made. Moreover, Gaussian filter with width 3 pixels was made on the average. The brightest N pixels were identified and binarization was made putting equal to 1 all those pixels and to zero the others. On this binarized object, the geometrical center of mass (x_i, y_i) was obtained. Each frame i was registered applying a rigid translation:

$$\Delta x_i = x_i - x_0 \quad (2.2)$$

and

$$\Delta y_i = y_i - y_0 \quad (2.3)$$

After the image registration, the segmentation and the frame by frame measurement of intensities was made as described above.

The time average and the spatial smoothing were made in order to avoid having noise related fluctuation entering in the segmentation based on the N brightest pixels. Registration was made only when visual inspection of the image stack revealed the presence of a translation. For not moving cells, comparison of the analysis with registered and unregistered procedure resulted in no significant differences (first validation of the method). Visual inspection of the registration procedure was also made to verify that registration was properly made (second validation of the method). For samples with large translations and rotations, a more refined registration is required for future works. In the present work those samples were not analyzed, but they represented less than 5% of the dataset and often corresponded to cells that for other reasons had been rejected.

3. Treated movies

In order to visualize calcium dynamics more easily as a function of space and time, different visualizations had been adopted to reduce noise and enhance contrast. The first step to appreciate calcium dynamics was to normalize each frame x, y, t over the mean spatial intensity in order to have the same average intensity inside the cell at each frame. Therefore the Normalized Intensity $I_{norm}(x, y, t)$ was obtained by normalizing over the average intensity:

$$I_{norm}(x, y, t) = \frac{I(x, y, t)}{I_{mean}(t)} \quad (2.4)$$

As shown in the results in **Figure 3.8** (cfr **Section 3.2**), this allowed to observe the change of the spatial distribution of the signal over time.

In order to better appreciate calcium spreading removing the intrinsic intensity heterogeneity of the cell (e.g. due to the presence of the nucleus), background subtraction intensity was evaluated by subtracting at each frame the starting intensity distribution. To do so, the noise was firstly reduced evaluating a moving time average of I_{norm} over 3 consecutive frames and applying a 2D median filter, obtaining $I_m(x, y, t)$. Then, the starting spatial intensity distribution was evaluated as the average I_m before laser shooting, obtaining $I_{m,0}(x, y)$. Finally, ΔI_{norm} was obtained as

$$\Delta I_{norm}(x, y, t) = I_m(x, y, t) - I_{m,0}(x, y) \quad (2.5)$$

As shown in the results in **Figure 3.8** (cfr **Section 3.9**), the Background subtraction allowed the spatial visualization of the beginning of the calcium spreading and, therefore, the identification of the Ca^{2+} microdomains.

4. Intensity profile: plot, t_{max} and I_{max}

From the single cell mean intensity profile $I_{mean}(t)$, the maximum intensity was identified (I_{max}) and the corresponding time (t_{max}) was noted. For each condition (medium, PBS wo Ca^{2+} and Mg^{2+} and Synta66) the average and standard deviation was computed for both t_{max} and I_{max}/I_0 . The latter was normalized over the pre-shot average intensity, obtained averaging over all the pre-shot recorded frames in order to obtain the relative increment of intensity due to calcium release.

5. Analysis of the radius

To obtain the cell radius and, therefore, be able to appreciate the radius increase over time, the analysis described below was performed. Starting from x_0, y_0 , the radial profile was extracted for any angle φ and azimuthal average was then made. Each profile was normalized by imposing equal to 1 the center of the cell and equal to 0 the average value outside the cell.

The value of the cell radius frame by frame was determined as follows. First, the point of the normalized radial profile closer to 0.5 was determined. Then, a linear interpolation was used to determine the cell radius with subpixel accuracy.

6. Ca^{2+} microdomains dynamics: angular profile and radial position

The Ca^{2+} microdomains dynamics was followed on a subset of cells that, before the shoot, exhibited an uniform intensity (with no visible internal structures) and with only one microdomain. This allowed for unambiguous and automatic definition of the microdomain position and a clean profile. Since just few cells fulfilled the abovementioned criteria, the numbers of sample considered for this analysis was lower. The applied procedure was the following. First, it has been selected the frame located 75 msec after the laser shot, at the typical timescale when the microdomain intensity is significantly higher than the global cell intensity and thus easy to localize. Then, the intensity of the choosen frame was collected and the spatial filter was applied to reduce the noise. The peak of intensity of the microdomains was identified on the filtered image. Since the peak did not move in the angular dimension (φ), and slightly move in the radial (r), it was possible to follow its intensity over time keeping its position fixed.

To confirm that the local increase intensity was linked to a Ca^{2+} microdomain, a control area was drawn in the point diametrically opposite the peak from the geometric center of the segmented cell. Therefore, at each time point the intensity, after the spatial average, of both the peak and control position was collected. Both intensity were then normalized on the signal pre-shoot and superimposed to the global increase of intensity of the whole cell (**Figure 3.10**). The data were obtained applying a moving average of 3 subsequent frames.

The intensity of the Ca^{2+} microdomains (J) was normalized over the average cell intensity at the same time in order to have a cell average value equal to 1 at all frames (**Figure 3.11**). This additional normalization was made to remove the global increase of intensity of the cell after the laser shot. The data were obtained applying a moving average of 3 subsequent frames.

In order to study in more detail the microdomains, their evolution over time was followed. Both the radial and azimuthal profiles of the normalized and filtered intensity passing from the identified starting position of the microdomain were obtained. The profiles were taken for each frame after the laser shot. To reduce the noise, a temporal mean was made on 10 frames (250 msec) and then plotted (**Figure 3.12** and **3.13**). Regarding the azimuthal profile, the width of the distribution was measured as half width half maximum. Regarding the radial distribution, the microdomain peak position was measured over time.

Chapter 3

Results

The results gathered from the different experiments are illustrated in this chapter starting from the basal condition (Medium, always represented in red) to the most complexes ones (PBS without Ca^{2+} and Mg^{2+} , in green; Synta66, in blue; Thapsigargin, in black). For all the conditions the same parameters were studied (time required to reach the peak of intensity, maximum intensity, calcium dynamics, ...etc) and compared, testing significance of the differences. All the data are interlinked and help to understand the whole picture. The set up was also studied to optimize its performances.

3.1 Characterization of T cells response to photo-thermal stimulation

3.1.1 Time evolution on mean intensity

Jurkat T cells were treated with 50 μL of gold star-shaped nanoparticles. The presence of gold nanoparticles in the cells made possible to exploit their unique physical characteristics to excite the surface plasmon and, therefore, obtain a fast local increase in temperature. This transient rise in temperature triggered the release of Ca^{2+} from lysosomes leading to the activation of the calcium amplification signaling system. After the incubation, cells were rinsed to removed the excess of nanostars and stained with Hoechst and Fluo4-AM. Then, Jurkat were washed, resuspended in complete medium and plated in a coated petri dish. The sample was placed under a confocal microscope and shoot with a laser set at the appropriate wavelength. The laser power with which cells were stimulated could easily be set with the instrument software and it was expressed as percentage of the maximum. Overall these were the adopted laser power percentages: 0.2, 0.5, 2 and 5%. Each cell reacted to the stimulus differently, in a way that cannot be known *a priori*. Hence, during the experiment the laser energy was increased or decreased depending on the responsiveness of the cells. The 0.2% was the starting laser power in every experiment. If the cell was not responsive or slightly responsive, the percentage was increased till the maximum 5%. The observed survival rate was 66 % on average with a high inter-sample variability. Even if it was sometimes possible to anticipate the outcome of the experiment in terms of viability (for example, newly thawed cells tended to be more prone to died after 0.2% laser shot), it is still unclear why such a great variability could be observed inside the same sample.

The detection of Ca^{2+} migration and distribution inside the T cells was based on

the fluorescence of Fluo4-AM calcium indicator[113]. This molecule exhibits an immediate increase in fluorescence upon binding Ca^{2+} . The change in the fluorescence intensity can be plotted versus the time. The plots display a characteristic profile, shown in **Figure 3.1**, which can also be found in the literature when T cells are activated by mimicking a biological stimulus [163, 164]. The signal is normalized on the average intensity of the first 201 frames (*circa* 5 seconds) before the shooting of the laser. Pre stimulus, Jurkat cells exhibit a low intensity profile. It's important to point out that sometimes the signal before the shooting can slightly increase or decrease, however not significantly. This is due to the high biological variability between different samples and different cells inside the same sample. After 5 seconds, the laser hits the cell (grey dashed line in **Figure 3.1**) and induces the release of calcium. On the graph, a rapid increase of the fluorescence can be observed. The increase lasts for few seconds until it reaches a peak. The peak correlates with the maximum intracellular calcium concentration and it is followed by a decrease of the fluorescence. The lessening of the signal can be rapid or slow depending on the cell and the samples, but it was always slower than its increase. Overall all the samples show a similar profile even though some differences can be detected between cells within the same sample. From the same data, both the time needed by the cells to reach the peak and their maximum intensity can be quantified (cfr. **Section 2.7**).

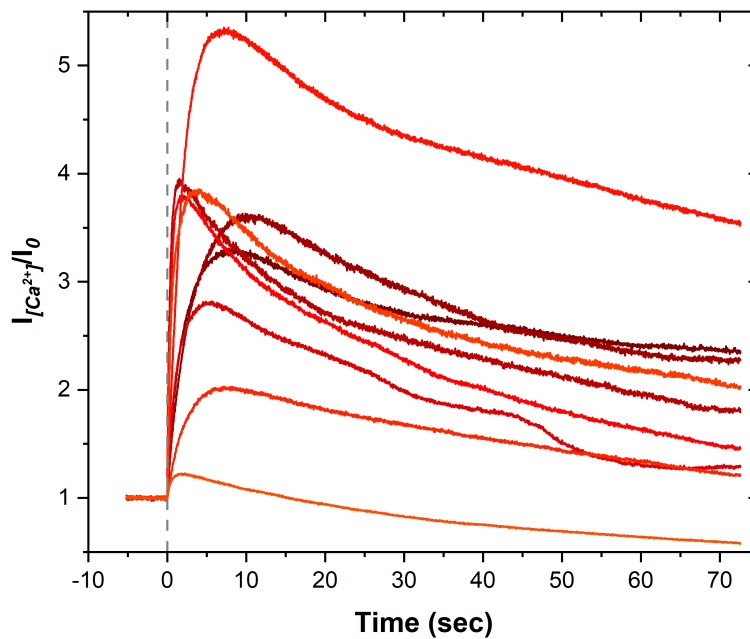


Figure 3.1: Normalized fluorescence intensity versus time of T cells in complete medium. The fluorescence is normalized over the first 201 frames before the laser shot ($t=0$). The grey dashed line represents the laser shot. Each line is a different cell. The graph displays 9 different samples collected on different experiments run on different days.

3.1.2 Reiteration of the signal

Allowing the cells the appropriate time to restore the calcium storage, can lead to the possibility to reiterate the stimulus, as the cells can respond to the same stimulus more than once. **Figure 3.2** shows two different cells that have been shoot twice (**3.2B**) or three times (**3.2A**). In both cases the resting time between subsequent stimuli is 12 minutes. After that time, the laser is shoot as for the first time. The response to the subsequent stimulation does not always result in the same fluorescence intensity, as shown in **3.2A**. However, the sudden increase in the signal is neat and sharp and cannot be mistaken with a physiological release of calcium from the cellular storage, independent from the laser.

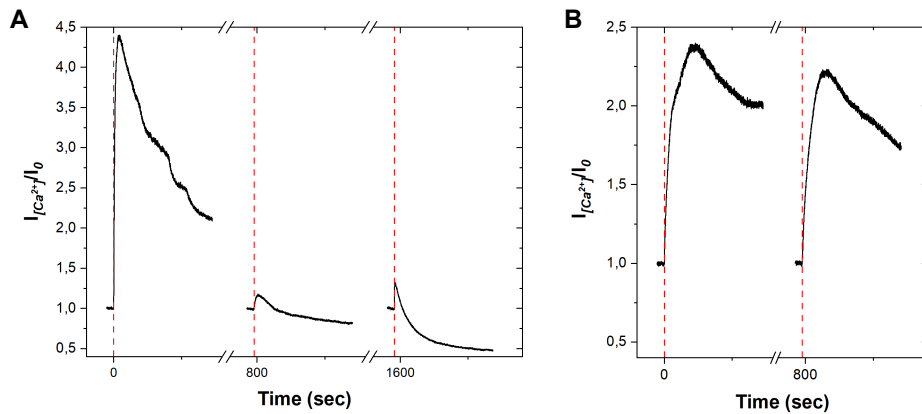


Figure 3.2: Reiteration of the stimulus. The graphs show the normalized intensity versus the time of two different cells that are stimulated twice (B) or three times (A). The fluorescence is normalized on the first 201 frames before the laser shot. The red dashed lines represent the laser shots. The axis breaks are equals to circa 10 minutes and they represents the resting time between subsequent stimuli.

3.1.3 Effects of Hoechst on cells response

In order to ensure that the observed increase of the signal was only related to the photothermal stimulus of the nanostars and not affected by the nuclear staining, tests were made in absence of Hoechst. Since it is an organic dye, indeed, Hoechst could potentially be photolyzed by the near-infrared laser and lead to unwanted signal. To make the comparison, two samples were prepared, as described before. One was stained with both Hoechst and Fluo4-AM (Medium) while the other only with Fluo4-AM (Medium wo Hoechst). As shown in **Figure 3.3**, the two samples didn't exhibit any significant difference in neither the time required to reach the peak of intensity (t_{max}) nor in the maximum intensity registered (I_{max}). The sample stained with both the dyes took 13 ± 1 sec to reach the peak, the same as the one stained without Hoechst (13 ± 1 sec). Even the I_{max} didn't show a significant difference, double stained samples display an intensity equals to 2.7 ± 0.2 a.u. while the other sample 2.9 ± 0.3 a.u.. The data shown are an average of $n=90$ cells stained and $n=25$ cells not stained with Hoechst. The measurements were performed on different days to take into consideration eventual daily variability of the samples. A *t* Student's two way test was carry out to confirm that there were no statistical difference between the two conditions. The obtained *p* values were the following: $p_{time}=0.97$ and $p_{intensity}=0.47$.

This means that there is the 97% of probability that the data obtained for the t_{max} of the two conditions belong to the same distribution. The same can be said for the I_{max} , where the probability is the 47%.

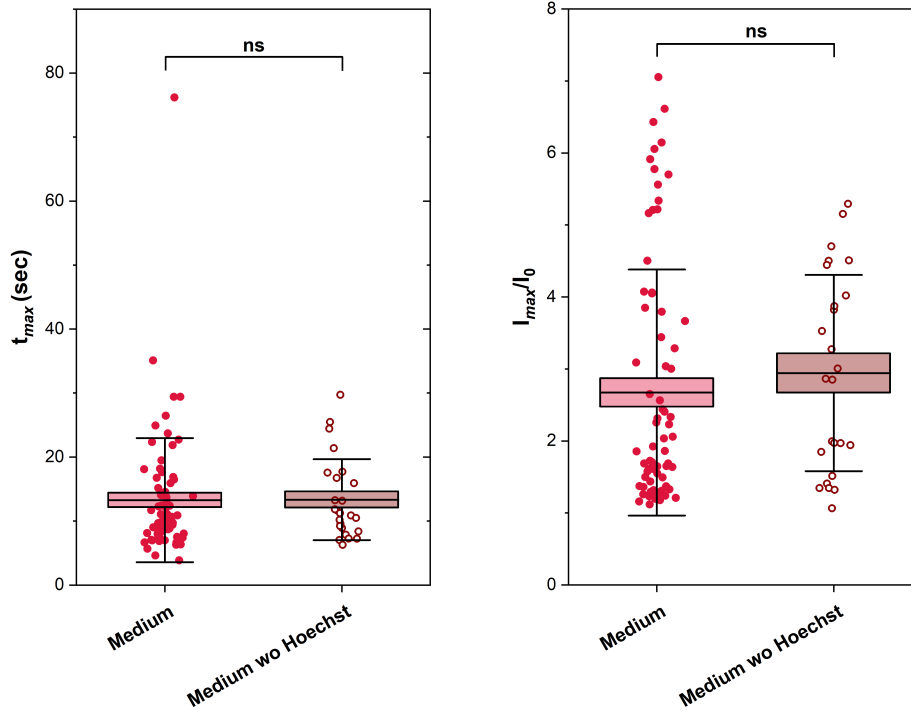


Figure 3.3: Time to reach the fluorescence intensity peak (left) and maximum fluorescence intensity (right) for T cell in Medium and in Medium wo Hoechst. The data shown are an average of $n=90$ cells stained and $n=25$ cells not stained with Hoechst. The p values were the following: $p_{time}=0.97$ and $p_{intensity}=0.47$. ns = non significant.

3.1.4 Role of the laser spot dimension

The next steps were to confirm that the presence of the nanoparticles was essential for the cellular response, and then to study the effects of the laser spot dimension on it. T cells were treated, as usual, with $50 \mu\text{L}$ of AuNSs, while the control sample remained untreated. After the removal of the excess of nanoparticles, both samples were stained with Fluo4-AM, placed in complete medium and taken to the confocal microscope to perform the release. As shown in **Figure 3.4**, the control sample does not show any increase in the signal after the treatment with laser. On the other hand the cell treated with the particles reacted to the stimulus as expected.

Gold nanostars dimension was around 200-250 nm. In view of their small size, a proper imaging AuNSs was not possible due to the intrinsic resolution limit of the confocal microscope. Nevertheless, some cells showed dark agglomerates suggesting the presence of aggregates of nanoparticles (as underlined by the red arrow in **Figure 3.5**). In these cases it was possible to manually draw the laser shooting spot centered on the uptaken nanostars, as in **Figure 3.5, first row**. These small laser spots (SL) were drawn always with the same area of $75 \mu\text{m}^2$ to keep consistency between the samples. Nevertheless, since it has been proven very challenging to identify

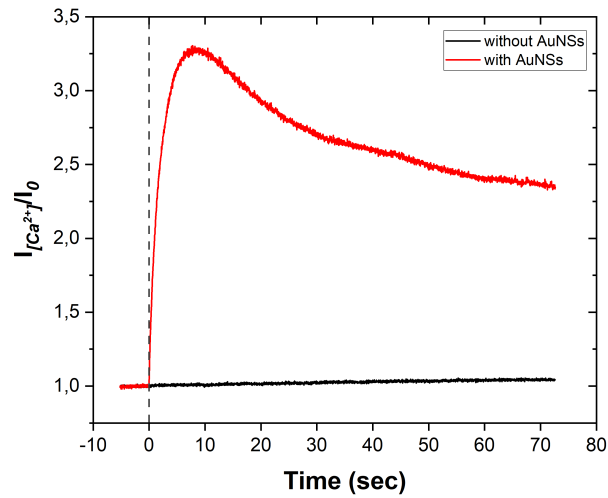


Figure 3.4: Normalized fluorescence intensity versus time of T cells in the presence (red line) or absence (black line) of AuNSs. The fluorescence is normalized over the first 201 frames before the laser shot ($t=0$). The grey dashed line represents the laser shot. Each line is a different cell.

nanostars in cells, a different strategy should be exploited. For this reason, the laser shot was drawn to include the whole cell (**Figure 3.5, second row**). The large laser (LL) allowed to excite AuNSs whenever at least a nanostar is present in the cell, even though no dark aggregates could be visualized inside the considered cell. Due to the biological variability of the cells the dimension of the large laser (LL) spot changed adapting to them.

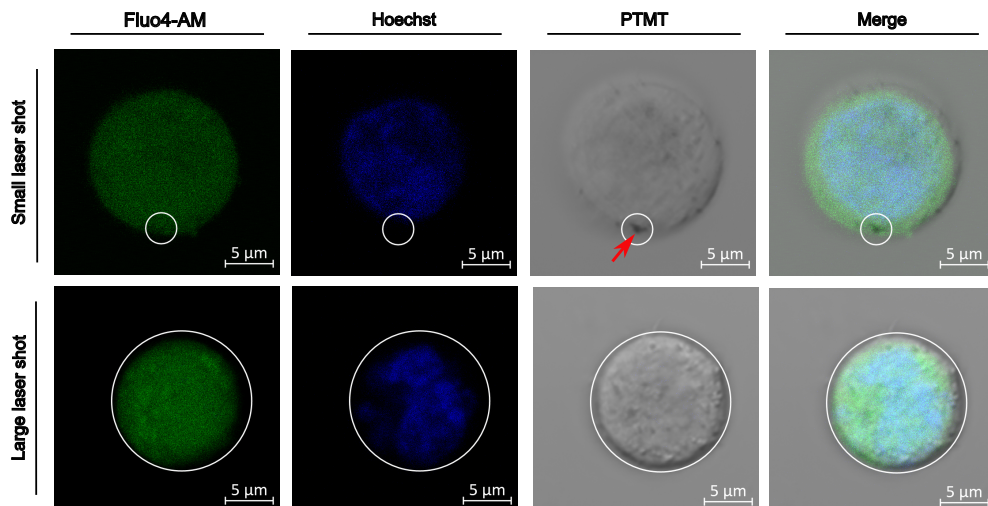


Figure 3.5: Laser spot dimension. Jurkat T cells with a small laser spot (upper part) or large laser spot (lower part). Fluo4-AM (green) stain the calcium ions inside the cell, Hoechst (blue) the cell nucleus and PTMT is the transmitted light. The red arrow points at an aggregate of AuNSs. Scale bar: $5\ \mu\text{m}$.

To study if the different dimension of the laser spots led to some variations in the cellular response to the stimulus, two samples were prepared as described above and then shot using a SL or LL spots. **Figure 3.6** reveals that there is no significant difference in t_{max} or averaged I_{max} between the two conditions. Cells shot with a large laser spot displayed a t_{max} of 13 ± 1 sec while the ones shot with a small laser of 13 ± 2 sec. On the other hand, the maximum intensity remained around 2.6 a.u. (I_{max} of Medium (LL) 2.7 ± 0.2 a.u.; I_{max} of Medium (SL) 2.7 ± 0.4 a.u.). The data shown are an average of $n=15$ cells for Medium SL and $n=75$ cells for Medium LL. A two way t Student's test was performed to confirm that there were no significant difference between them. The p values obtained were the following: $p_{time}=0.81$ and $p_{intensity}=0.96$.

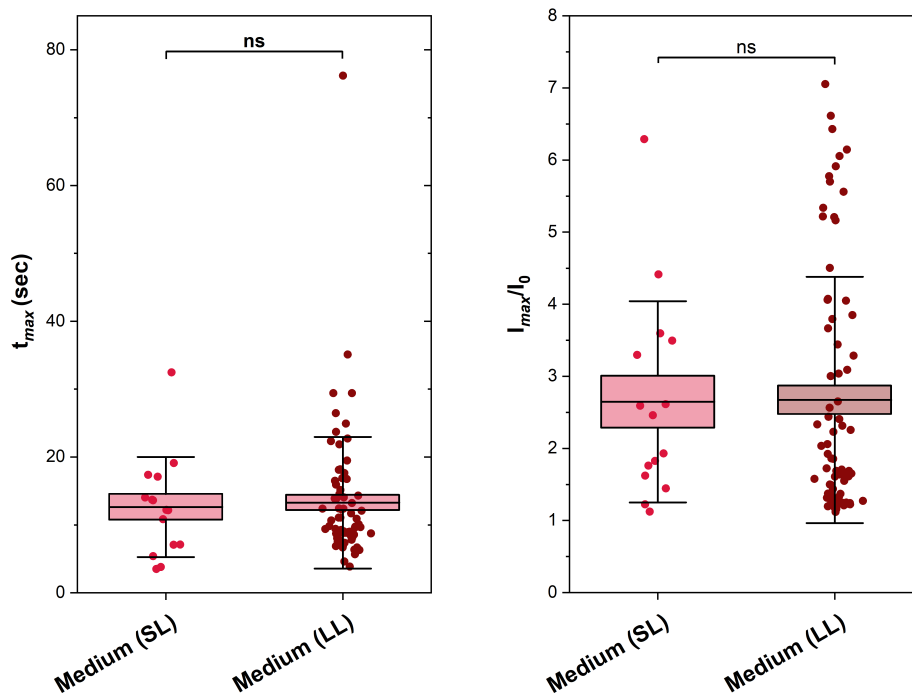


Figure 3.6: Time to reach the fluorescence intensity peak (left) and maximum fluorescence intensity (right) for T cell in Medium shot with a small (SL) or a large (LL) laser spot. The data shown are an average of $n=15$ cells for Medium SL and $n=75$ cells for Medium LL. A two way t Student's test was performed to confirm that there were no significant difference between them. The p values obtained were the following: $p_{time}=0.81$ and $p_{intensity}=0.96$. ns = non significant.

3.1.5 Responsiveness

Given the great variability found in the samples, the responsiveness of the different experiments and treatments (which will be discussed in **Section 3.3**) was studied to evaluate the percentage of successful stimulation. Responsiveness was defined as the neat and sharp increase of the cell fluorescence after the stimulation regardless the cell survival. In the graph in **Figure 3.7**, each dot includes all the measurements made in a single day, showing the difference in responsiveness between the experimental realization of each condition. Therefore, the data take into account the pos-

sible biological changes during cells cultivation and aging. Cells placed in Medium had an average responsiveness of 65%, the ones in PBS without Ca^{2+} and Mg^{2+} of 54% and the ones treated with Synta66 drug of 71%. Overall these data demonstrate that on average all the tested conditions have a good rate of responsiveness. It is important to keep in mind that not all the cells uptake the AuNSs. Hence, it is plausible to hypothesise that some of the samples, that were identified as non-responsive, were cells that hadn't taken up any nanoparticles and were therefore unable to respond to laser stimulation. The data shown for Medium (red) comes from $n=14$ different days, while the data for PBS without Ca^{2+} and Mg^{2+} (green) $n=8$ days and for Synta66 treatment (blue) $n=10$ days.

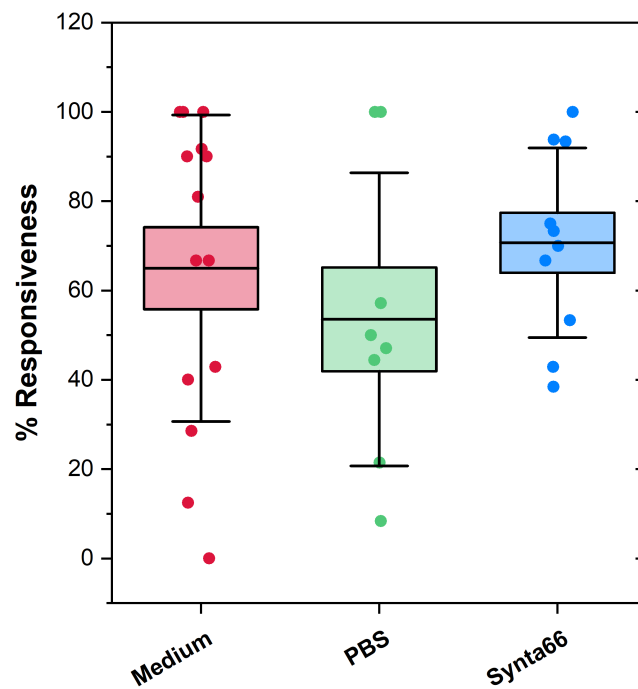


Figure 3.7: Percentage of responsiveness of samples in Medium (red), PBS wo Ca^{2+} (green) and Mg^{2+} and treated with Synta66(blue). The data shown for Medium (red) comes from $n=14$ different days, while the data for PBS without Ca^{2+} and Mg^{2+} (green) $n=8$ days and for Synta66 treatment (blue) $n=10$ days.

3.2 Ca^{2+} dynamics

Increasing the number of samples collected has given the opportunity to have a detailed visual description on how the signal starts and spreads inside the cell. In **Figure 3.8**, four images taken at different time frames are displayed.

The first image is taken at the beginning of the measurement ($t=-5.188$ sec) and represents the cell in a resting state. The second image shows the cell right after the

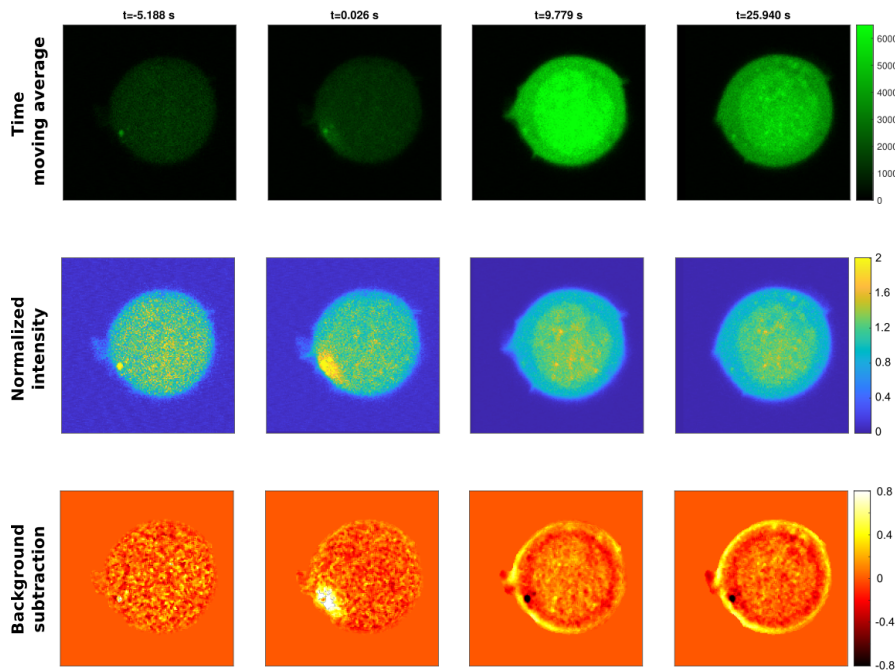


Figure 3.8: Image data analysis. The same Jurkat T cell is shown at the same time points with subsequent image analysis. The time points are: beginning of the measurement ($t=-5.188$ sec), first frame after the laser shot ($t=0.026$ sec), peak maximum intensity ($t=9.779$ sec) and decrease in signal intensity ($t=25.940$ sec). The first row shows the Time moving average, the second the Normalized intensity and the third the Background subtraction.

shooting of the laser ($t=0.026$ sec). The third image shows the cell at its peak of intensity ($t=9.779$ sec), while the fourth shows it during the decreasing of the signal ($t=25.940$ sec). The different rows illustrate the subsequent analysis made to study the spreading of calcium. In the first row, Time moving average, the green fluorescence of Fluo4-AM can be seen over time. At the beginning the cell is slightly green as right after the laser shot. However, with the passing of time, the fluorescence increase until the cell becomes bright green. After the peak, the cell remains fluorescent even though its intensity decreases. The first row represents what can be seen and collected at the confocal microscope during the experiment treated with a time moving average. Even though the time moving average allows a neat visualization of the signal increase over time, it does not allow to localize in space its starting point. To be able to identify and study the origin of the release of calcium, further image analysis were exploited (cfr. **Section 2.7**). Firstly, each frame was normalized to its average intensity and the resulted images are shown in the second row of **Figure 3.8**, Normalized intensity. These pictures show that the spatial distribution of the signal changes over time. Immediately after the laser shot, the signal originates from a localised point in the cell and can be observed even before a macroscopic increase in intensity can be seen. The main drawback of this analysis is the presence of macrostructures, such as the nucleus, that can still be seen. To remove the signal from the cellular structures, a background subtraction was applied to the normalized intensity (cfr. **Section 2.7**). In this analysis, the background is defined as the average

cell intensity of the first frames (before the laser shot). The obtained background was then subtracted from all the frames. The Background subtraction in **Figure 3.8** shows small calcium fluctuation, in the form of yellow spots, before the laser shot ($t=-5.188$ s) that could not be observed in the other data analyses. Moreover, this image analysis allows to see the spatial localization of the starting point more clearly than with the normalized intensity with time, the initially localized intensity spreads within the cell. Finally, when the cell reaches the peak of intensity ($t=9.779$ s) the localized signal is dispersed in the overall fluorescence intensity.

In **Figure 3.9**, the background subtraction of two different cells is shown. The first frame ($t=-0.026$ s) is taken during the resting phase of the cell, immediately before the laser shot. The other seven images follow the release of calcium from the laser shot ($t=0.000$ s) to less than a second after it. This short span of time allows to observe in detail the spreading of calcium.

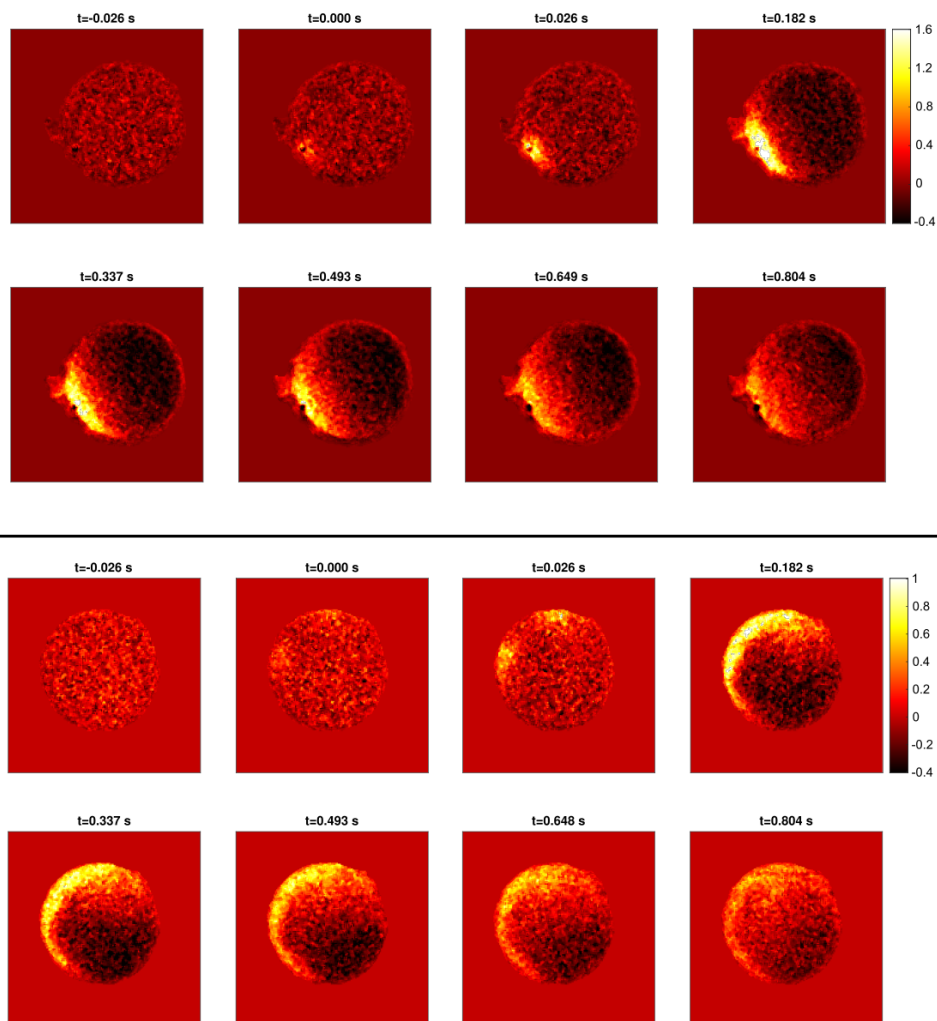


Figure 3.9: Ca^{2+} microdomains dynamics. Background subtraction of two different T cells. The images show the cells from the laser shot ($t=0.026$ s) to the blending of the microdomains with the whole cell signal ($t=0.804$ s).

Interestingly, the second cell shown in **Figure 3.9** presents not one but two starting points, well defined and separated from each other. This phenomenon suggests the presence of two AuNSs (or aggregates of AuNSs) that are stimulated at the same time. The presence of this localized signal can be identified as a Ca^{2+} microdomain, that is the initiator for the calcium release cascade. It is important to underline that the localized initial Ca^{2+} microdomains cannot be identified in all the stimulated cells and that's probably due to the fact that the cells are observed on a single focal plane that can be not the same from which the signal starts. Therefore the number of cells taken into consideration for further analysis of the Ca^{2+} microdomains is significantly lower compared to the number used to gain information on t_{max} and I_{max} .

In **Figure 3.10A** and **B**, it is presented the fluorescence intensity of the calcium microdomain (orange solid line) with the overall cell intensity (black solid line) against the time. In the same graphs an orange dotted line can be observed. It represent the intensity of a control area equal to the one used to define the Ca^{2+} microdomains but in an opposite position with respect to the cell geometrical center. The control area is needed to confirm that the Ca^{2+} microdomains intensity is not just due to the noise fluctuation of a small localized area. The plot shows that the Ca^{2+} microdomains' intensity grows faster than the whole cell intensity, although only in the first frames after the laser shot. Initially the slope of the Ca^{2+} microdomain signal is higher than the one of both the whole cell and the control area. Then, after roughly 2 sec, the slopes of the three curves become comparable and the curves only differ for an offset. The offset points towards a longer term localisation after the reaching of the maximum peak of intensity. The latter is an average behaviour but there is a great variability from sample to sample. In some cases the offset is almost zero as can be seen in **Figure 3.10C**. It is important to notice that the graph in **Figure 3.10A** and **B** represent the average intensity of $n=28$ different cells.

The plot in **Figure 3.10C** shows the average intensity against the time for one cell that has two Ca^{2+} microdomains. Each domain is represented by a different color: orange and violet. As for the the graph **3.10A**, a control area was drawn for every microdomain as shown in the diagram in **Figure 3.10D**. The intensity of both Ca^{2+} microdomains increase faster than the whole cell and the controls, as already observed for a single microdomain, and are quite remarkably superposed. After around 2 sec, the offset between the curves resets to zero and the microdomains signal blends with the one of the whole cell. Differently from the graph in **Figure 3.10A**, the one in **3.10C** represent a single cell and, therefore, is more noisy.

Figure 3.11 shows the relative intensity related to the Ca^{2+} microdomains (J_{μ} ; solid lines) and the one to the opposite position with respect to the cell geometrical center (J_{Ctr} ; dotted lines) against the time. The relative intensities were obtained by normalizing the microdomain intensity over the one of the whole cell (cfr. **Section 2.7**). The graph allowed to better visualize the peak of the Ca^{2+} microdomain. The fraction of time taken into consideration was just a small part of the total time of the experiment, roughly 20 sec from the beginning of the measurement. That's because, as seen in both **Figure 3.10** and **3.11**, microdomains' fluorescence rapidly blends in with the overall fluorescence intensity and cannot be distinguish after just about 3 seconds from the laser shot. From **Figure 3.11**, it can be seen that the increase in the intensity is not a noise fluctuation and can be discriminated from the background noise. It is important to notice that the J_{Ctr} (dotted lines) intensity goes under 1 after the laser shot (dashed line). That is due to the fact that the average intensity of the control is normalized on the total average intensity of the cell. Therefore when the intensity of the Ca^{2+} microdomain was added to the total intensity, the calculated J_{Ctr} decreased under 1. The zoom in, in the right side of **Figure 3.11**, allows to observe

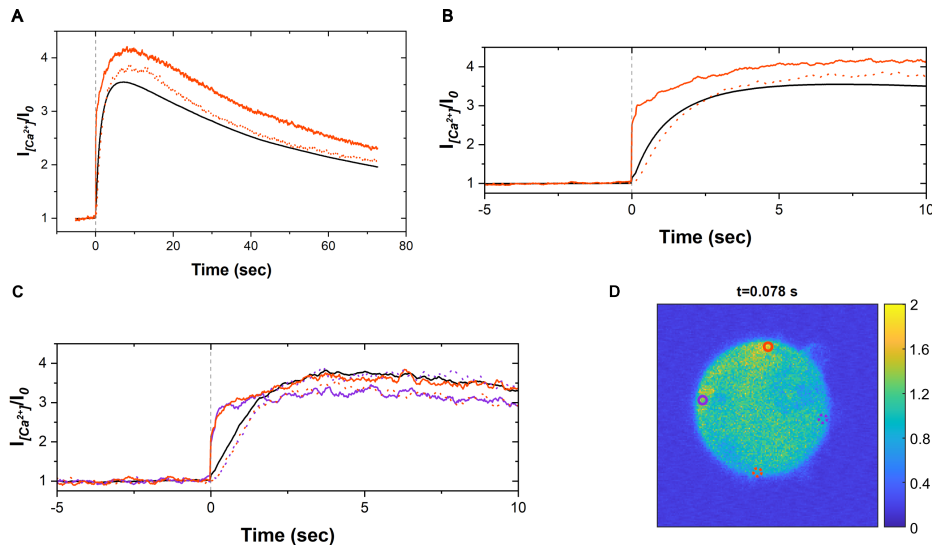


Figure 3.10: Visualization of calcium microdomain intensity compared to the whole-cell signal. The grey dashed line is the laser shot. A) and B): the orange line present the fluorescence intensity of the calcium microdomain, the black the signal of the entire cell and the dotted orange line represent the signal of the control area. The data are an average of $n=28$ cells. C) Both the orange and violet lines represent two distinct calcium microdomains, the black line the signal of the entire cell and the dotted lines the control areas. The data shown are relative to a single cell. D) Microdomains and control areas can be visualized inside the same cell of C, as circles whose colors and line styles correspond to the ones of C.

the time of the peak (t_{μ}). For samples imagined in complete medium t_{μ} was 0.10 sec, for the ones in PBS wo Ca^{2+} and Mg^{2+} was 0.24 sec and for the ones treated with Synta66 0.09 sec.

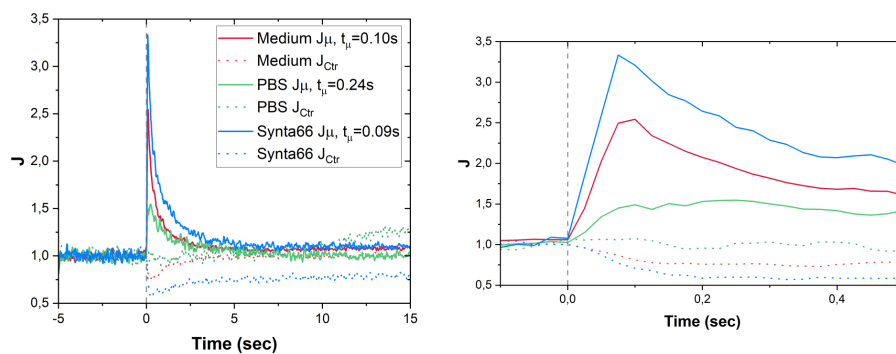


Figure 3.11: Relative intensity of the Ca^{2+} microdomains (J) versus the time. The dashed grey line represent the laser shot. The solid lines display the signal of the microdomains of the samples in Medium (red), PBS wo Ca^{2+} and Mg^{2+} (green) and treated with Synta66 (blue). The dotted lines are the relative controls. The data are a mean value of $n=6$ cells for Medium samples, $n=7$ cells for PBS wo Ca^{2+} and Mg^{2+} and $n=6$ cells for Synta66 treatment

Following the confirmation that the Ca^{2+} microdomains can be isolated from the overall intensity, their spreading in time was studied in detail. Observing the **Figure 3.9**, it is possible to notice that the Ca^{2+} microdomains spreads during time differently in the radial and angular direction. Therefore both the angular (**Figure 3.12**) and radial (**Figure 3.13**) distributions were studied. Angular distribution is evaluated at the radial coordinate (i.e. distance from the center) corresponding to the maximum intensity in the radial direction (i.e. along the green line in the cell scheme in both **Figure 3.12** and **3.13**). On the other hand, the radial distribution is obtained with a radial section from the center (0) to the cell membrane (1) passing through the maximum intensity of the Ca^{2+} microdomains (i.e. along the blue line in the cell scheme in both **Figure 3.12** and **3.13**). The abscissa coordinate was defined by dividing the radial coordinate (r) by the measured cell radius (R) (cfr. **Section 2.7**).

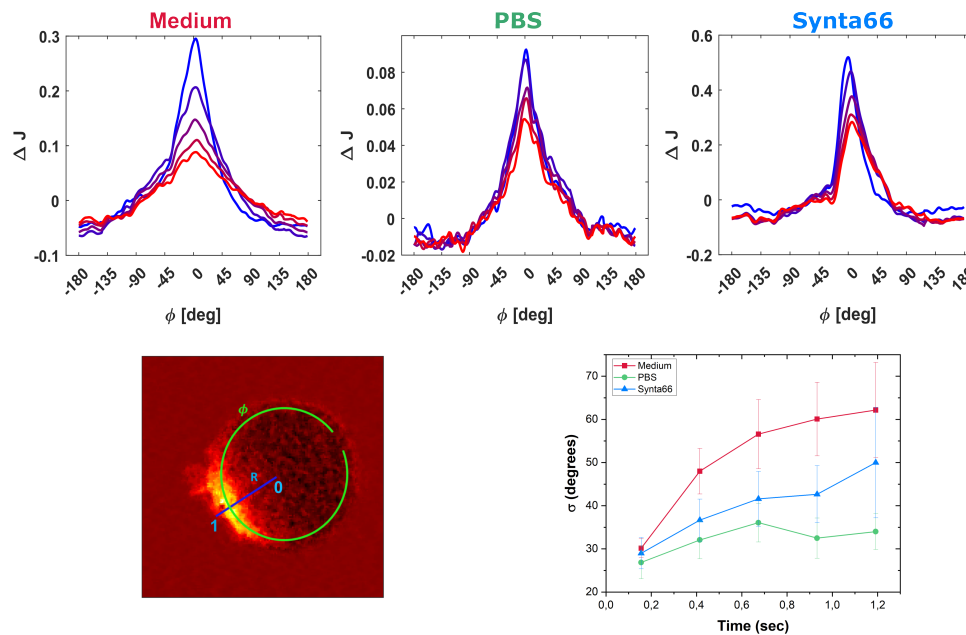


Figure 3.12: Angular distribution of Ca^{2+} microdomains. The upper part show the normalized intensity plotted against the angle (ϕ) in each condition tested (Medium, PBS wo Ca^{2+} and Mg^{2+} and Synta66). The lines goes from blue to red following the increasing of the time from 0 sec (laser shot) to 1.25 sec (the end of the Ca^{2+} microdomain's signal). Each line is the mean of 10 frames (250 msec). In the lower part, a graphical scheme shows the angular (green) and radial distribution (blue). The plot on the right side display the half-width half-maximum (σ) of the distribution against the time for each condition. The data are a mean value of $n=6$ cells for Medium samples, $n=7$ cells for PBS wo Ca^{2+} and Mg^{2+} and $n=6$ cells for Synta66 treatment

In **Figure 3.12**, in the upper part it's plotted the signal intensity against the angle (expressed in ϕ , degrees) over time (cfr. **Section 2.7**). The plotted lines go from blue ($t=0$ sec) to red ($t=1.25$ sec) following time as it progresses. Each line represents an average of 10 frames, thus the time step between two curves is equal to 250 msec. The darkest blue line corresponds to the starting of the calcium release. All the lines show a peak at the abscissa coordinate $\phi=0$. This coordinate is defined as the angular position of the maximum intensity in the first frame after the laser shot. Even if the distribution does not change the position of its maximum intensity, it widens

and decreases over time. To give more clarity, the with (σ , degrees) of the intensity distribution along φ was extracted and plotted versus time. This is made to allow a quantitative comparison between different conditions (described in **Section 3.3**). The data are a mean value of $n=6$ cells for Medium samples, $n=7$ cells for PBS wo Ca^{2+} and Mg^{2+} and $n=6$ cells for Synta66 treatment.

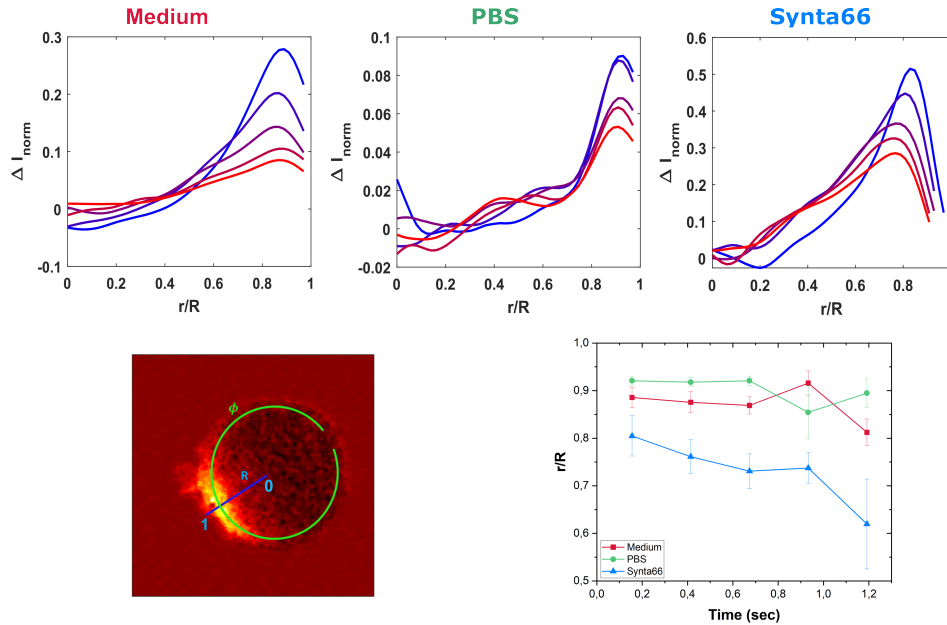


Figure 3.13: Radial distribution of Ca^{2+} microdomains. The upper part show the normalized intensity plotted against the radial coordinate normalized on the cell radius (r/R) in each condition tested (Medium, PBS wo Ca^{2+} and Mg^{2+} and Synta66). The lines goes from blue to red following the increasing of the time from 0 sec (laser shot) to 1.25 sec (the end of the Ca^{2+} microdomain's signal). Each line is the mean of 10 frames (250 msec). In the lower part, a graphical scheme shows the angular (green) and radial distribution (blue). The plot on the right side display the normalized radial position of the maximum intensity (r_{max}) against the time for each condition. The data are a mean value of $n=6$ cells for Medium samples, $n=7$ cells for PBS wo Ca^{2+} and Mg^{2+} and $n=6$ cells for Synta66 treatment

Regarding the radial distribution, in the upper part of **Figure 3.13** the graphs display the fluorescence intensity versus the ratio between the radial coordinate (r) and the cell radius (R) over time. As already explained above, the colors of the lines reflect the time course and are an average of 10 frames each. The distribution, unlike the angular one, does not show a symmetry and decreases in intensity over time without significantly changing shape. In the bottom right plot of **Figure 3.13**, the radial position of the maximum was plotted versus time to give more clarity. While the time goes by, the Ca^{2+} microdomains do not significantly move towards the center of the cell for samples in Medium. These data are collected from the same samples used for the study of angular distribution. Therefore the data are a mean value of $n=6$ cells for Medium samples, $n=7$ cells for PBS wo Ca^{2+} and Mg^{2+} and $n=6$ cells for Synta66 treatment.

3.3 Ca²⁺ depletion

The removal of Ca²⁺ from the extracellular space and the intracellular storage can be used to better understand how AuNSs induce the release cascade. The strategies adopted to induce an extracellular calcium depletion were two. On one hand the cells were placed in PBS without Ca²⁺ and Mg²⁺ instead of complete medium; on the other hand they were treated with Synta66 drug. Synta66 is able to inhibit the store-operated calcium entry channel ORAI1. Therefore the treated T cells are unable to exploit ORAI1 pathway to induce calcium entry and they are expected to be insensitive to extracellular Ca²⁺.

Regarding the intracellular storage, Thapsigargin drug can be used to empty the endoplasmic reticulum. Thapsigargin is a non-competitive inhibitor of the sarco / endoplasmic reticulum Ca²⁺ ATPase (SERCA). The inhibition of SERCA induces first the emptying of the ER from calcium and then prevent its replenishment. Thus, T cells treated with Thapsigargin fail to sustain the calcium release cascade.

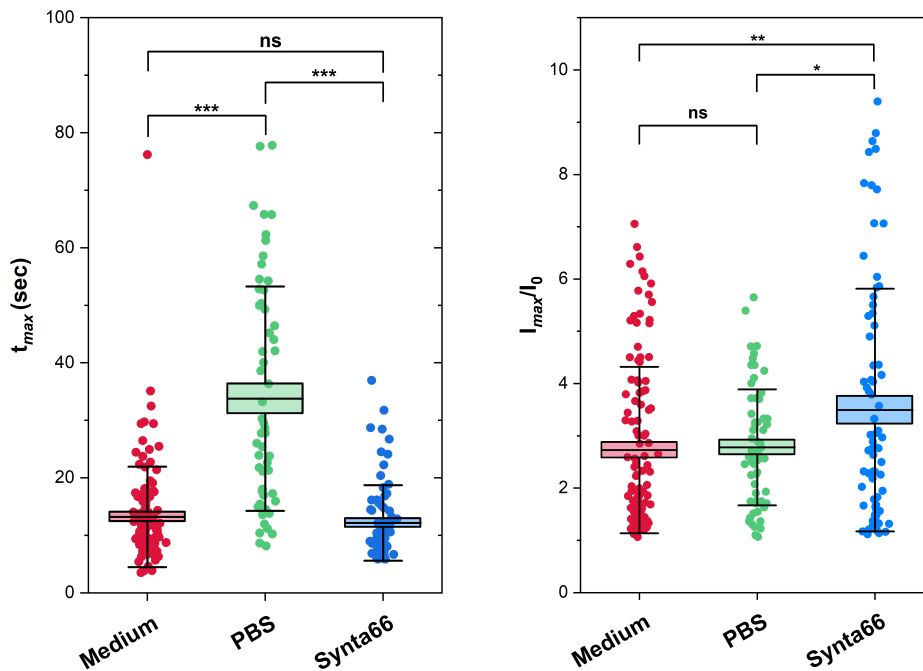


Figure 3.14: Time to reach the fluorescence intensity peak (left) and maximum fluorescence intensity (right) for T cell in Medium (red), PBS wo Ca²⁺ and Mg²⁺ (green) and treated with Synta66 (blue). The data shown are an average of n=115 cells in Medium, n=57 cells in PBS wo Ca²⁺ and Mg²⁺ and n=76 cells treated with Synta66. The Student's *t* test was performed and the *p* values obtained were the following. For the t_{max} plot, $p=1.36 \cdot 10^{-17}$ between Medium and PBS wo Ca²⁺ and Mg²⁺; $p=2.11 \cdot 10^{-15}$ between PBS wo Ca²⁺ and Mg²⁺ and Synta66 treated; $p=0.37$ between Medium and Synta66 treated. For I_{max}/I_0 plot, $p=0.79$ between Medium and PBS wo Ca²⁺ and Mg²⁺; $p=0.04$ between PBS wo Ca²⁺ and Mg²⁺ and Synta66 treated; $p=0.008$ between Medium and Synta66 treated. * = $p < 0.05$; ** = $p < 0.01$; *** = $p < 0.001$; ns = non significant.

3.3.1 Extracellular Ca^{2+} depletion: PBS without Ca^{2+} and Mg^{2+}

Jurkat T cells were incubated overnight with 50 μL of AuNSs. The following day, the cells were washed three times with PBS to remove the excess of nanoparticles and stained with Fluo4-AM. Then, they were washed again three times and resuspended in PBS without Ca^{2+} and Mg^{2+} . The sample was plated on a coated petri dish and the measurement was performed utilizing Zeiss LSM 880 microscope. The experiment was executed as already described above.

The obtained plot for the normalized average intensity vs the time was qualitatively similar to the one of the samples maintained in complete medium (Figure 3.1). The stimulation of the laser shot (dotted line) induced a sudden increase in the fluorescence intensity, followed by a peak and a slower decrease. From the quantitative point of view, Jurkat immersed in PBS wo Ca^{2+} and Mg^{2+} shown a significant delay in reaching peak intensity (Figure 3.15 and 3.14). In Figure 3.14, the difference in the time needed to reach the peak (t_{max}) between the two conditions can be visualized. Samples in complete medium took on average 13.2 ± 0.8 sec to reach the peak of intensity, whereas the ones in PBS wo Ca^{2+} and Mg^{2+} took roughly 20 seconds more (34 ± 3 sec). The data shown are an average of $n=115$ cells in Medium, $n=57$ cells in PBS wo Ca^{2+} and Mg^{2+} . The Student's t test between them was performed and the p values obtained was equal to $1.36 \cdot 10^{-17}$, underlying that the two samples are significantly different.

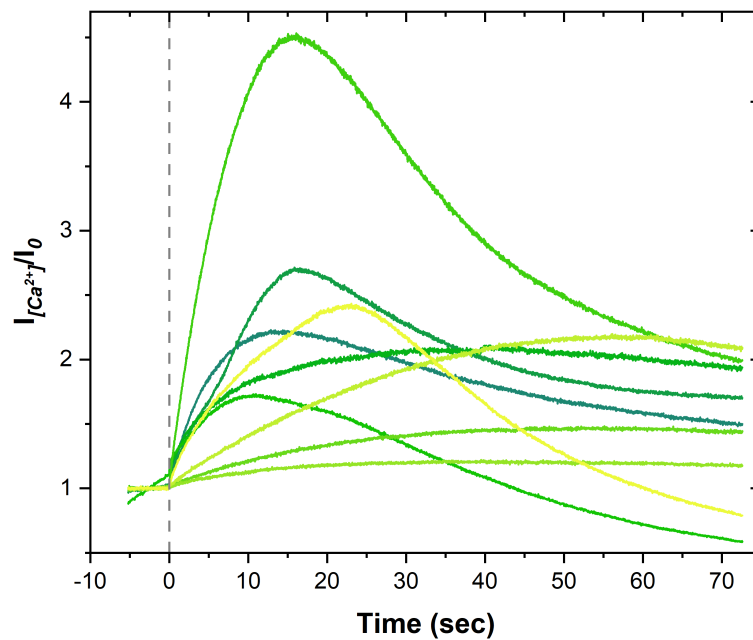


Figure 3.15: Normalized fluorescence intensity versus time of cells in PBS without Ca^{2+} and Mg^{2+} . The fluorescence is normalized over the first 201 frames before the laser shot ($t=0$). The grey dashed line represents the laser shot. Each line is a different cell. The graph displays 9 different samples collected on different experiments run on different days.

It is worth noting that, despite the difference in t_{max} , there was no significant change in the normalized measured maximum intensity (I_{max}/I_0). The I_{max} calculated for the samples in medium was 2.7 ± 0.2 a.u., almost the same as the one of the samples in PBS, equal to 2.8 ± 0.2 a.u.. The Student's t test had confirmed the observation with a calculated p value of 0.79.

The spreading of Ca microdomains was also observed in samples in PBS w/o Ca^{2+} and Mg^{2+} . The angular (**Figure 3.12**) and radial (**Figure 3.13**) distribution plots shown that Ca^{2+} microdomains in Ca^{2+} depleted samples were lower in intensity and spreaded less along the azimuthal coordinate compared to the samples in medium, while remaining localized near the plasma membrane with unaffected shape in a similar way as the medium.

3.3.2 Extracellular Ca^{2+} depletion: Synta66

The second strategy taken into place to induce an extracellular Ca^{2+} depletion was to treat Jurkat T cells with Synta66.

Briefly, T cells were incubated overnight with 50 μ L of gold nanostars. The day after, cells were washed with PBS and stained with Fluo4-AM. After removing the excess of dye, the cells were resuspended in Calcium Buffer with 50 μ M Synta66 and put in a coated petri dish. After 15 minutes, to allow the compound to completely inhibit the channel protein ORAI1, the sample was imaged with a confocal microscope. The instrument was set as for the other conditions. To confirm that the results obtained from the treatment were only related to it, two controls samples were also prepared. In the first one the cells were incubated in Calcium Buffer, while in the other one a volume of Dimethyl sulfoxide (DMSO) identical to that of Synta66 was added. Synta66 is dissolved in DMSO, therefore the second control was needed to assure that this organic solvent did not interfere with the experiment. The control samples were prepared, stained and imaged as described above.

As shown in **Figure 3.16**, the maximum intensity did not statistically differ between the sample and the controls while the time needed to reach the peak slightly did. The normalized intensity value was close to 4 a.u. in all the conditions (3.5 ± 0.3 a.u. for Synta66 treated, 4.1 ± 0.6 a.u. for DMSO and 4.1 ± 0.3 a.u. for Calcium buffer). The p values calculated with the t Student's test confirmed the non significant difference between the conditions. The obtained values were: $p=0.35$ between Synta66 and DMSO, $p=0.16$ between Synta66 and Calcium buffer and $p=0.98$ between DMSO and Calcium buffer. The data are an average of $n=76$ cells for Synta66 treatment, $n=36$ for DMSO treatment and $n=46$ for Calcium buffer. Regarding the t_{max} , all the conditions rapidly reached the maximum intensity. In detail, cells treated with Synta66 took 12.1 ± 0.8 sec to reach the peak, the one treated with DMSO 16 ± 2 sec and the control sample in Calcium buffer 15 ± 1 sec. While the difference between the sample treated with DMSO and the one left in Ca^{2+} buffer is not significant ($p=0.53$), the one between both Synta66 and DMSO and between Synta66 and Calcium buffer shows a low significant difference ($p=0.02$ and $p=0.06$ respectively). Even though the conditions show some significant difference between them (especially between Synta66 sample and DMSO or Calcium buffer), the t_{max} are all close to the one of the Medium sample ($t_{max}=13.2 \pm 0.8$, **Figure 3.14**) and have no significant difference with it. On the other hand, when these conditions are compared with PBS, they all reach the peak of intensity much faster than the sample in PBS ($t_{max}=34 \pm 3$).

The comparison between the different treatments (Medium, PBS and Synta66) can be observed in **Figure 3.14** where it can be observed more clearly how Synta66 treated samples behaved differently from the samples in PBS. That's surprising, because both conditions, albeit in different ways, would be expected to prevent the

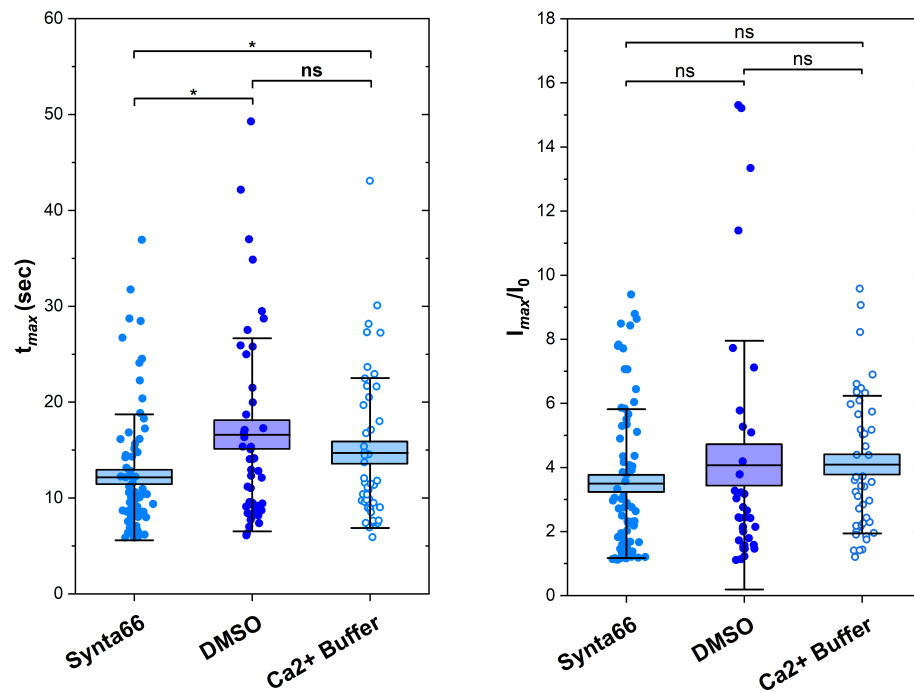


Figure 3.16: Time of the maximum intensity (t_{max}) and maximum fluorescence intensity (I_{max}/I_0) of samples treated with Synta66, DMSO and resuspended in Calcium buffer. The data shown are an average of $n=76$ cells treated with Synta66, $n=36$ cells treated with DMSO and $n=46$ cells in Calcium buffer. The Student's t test was performed and the p values obtained were the following. For the t_{max} plot, $p=0.02$ between Synta66 and DMSO treated; $p=0.06$ between Synta66 treated and Calcium buffer; $p=0.53$ between DMSO treated and Calcium buffer. For I_{max}/I_0 plot, $p=0.33$ between Synta66 and DMSO treated; $p=0.16$ between Synta66 treated and Calcium buffer; $p=0.98$ between DMSO treated and Calcium buffer. * = $p < 0.05$; ns = non significant.

uptake of calcium from the extracellular space. However the time needed for cells with Synta66 to reach the peak (12.1 ± 0.8 sec) was almost 20 seconds less than the time needed for samples in PBS wo Ca^{2+} and Mg^{2+} (34 ± 3 sec). The calculated p values confirmed that there was no significant difference in t_{max} between Medium and Synta66 treated samples ($p = 0.37$) while there was between PBS wo Ca^{2+} and Mg^{2+} and Synta66 samples ($p = 2.11 \times 10^{-15}$). Regarding the maximum intensity, while the values for samples in Medium and PBS are statistically the same, it increased in the samples treated with the drug. The I_{max} of Synta66 samples was 3.5 ± 0.3 a.u. against 2.7 ± 0.2 a.u. and 2.8 ± 0.2 a.u. for samples in Medium and PBS respectively. As before, the p values obtained by the Student's t test confirmed the statistical significance.

The spreading behaviour of the calcium microdomains was plotted in **Figure 3.12** and **3.13** with the other two conditions. In **Figure 3.12**, it can be observed that the angular distribution of Synta66 is similar to that of Medium in terms of the decrease in signal intensity over time. On the other hand, the breadth of the broadening of the distribution is similar to that of PBS, both slower than Medium. Regarding the radial distribution (**Figure 3.13**), it differs from that of all the other samples, suggesting

that calcium spreads more towards the centre of the cell rather than localising only in close proximity to the plasma membrane.

3.3.3 Ca^{2+} storage depletion: Thapsigargin

The depletion of Ca^{2+} storage was achieved treating the cells with Thapsigargin.

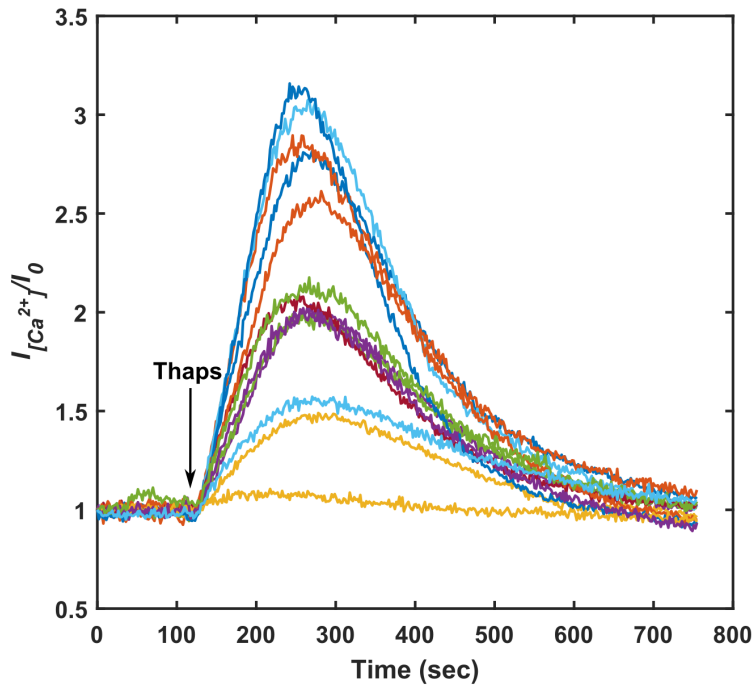


Figure 3.17: Effect of Thapsigargin on 13 different Jurkat T cells in the same field of view ($425.1 \mu\text{m} \times 425.1 \mu\text{m}$). Mean intensity of each cell normalized over the mean intensity of the cell at the first frame of the time lapse. The arrow marks the time when thapsigargin was added to the sample.

Before performing the experiment, the time required to complete emptying of the endoplasmic reticulum was validated. Samples were prepared as usual. Briefly, T cells (1×10^5 cells) were incubated o/n at 37°C with $50 \mu\text{L}$ of gold nanostars. The day after, cells were washed with PBS and stained with $6.5 \mu\text{M}$ of Fluo4-AM. After removing the excess of dye, the cells were resuspended in PBS w/o Ca^{2+} and Mg^{2+} . The sample was plated in a coated petri dish and left undisturbed for 15 min prior imaging. 3000 frames with a 25 msec frame rate were collected, at frame number 201 the 825 nm Mai Tai laser was shot for 25 msec with a variable laser power (0.2, 0.5, 2 or 5%). In order to simultaneously visualize multiple cells, a field of view bigger than usual was set. The image size was 1024×1024 pixels, equals to $425.10 \times 425.10 \mu\text{m}$. A video of 400 frames with a frame rate of 2 seconds was collected. After circa 2

minutes (160 sec or 60 frames), 1.67 μ M of Thapsigargin was added to the dish and the sample was recorded for another 11 minutes. As shown in **Figure 3.17** where 13 cells in the same field of view were taken into consideration, the fluorescence intensity started to increase simultaneously for all the cells after few seconds from the adding of the drug. Afterwards, the signal intensity began to decrease until it went back to the initial value. This result confirmed that a resting time of 15 minutes was enough to empty the ER storage and to allow the cells to go back to the basal signal.

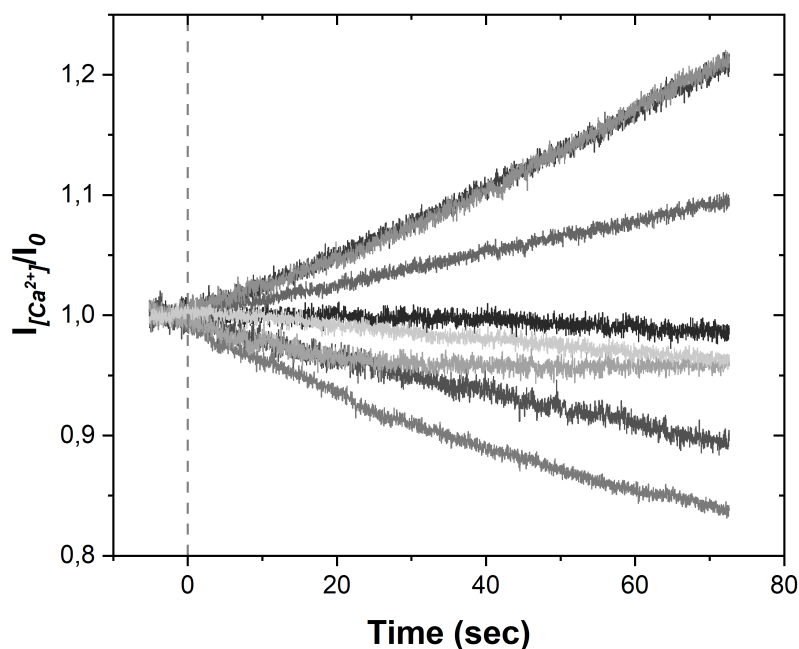


Figure 3.18: Normalized fluorescence intensity versus time of T cells treated with Thapsigargin. The fluorescence is normalized on the first 201 frames before the laser shot. The grey dashed line represents the laser shot. Each line is a different cell. The graph displays 9 different samples collected on different experiments run on different days.

After the validation of the appropriate treatment time, the experiment was performed as described above. The cells were imaged with the usual set up 15 min after the addition of the Thapsigargin. As expected, T cells treated with the drug failed to elicit the calcium release cascade. Therefore, when the normalized fluorescence intensity was plotted against the time no intensity peaks are visible (**Figure 3.18**) and samples were labeled as non responsive. Apart from the lack of a strong calcium release signal, this test was also aimed to check our capability of observing and isolating the beginning of the calcium cascade: the release of Ca^{2+} from the lysosomes where AuNSs were confined. Despite observed for other cells[100], this is not obvious in our case because the dimension of both the nanoparticles used and the cells tested is significantly smaller. The dimension of the gold nanostars is around 200 nm, therefore it was possible to presume that lysosomes with internalized nanoparticles would have approximately that size. Given the intrinsic resolution limit of confocal,

it is clear that it was not possible to clearly visualize the lysosomal signal which, despite calcium deprivation, is lost in the background. Then, MATLAB software was used to try to extrapolate it from the basal signal (cfr. **Section 2.7**). To do so, different regions of the cells were compared to each other and subtracted in order to bring out the slightest difference in signal intensity. Nevertheless, it was not possible to localize any bright starting spot.

3.4 Effect of Ca^{2+} release on cell dimension

Figure 3.8, that was essential for visually describing the calcium release and for the identification of Ca^{2+} microdomains, brought the attention on a unexpected phenomenon. The background subtraction in **Figure 3.8** uncovered a brighter halo around the cell on the third and fourth images, i. e. the time of the maximum intensity peak ($t=9.779$ s) and the decrease of the signal ($t=25.940$ s) respectively. At first glance, the halo seemed to suggest the accumulation of a great amount of calcium ions at the cell membrane. In-depth studies on the cell dimension over time have proven that this halo was an artefact.

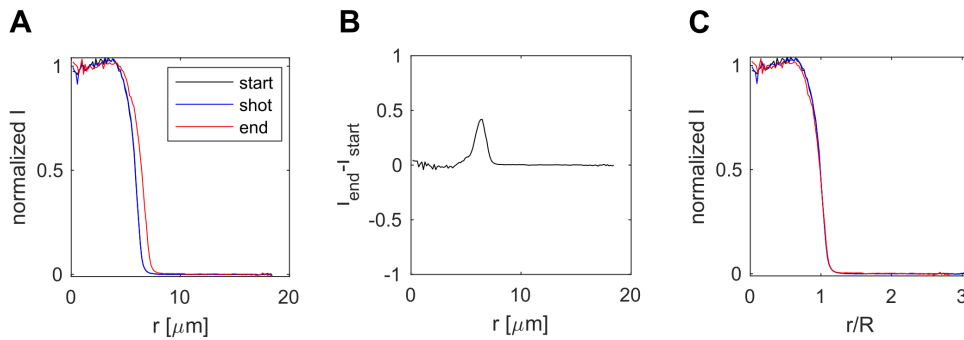


Figure 3.19: Radial coordinate at three time points the start (black line), the shot of the laser (blue line) and the end (red line). A) Normalized intensity of the cell plotted against the radial coordinate (r). B) Subtraction of the initial intensity profile (I_{start}) to the final one (I_{end}) plotted versus the radial coordinate (r). C) Normalized intensity plotted against the radial coordinate (r) normalized on the cell radius (R).

To come to this conclusion, the trend of the radial coordinate and the cell intensity were studied over time (cfr. **Section 2.7**). In **Figure 3.19A**, the normalized intensity was plotted against the radial coordinate and the three major time points of the experiment were studied: the start (black line), the shot of the laser (blue line) and the end (red line). It can be observed that during the beginning of the experiment and the laser shot the radial profile does not change while at the end a radial shift appears corresponding to an increase of cell radius. The subtraction of the initial intensity profile (I_{start}) to the final one (I_{end}) in **Figure 3.19B** allowed to visualize how that radial shift results in a peak localized at the cell border. In this way, by looking only at **Figure 3.19B**, it may seem that there is a calcium accumulation over time. The **Figure 3.19B** is a 1D representation of what can be seen in the background subtraction in **Figure 3.8**. To check if halo was only due to the increase of the cell radius, the normalized intensity was plotted against the radial coordinate normalized on the cell radius (R). The plot in **Figure 3.19C** showed that, when the changes in cell

dimension are not taken into consideration, all the lines overlap almost completely thus excluding the presence of Ca^{2+} accumulation.

In **Figure 3.20A**, it is possible to see the radius variation over time for three different cells (expressed as a percentual variation compared to the starting radius, R) over time. The graph shows that on long period of times the radius increase in each cell. The comparison of the plots of the radius over time with the corresponding graph of the cell intensity over time (**Figure 3.20A** and **B**) underlines that even though cells shown different maximum intensity they all increased their diameter at the end of the experiment. The increase of the cell dimension over time (obtained by dividing the radius at the end of the experiment, R_{end} , by the radius at the beginning of it, R_0) was calculated for all the condition and plotted. In **Figure 3.20C**, it is possible to observe that the cells in Medium, PBS wo Ca^{2+} and Mg^{2+} and treated with Synta66 increase on average their dimension of of ≈ 5 -15%.

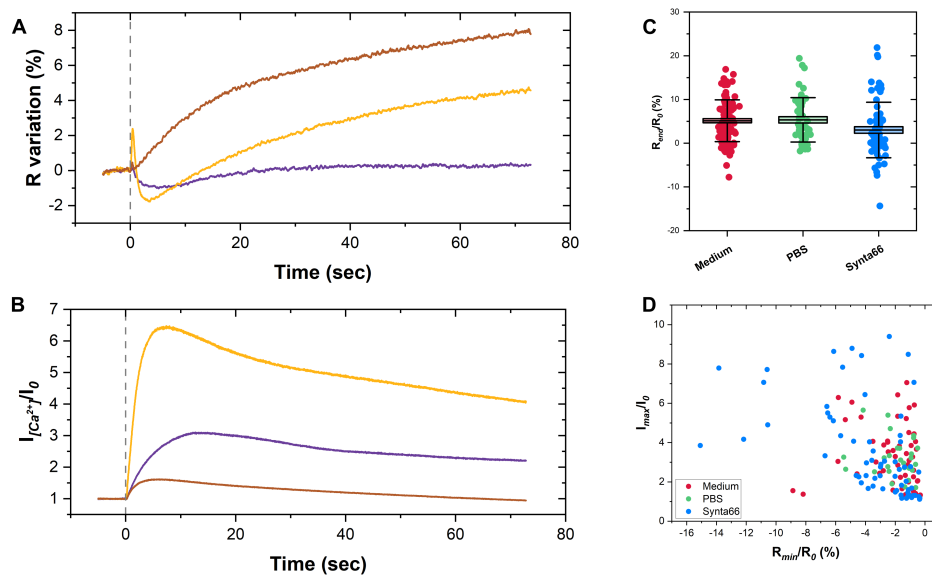


Figure 3.20: Radius variation upon stimulus. A) Radius variation (in percentage) over time. Each line represents a different cell. The dashed line represents the laser shot. B) Normalized intensity over time. Each line represents a different cell. All the cells displayed are the same as A. The dashed line represents the laser shot. C) Radius increase in percentage obtained normalizing the final radius (R_{end}) on the initial radius (R_0) of samples in Medium (red), PBS wo Ca^{2+} and Mg^{2+} (green) and Synta66 (blue). D) Scatter plot of the normalized intensity and the normalized minimum radius (R_{min}) with the tested conditions: Medium (red), PBS wo Ca^{2+} and Mg^{2+} (green) and Synta66 (blue).

Although they behaved similarly over long periods of time, the cells reacted differently at short time scales after the laser shot in terms of their size. Moreover, different behaviours were found for different cells. Focusing on the the first 10 sec after the laser shot in **Figure 3.20A**, it is possible to notice that some cells reacted to the stimulus with a rapid shrink before starting to increase their size. Contrary to what is observed for the final radius, this shrinkage seems to be related to the total intensity of the cell. Comfronting **Figure 3.20A** and **3.20B**, it can be observed that the cell with the higher intensities (yellow line) had also the bigger shrink. To confirm the correlation between the intensity and the minimum radius (R_{min}), a scatter

plot with the tested conditions (Medium, PBS wo Ca^{2+} and Mg^{2+} and Synta66) was created (**Figure 3.20D**). In **Figure 3.20D**, the samples with lower maximum fluorescence intensity show a normalized minimum radius between -2 and 0 %, Whereas cells with higher signal intensity decrease their radius to the 12/10 %.

Chapter 4

Discussion, conclusions and outlooks

This chapter summarizes the obtained results and gives an interpretation and explanation in light of the thesis' objective and previous knowledge. Future steps needed to complete the work will also be highlighted.

The aim of the work presented in this dissertation was to induce the release of calcium in T cells exploiting the photothermal properties of the gold nanoparticles. To this end, Jurkat T cells were treated with gold nanostars. Using a laser with the appropriate wavelength, the surface plasmon resonance of the AuNSs, localized in the endolysosomes, was stimulated. The subsequent temperature increase of the nanoparticles and its surroundings led to the formation of small and transient pores on the endolysosome membrane and to the leakage of Ca^{2+} into the cytosol. This small localized calcium increase mimicked the Ca^{2+} microdomain and triggered the global rise of calcium, via SOCE. The release and the increase of calcium were studied in detail from the first moments after the laser stimulation up to its decrease after a few minutes. Special attention was paid to the isolation and visualization of the calcium component of lysosomes.

Gold nanostars were chosen to carry out this work for two main reasons: their dimension and the positioning of their SPR peak. One of the starting points for this dissertation was the work of Zhu and coworkers [100]. In Zhu's publication, the AuNSs were integrated into a multi-layered polymer structure with a dimension of approximately 4 μm . However, this structure could not be exploited in the present work due to the smaller size of the T cells (5-10 μm) compared to the HeLa and MCF7 cells (50-100 μm) utilized by Zhu. On the other hand, plain AuNSs have an average dimension of 200-250 nm, which made them optimal for the uptake by T cells. Moreover, AuNSs display an SPR peak in the NIR region of the spectrum (**Figure 2.1**). NIR light does not interact with biological samples, thus it's the optimal wavelength to exploit in *in vitro* (and *in vivo*) experiments. The presence of sharp tips, that can be observed in the SEM images (**Figure 2.2**), enhanced the SPR effect making the nanostars one of the most efficient photothermal vector.

The propagation of calcium ions was observed using a fluorophore that exhibited increased fluorescence upon binding with free calcium ions. This fluorophore allowed real-time visualization of calcium spreading within the cell. By monitoring the mean fluorescence intensity inside the cell over time, a graphical representation of the calcium increase was shown for different cells (**Figure 3.1**). Prior to stimulation, the normalized cell intensity always remained at the basal level. Following

laser stimulation of the gold nanostar, the fluorescence rapidly increased to a peak within a few seconds, correlating with the maximum calcium concentration within the cell. Subsequently, the signal decreased. Although all cells showed the same intensity profile, there was a considerable variability in the overall intensity among different samples and even within the same sample. This is due to the intrinsic biological diversity among cells. Notably, Jurkat T cells can respond more than once to the same stimulus (**Figure 3.2**). This can be achieved by giving the cells time to replenish their stores (especially the ER). Nevertheless, the subsequent responses may vary significantly in terms of intensity and duration compared to the first response.

Although the small size of the nanoparticles was a desired feature, it raised some problems regarding their visualization at the microscope. The confocal microscope has an intrinsic resolution limit and, which unfortunately makes it impossible to detect AuNSs inside the cells. Nevertheless, it was possible to observe dark agglomerates in the cytoplasm, especially in proximity to the plasma membrane (**Figure 3.5**), which are most likely aggregates of nanoparticles. The presence of AuNSs inside the cells was confirmed by two experimental evidences. The first one was the presence of a huge amount of gold atoms, quantified by mass spectrometry, in treated cells compared to the untreated ones (**Figure 2.5**). The second was that only cells treated with nanostars were able to respond to the laser stimulation, even though no particles could be visualized inside the cells. While the untreated cells were all unresponsive (**Figure 3.4**). The inability to see the particles inside the cells made necessary to optimize the stimulation protocol. The size and position of the laser spot can be adjusted by the operator. Initially, the laser spot (referred to as small laser spot) was placed only on visible dark agglomerates, that correlated with the AuNSs or aggregation of AuNSs. Only few cells shown such clear feature, so that it was not possible to get a good statistical sample for analysis. Therefore, a different strategy was adopted: irradiating the entire cell with the laser (referred to as large laser spot). The responsive cells stimulated with either a small or a big laser spot showed the same maximum intensity and took the same time to reach the peak, proving that laser's dimension did not affect the outcome of the stimulation (**Figure 3.6**).

Overall, how the cells responded to the stimulation, in both terms of responsiveness and survival, depended on several factors. Responsiveness was defined as the rapid increase in fluorescence intensity upon stimulation. The observed responsiveness was above 50% for all conditions tested (**Figure 3.7**). However, these data are susceptible to misinterpretation because they consider all stimulated cells without taking into account whether they actually contained nanoparticles. For this reason, some cells identified as unresponsive may simply be cells that did not take up nanoparticles and thus were unable to interact with the laser. In terms of survival, how Jurkat cells responded to the temperature increase caused by laser interaction with AuNSs depended not only on the amount of NPs taken up but also on the well-being of the cells. For example, newly thawed cells tended to have a more dramatic response to the stimulus, specifically dying after a few msec or seconds.

In order to isolate and examine the lysosomal component within the overall calcium signaling pathway, the primary contributors to this pathway — extracellular calcium and calcium stored in the endoplasmic reticulum (ER) — were intentionally disrupted. Depletion of Ca^{2+} was achieved through various strategies.

To make cells insensitive to the extracellular calcium, they were either left in a PBS buffer without calcium and magnesium ions or treated with Synta66, an inhibitor of ORAI1. Elimination of the extracellular component in the global calcium signal implies that the calcium release observed in treated samples after stimulation comes from only two components: the lysosomal component and the endoplasmic reticulum component. Calcium-deprived cells were still able to respond to the

photothermal stimulus and exhibited a signaling pattern similar to untreated cells (**Figure 3.15**). Interestingly, the two treatments, expected in principle to give the same results, showed significant differences. T cells in PBS wo Ca^{2+} and Mg^{2+} took longer (approximately 20 seconds more) than those in complete medium (Medium) to reach the peak of intensity, although they displayed the same maximum intensity (**Figure 3.14**). Whereas Synta66-treated samples did not show this shift in the time needed to reach the peak. Currently, there is no a definitive explanation for the behavior of the samples, but several hypotheses can be proposed. The delay in the peak shown by the samples in PBS is directly related to the importance of the extracellular calcium in SOCE and its self-maintenance. After the stimulation, the opening of the channels on the ER induces the activation of the CRAC channels on the PM. However, the lack of extracellular Ca^{2+} delays the reaching of the peak because the cells reach it only by completely depleting the ER store. On the other hand, Synta66-treated samples are not able to activate CRAC channels, but are immersed in a buffer containing calcium, so that extracellular calcium is still available. Since the time of the peak in Synta66-treated samples is similar to that of samples in complete medium, this means that the extracellular calcium component is still involved in the dynamics of signal intensity despite ORAI1 inhibition. The lysosomes, where the nanoparticles are located, are close to the plasma membrane. Therefore, when the nanoparticles heat up, their heat diffuses and may affects not only the lysosomal membrane but also the plasma membrane. This may lead to transient disruption of the plasma membrane or activation of another type of calcium channels, that are not part of the CRACs. Among the various channels involved in calcium signaling, there are also temperature-sensitive channels [165]. These channels can respond to small or large changes in temperature, resulting in the flow of ions within the cell. The most studied ion channels in Jurkat T cells belong to the family of transient receptor potential (TRP) channels and are mostly located at the level of the plasma membrane [166, 167]. It is therefore plausible that the local temperature increase induced by the irradiation of gold nanostars triggers the opening of the temperature-sensitive calcium channels, effectively bypassing the inhibition of the traditional entry pathway via CRAC channels. The involvement of the extracellular calcium is further supported by the fact that Synta66-treated cells show only a slight difference from their controls, cells treated with DMSO or untreated but left in the same buffer in the presence of calcium respectively (**Figure 3.16**). However, it remains to be explored which of the two hypotheses explains why the time to peak in Synta66-treated samples differs from that of samples in PBS without Ca^{2+} and Mg^{2+} .

To isolate the lysosomal component, Jurkat cells in PBS wo Ca^{2+} and Mg^{2+} were treated with Thapsigargin. Thapsigargin, an inhibitor of SERCA, was utilized to induce ER depletion, hindering its replenishment. Cells pre-treated with Thapsigargin before laser stimulation exhibited an initial rise in intracellular calcium levels followed by a subsequent decline until returning to basal levels (**Figure 3.17**). Subsequent laser stimulation failed to trigger the calcium signaling cascade and no peak was observed, as expected since the major sources of calcium were removed (**Figure 3.18**). Despite efforts to isolate lysosomal calcium, it remained undetectable. Multiple attempts were made to discern it, but nothing above the background level was detected. It is important to emphasize that Zhu *et al.* were successful in demonstrating calcium release (as reported in their publication [100]) because they used particles in the micrometer range and therefore the lysosomes were swollen and easier to identify and isolate. In the present work, both the particles used and the lysosomes were smaller, close to the detection limit of the system.

The image data analysis of the first few minutes after the laser stimulation resulted in a detailed visual description of the Ca^{2+} dynamics inside the cells (**Figure**

3.8). Looking at the picture obtained after the analysis, it was possible to see small calcium fluctuations in T cells in resting state. While immediately after the laser stimulation, the Ca^{2+} microdomains could be precisely visualized. Remarkably, in some samples two separately Ca^{2+} microdomains were identified. This suggested the presence inside the cells of two AuNSs (or aggregates of AuNSs) that were stimulated at the same time.

These Ca^{2+} microdomains exhibited a peculiar fluorescence intensity profile compared to the overall cell intensity (**Figure 3.10**). Their intensity increased more rapidly than of the entire cell and blended in the global intensity after few seconds, before reaching the global intensity maximum. Since it was possible to isolate the microdomains signal from the background, a detailed study of Ca^{2+} dynamics could be carried out. Notably, Ca^{2+} microdomains exhibited an intensity peak relative to the global cell intensity within 0.10 sec in samples maintained in complete medium and treated with Synta66 (**Figure 3.11**). On the contrary, the time taken to reach the peak of Ca^{2+} microdomains in the samples in PBS without Ca^{2+} and Mg^{2+} was 0.24 seconds, slower than that observed in the medium and Synta66-treated samples. This observation aligns with previous findings regarding global calcium signaling, highlighting the impact of extracellular calcium not only on the global dynamics but also on that of Ca^{2+} microdomains. The spreading of the microdomains over time were investigated along two directions: angular and radial.

In the angular direction, microdomain distribution remained centered at the starting angular position while spreading along the plasma membrane (**Figure 3.12**). The spreading of calcium microdomains isn't merely a result of passive calcium diffusion, as calcium is buffered within the cytoplasm [74]. Instead, it's the calcium itself that drives its own propagation through the activation of calcium channels situated at the plasma membrane. In the samples in PBS wo Ca^{2+} and Mg^{2+} , the time to reach peak intensity of Ca^{2+} microdomains and of the global signal was prolonged compared to samples in a complete medium. Additionally, the spread of microdomains was lower due to the absence of extracellular calcium. The global signal was sustained solely by the ER and lysosomes, along with microdomain propagation, as there was no influx of calcium to support and amplify spreading, despite calcium channels on the plasma membrane being activated. Conversely, samples treated with Synta66 reached both peaks at the same time as the sample in medium, while displaying a spreading of the Ca^{2+} microdomain comparable to that of samples in PBS wo Ca^{2+} and Mg^{2+} . The data indicate that in Synta66-treated samples, Ca^{2+} microdomains remained localized at the starting point. This confinement was likely due to the inhibition of ORAI1, which prevented the Ca^{2+} entry from this channel, thus preventing its diffusion and self-propagation, and the subsequent activation of channels on the plasma membrane.

On the other hand, the radial distribution showed that the microdomains didn't diffuse very much towards the center of the cell (**Figure 3.13**). This could be due to two reasons. The first is that calcium diffuse poorly inside the cytoplasm because it is buffered. The second reason is that T lymphocytes' cytoplasm is largely occupied by the nucleus, therefore there is no place for calcium to spread.

The data analysis, especially the background subtraction, showed an interesting bright halo around the cells on long times, after the cell had already reached the peak (**Figure 3.8**). Initially, it was hypothesized that the halo was a localization of the calcium at the plasma membrane. However, further analysis on the cell dimension over time showed that it was an artefact (**Figure 3.19**). After the stimulation, the cells rounded and increased their size of 5 to 15% (**Figure 3.20C**). That was observed for all the samples in all the conditions. Many references can be found in the literature regarding the changes in shape of T cells (such as elongation, increase in

roundness and flattened). These conformational changes are directly linked with the immune-synapse formation and T cell activation [168, 169, 170]. This observation suggests that the laser stimulation did not only induce the increase of the calcium inside the T cells but also a full-fledged lymphocyte activation. Even though all the cells increased their dimension on long times, a shrink can be observed in some of them right after the laser shot. The initial shrink correlates with the cell fluorescence intensity (**Figure 3.20**). Cells with higher intensity displayed a larger shrink. The correlation has not an explanation to this day.

Overall, all the data collected in this dissertation shows gold nanostars as a promising tool for inducing the release of calcium in Jurkat T cells. AuNSs are efficiently uptake by the T cells and stimulated with a laser inducing the global release of calcium. The calcium release was spatially and temporally monitored. Through statistical analysis and evaluation of different conditions, the presence of a maximum peak was verified, whose intensity shows great variability, while the time to peak was typical in each condition. These findings suggest that photothermal heating mediated by the nanoparticles plays a role in the fluidification of the lysosomes. However, while trying to isolate the lysosomal signaling, it was observed that the photothermal heating also induced fluidification of the plasma membrane or activated thermosensitive calcium channels localized at the plasma membrane. Although this indicates that the method presented in this work offers a promising approach to studying calcium release and spreading, providing a simpler and more precise alternative to biological or chemical methods, further research is needed to fully comprehend the cellular effects during photothermal heating. First, other chemical inhibitors (such as Gadolinium chloride) can be exploited to clarify if the laser irradiation induces the fluidification of the laser membrane or if thermosensitive channels are involved in the calcium signaling. In case of the involvement of thermosensitive channels, it would be of great interest to identify them. Moreover, to visualize the calcium release from lysosomes, the linking of a fluorophore on the gold nanostars would help the co-localization of the nanoparticles with the lysosomes. The localization would also help a more precise stimulation and, perhaps, the stimulation of more than one nanostars (or aggregates of nanostars) in the same cell in different moments. Regarding the cell activation, other markers could be monitor (such as IL-2 production) to further investigate it.

Chapter 5

In silico drug discovery

5.1 Introduction

Traditional *in vitro* drug discovery methods have always generated big costs in terms of lab materials and manpower. Even with the advances in robotics and high-throughput inhibition/binding techniques, the identification of potential targets has been deficient in cost-efficiency ratios. This is due to the elevated cost and time required, not only in the first stages of target screening but also in the next steps of clinical phase trials. In the last decade the development of computer-aided drug discovery (CADD) has become a game-changing process decreasing the risk in drug development by increasing its effectiveness and reducing time and budget costs [171]. *In silico* methods were born based on the examination of the chemical structure of proteins and small molecules, determining the different features that can be responsible for its biological activity and the interactions that can exist among them. All this information is used not only to evaluate ligand-protein interaction but also to model proteins, predict potential protein binding sites and both biochemical (physicochemical and ADME properties) and clinical (side effects, selectivity) characteristics. The protein-drug interactions will made us able to easily and fast discriminate and elucidated a small number of targets to test *in vitro*. Despite the enhanced velocity, *in silico* approaches still need human supervision and its combination with other state of the art methods. Interestingly CADD is a helpful tool not only on identifying new drugs but also on drug re-purposing of compounds that have being used before for the treatment of similar or different diseases [172, 173, 174]. Measurements of intramolecular and intermolecular forces, binding delta-free energies and conformational changes prediction will be the most power consuming stage of the entire process. Finding and selecting metabolic targets and possible drugs, combining with high-throughput screening (HTS) methods have reduced the time and budget costs of the whole drug discovery field. This treatment will reduce the economic burden and the time of the nowadays *de novo* drug discovery.

5.2 *In silico* pipeline

The road to find a drug candidate for a specific target is made by subsequent and interlinked steps. These steps can be group based on their goal: target definition (determination of target structures and ligands), screening and defining target-ligand pair (determination of active sites/binding sites, molecular docking and pharmacophore determination) and chemical validation (ADME/T characterization) (**Figure 5.1**).

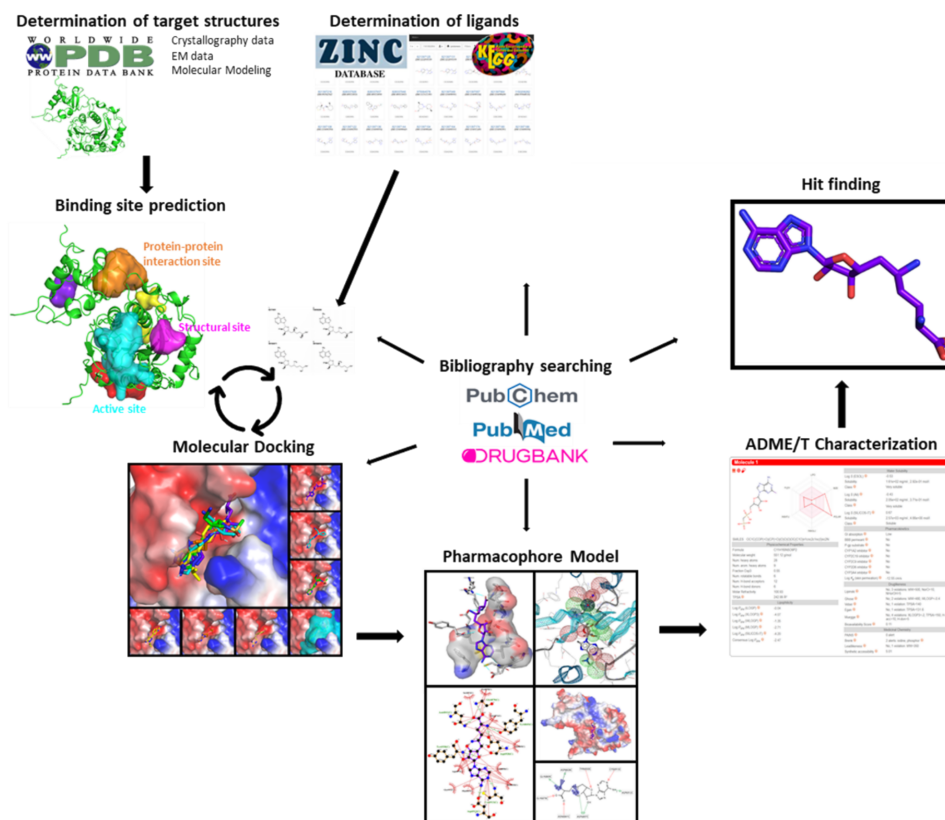


Figure 5.1: Workflow of an in silico pipeline, from the determination of target structures and ligands steps to the final drug best hit finding.

1. Determination of target structures

To determine the 3D configuration of the target protein, X-Ray and high resolution Cryo-EM structures should be the most trustable data to start with. X-Ray crystallography generates highly confident data with extremely high resolution (with an upper limit of 0.48 Å[175, 176]), however not all protein or protein complex can be crystallized. Despite a slightly lower resolution (upper limit 0.6 Å[177]), Cryo-EM gave the opportunity to obtain the structure of proteins that could have not been crystallized and macro complexes higher than 10 MDa. When the protein structure is not available, sequence-based 3D prediction methods are valuable strategies to predict some structural features. Despite their extreme accuracy, they cannot define the exact relative position of the different amino acids and/or DNA in the molecule and this could affect the validity of the results.

2. Determination of ligands

For the identification of potential ligands, it can be very useful to first understand the role of the target protein inside the cell and/or pathway. There are different databases that can be used depending on the goal of the study. In the case of drug repurposing scenario, databases of already tested and approved drugs should be used, as the WHO Model Lists of Essential Medicines[178]. However, in “the *novo* finding”, any other public and private database could be used too where millions of compounds can be found as KEGG or ZINC databases[179, 180]. These drug databases can be screened using as criteria the known activities of the compounds.

Drug/ligand structures were constantly deposited in the DrugBank database, which is a freely accessible and contains information on drugs and their targets[181].

3. Determination of active/binding sites

Usually, three main binding sites can be identified inside the protein structure: 1- Active site or related to its active site. Will be regions of the protein where its substrate (other protein, nucleotides, or small molecules) will bind or will help to interact with, as active or allosteric binding sites. 2- Structural sites, key regions for protein stability, folding or activity-related conformational changes. These sites can be located either close or far from the active sites and sometimes cannot be rationally easy to define. 3- Protein-protein interaction sites. Regions that are involved with its binding or interaction with other proteins, either in a transient or in a stable way. Either by using structural information available or biochemical and biophysical determination (binding site description, inhibition, mutagenesis studies) the region of interest into the protein structure can be easily defined. In cases of absence of some part of this information, computer aided methods will be crucial for establishing the region of interest. Sites as The Computed Atlas for Surface Topography of Proteins (CASTp)[182] and Metapocket[183], will help to Identify cavities on proteins with potential interest.

4. Molecular docking

Different software also can be used for analyzing drug-protein docking. Firstly, both ligand and protein should be prepared and optimized (removing waters of protein structures and examining ligand geometry), which can be done in several structure analysis software (PyMOL, Chimera, AutoDockTools)[184, 185]. The more accurate docking analysis should find the higher and best scoring-ranking-docking-screening power. Several software, such as AutoDockVina[186], give highly accurate and robust results that can give us proper confidence of the quality of the docking. The outputs consist in 3 parameters: affinity (expressed in kcal/mol) and the average deviation between the corresponding atoms of the molecule and the protein (RMSD upper bond and lower bond). The candidate drugs will be sorted based on affinity and RMSD values. It's up to the operator to define threshold values.

5. Pharmacophore determination

Pharmacophore models define the characterization of the steric and electronic features necessary to ensure the interactions between protein-drug for triggering/block its biological response, explaining how ligands can bind to a receptor site[187]. Knowing the 3D arrangement and features in the bio-active molecule (drug), will help in the finding and designing of improved compounds. Structurally conserved characteristics of different drugs can be responsible for their biological activity interacting with a specific protein target. Identifying a common pharmacophore in a compound library will allow us to define all possible conformations between the ligands and the protein. This steric information will drive us to identify the most favorable binding conformation for everyone, comparing them and finding the general and common molecular arrangements of the ligand into the binding site.

6. ADME/T characterization

The capacity of a selected drug to be effective in the body depends on its ability to reach its target in sufficient concentration, remaining in a bioactive form the time needed for generating its expected biochemical activity. The final stage of drug development involves the determination of ADME/T characteristics. Computer models can also increase the velocity of drug discovery at this stage, avoiding the necessity of *in vitro* experiments. Software packages, like SwissADME web tool[188], generate robust predictive models for the determination of ADME properties of a small molecule. Variables like its pharmacokinetics, physicochemical properties, medicinal chemistry friendliness and drug-likeness are key for describe the capability of

the drug for overcome its final screening step.

5.3 Case study

The final goal of this work was to investigate the possibility of finding molecules able to interact with the biochemical pathway that leads to the release of Ca^{2+} from the endoplasmic reticulum (ER) and lysosomes in T cells subsequent their activation by antigen presenting cells (**Figure 5.2**).

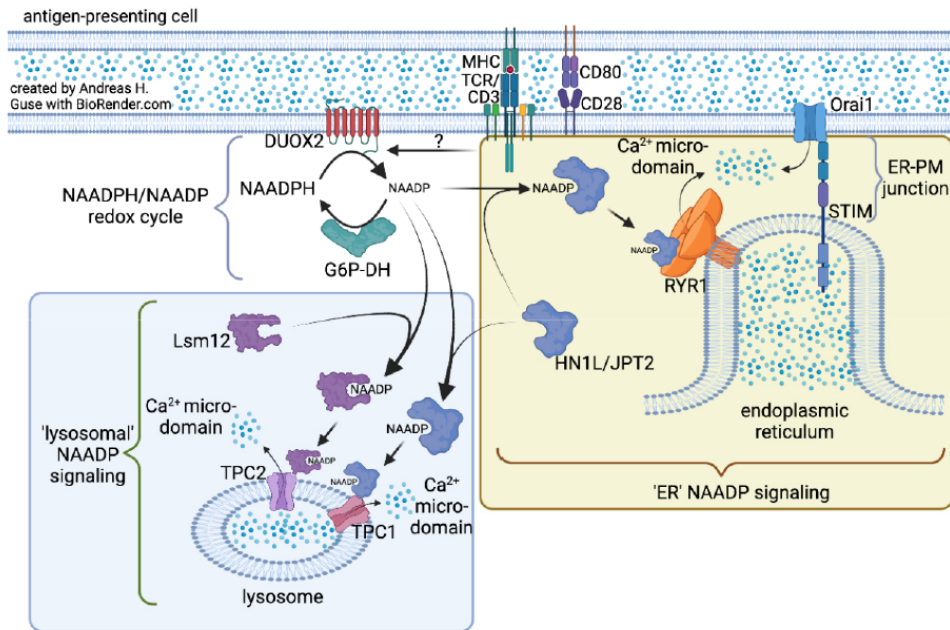


Figure 5.2: Ca^{2+} mobilization by NAADP mediated by NAADP receptors and binding proteins linking to different organelles and ion channels, upon T cell activation. Image from ref. [79].

Firstly, four key pathway components were identified: DUOX2, LSM12, HN1L/JPT2 and RYR1.

Among them, DUOX2 was dismissed from the beginning. Since it is an upstream component of the pathway, its impairment could lead, during the *in vitro* testing, to the unwanted disruption of others signaling routes and/or cell death.

The focus was then put on HN1L/JPT2 protein because its involvement in both release pathways. Following the *in silico* pipeline described above, the program AlphaFold was used to determine the protein structure. The result was disappointing since there was no available Cryo-EM or X-Ray crystallography data and most of the structure was unreliable (**Figure 5.3**). Phyre program was exploited to look for folding similarity with other proteins but none was found. HN1L/JPT2 protein was then discard because there was not enough structural information.

On the other hand, LSM12 presented a better structure in AlphaFold even though it was partial (**Figure 5.4**).

To have a better understanding, Phyre was used to identify similarity with other proteins and if there could be a useful active/binding site. Few proteins were found

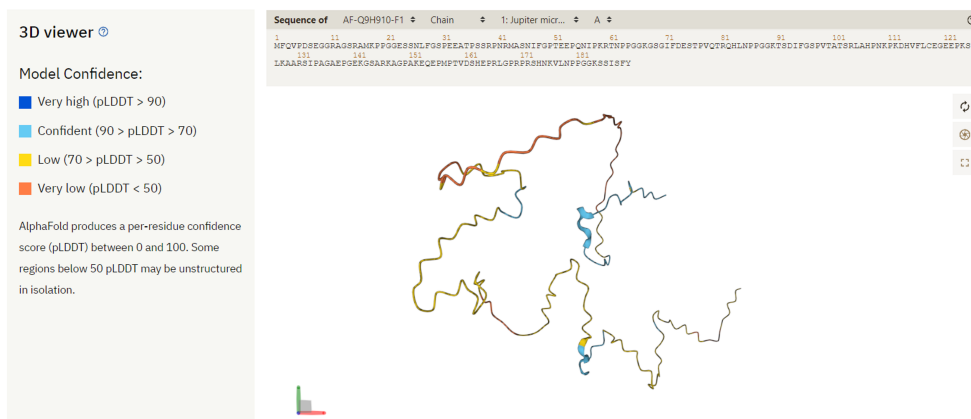


Figure 5.3: HN1L/JPT2 structure produced by AlphaFold program.

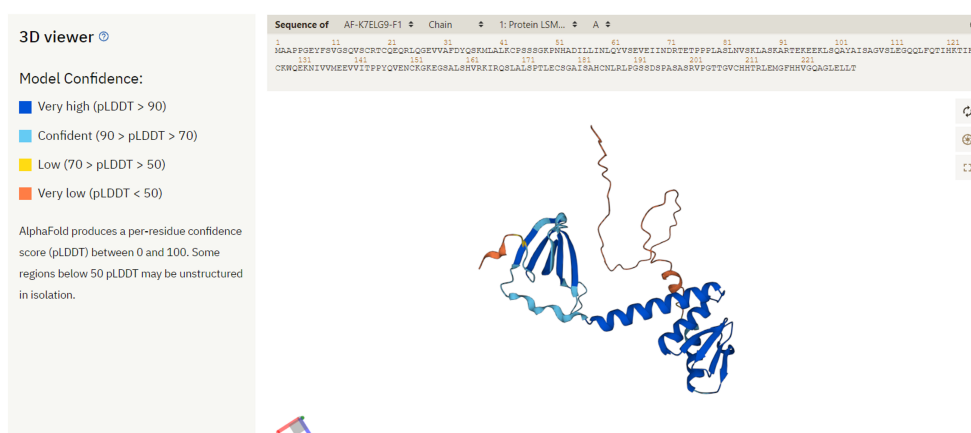


Figure 5.4: LSM12 structure produced by AlphaFold program.

to hold some similarity (around 20/25 %), suggesting the presence of potential binding sites in LSM12 protein (Figure 5.5).

Since no hypothetical ligands was determined, a broader database was used to increase the chances of a good match. The chosen database was ZINC. Inside of it, it was possible to narrow the dataset on the compounds already approved by FDA.

The possible binding sites were determined using PrankWeb and Cavity Plus. These programs give all the possible docking sites solely based on the protein structures. This means that they potentially identify a binding site positioned in an unreachable part of the protein. Therefore, it is needed a human screening of the identified potential sites to rule out the least probable and keep on working of the ones that could lead to higher success binding rate. Inside LSM12 structures four binding pockets were identified. To position these pockets in the structures their x,y,z coordinates must be found. Chimera program is able to do it by virtually creating a cube containing the pocket (Figure 5.6). The cube can be modified to better fit the structure.

Once the coordinates of all the binding sites are obtained it's possible to move on to the molecular docking. AutoDockVina was exploited to identified possible binding molecules for each site by loading into the program the site coordinates and the ZINC molecules file. The output is made by a file where the affinity and the av-


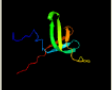
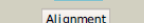
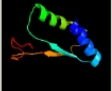
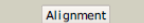

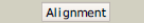

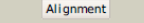
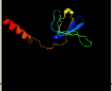
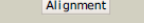

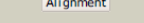
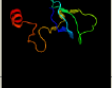
#	Template	Alignment Coverage	3D Model	Confidence	% I.d.	Template Information
1	c2vxeA	 Alignment		93.2	22	PDB header: transcription Chain: A; PDB Molecule: cg10686-pa; PDBTitle: solution structure of the lsm domain of drosophila 2 melanogaster tra1 (trailer hitch) PDB Entry: PDB RCSB PDBj
2	c3lhiA	 Alignment		37.1	25	PDB header: hydrolase Chain: A; PDB Molecule: putative 6-phosphogluconolactonase; PDBTitle: crystal structure of putative 6-phosphogluconolactonase(yp_207848.1)2 from neisseria gonorrhoeae fa 1090 at 1.33 a resolution PDB Entry: PDB RCSB PDBj
3	c2vc8A	 Alignment		95.2	25	PDB header: protein-binding Chain: A; PDB Molecule: enhancer of mra-decapping protein 3; PDBTitle: crystal structure of the lsm domain of human edc3 (enhancer2 of decapping 3) PDB Entry: PDB RCSB PDBj
4	d2zjrm1	 Alignment		37.3	19	Fold: SH3-like barrel Superfamily: Translation proteins SH3-like domain Family: Ribosomal protein L19 PDB entry: PDB RCSB PDBj
5	c5uz5K	 Alignment		83.9	15	PDB header: nuclear protein/rna Chain: K; PDB Molecule: small nuclear ribonucleoprotein-associated protein b; PDBTitle: s. cerevisiae u1 snrnp PDB Entry: PDB RCSB PDBj
6	c4c92A	 Alignment		88.5	13	PDB header: transcription Chain: A; PDB Molecule: sm-like protein lsm1; PDBTitle: crystal structure of the yeast lsm1-7 complex PDB Entry: PDB RCSB PDBj
7	c3jcr2	 Alignment		88.9	18	PDB header: splicing Chain: 2; PDB Molecule: lsm2; PDBTitle: 3d structure determination of the human* u4/u6.u5* tri-snmp complex PDB Entry: PDB RCSB PDBj

Figure 5.5: LSM12 folding similarity by Phyre.

erage deviation between the corresponding atoms of the molecule and the protein (RSMD) are listed. The highest binding affinity receives the chosen value of RSMD equal to 0 and it is considered the control position to evaluate the RSMD values of the all the other possible positions of the drug inside the pocket. To evaluate if the binding between the protein and the drug is good a threshold, for both affinity and RSMD, must be set. The threshold is set based on experience and can change depending on the drug characteristic (size, charge ... etc) and the software in use. The docking analysis of ZINC candidates on LSM12 binding sites selected few possible molecules, however the threshold evaluation excluded all of them. It was not possible to find any suitable candidate within the chosen dataset. For this reason, LSM12 was also dismissed.

RYR1 was chosen as the last target of this study. Unlike the other proteins considered, RYR1 is a transmembrane channel and a multimeric complex. It is made by 4 identical monomers that create a bouquet-like structure where the bottom part constitutes the channel porous and the upper part interact with HN1L/JPT2 (Figure 5.7). This complex structure created a new challenge: how to handle a huge protein? Different strategies can be adopted and they depend on how the protein is looked at.

The complex can be disassembled using PyMol and each portion can be studied separately. Since the transmembrane portion is the one that creates the pore throughout Ca²⁺ is been released from ER, it was chosen for the study (Figure 5.8).

ZINC dataset was the same used in the study of LSM12. Exploiting Cavity Plus, it was possible to find roughly 10 binding sites. Most of them displayed apolar and hydrophobic features (Figure 5.9).

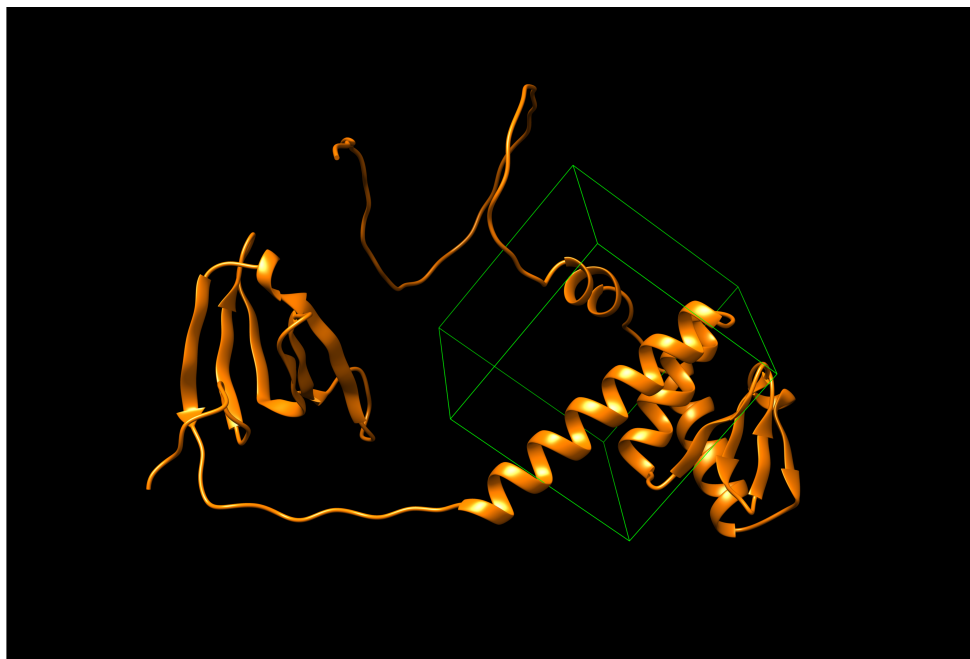


Figure 5.6: The green cube containing one of the putative binding sites of LSM12 protein.

After the coordinates were found with Chimera, AutoDockVina was run to discover potential drug candidates. At the end of the molecular docking evaluation, some molecules of the dataset showed a good fit with a particular binding site (shown in green in **Figure 5.10**).

The subset molecules potential candidates must go through another screening. This is due to the fact that the molecules can have a very high affinity while having rotation within the pocket. If a compound can change its position inside a binding site, this means that it's not really linked to. The screening process was carried on by eye using PyMol. Since it is able to display in different conformations of the drug inside the pocket, it is possible to distinguish between a good and a bad candidate just looking at it. Within all the compounds that were selected after the docking study, only one was found to have all the proper features to be considered for further studies: Di-indolyl-methane is a natural compound that can be found in cruciferous vegetables[189], such as broccoli, Brussel sprout and cabbage. It is used to treat recurrent respiratory papillomatosis[190] and some studies showed its potential role in the prevention of a variety of cancers, such as prostate and breast[191]. Di-indolyl-methane is made by two Indolyl linked to each other by a carbon. The presence of the two rings helps the molecule to insert inside the apolar binding site of RYR (**Figure 5.10**) and to stabilize the link via Van der Waals interactions (**Figure 5.11A and B**). They also lead to a high affinity for the complex (**Figure 5.11C**).

After identifying a promising candidate, evaluate its binding affinity and identifying its link with the target protein, the last step is to characterize its ADME. SwisADME was used to discover as many information as possible on Di-indolyl-methane (**Figure 5.12A**). This program shows not only the physiochemical properties (molecular weight, number of heavy atoms ... etc), but also lipophilicity, water solubility, pharmacokinetics and druglikeness. This is key information for the subsequent in vitro testing and can give a preliminary idea of the ways of administration and pos-

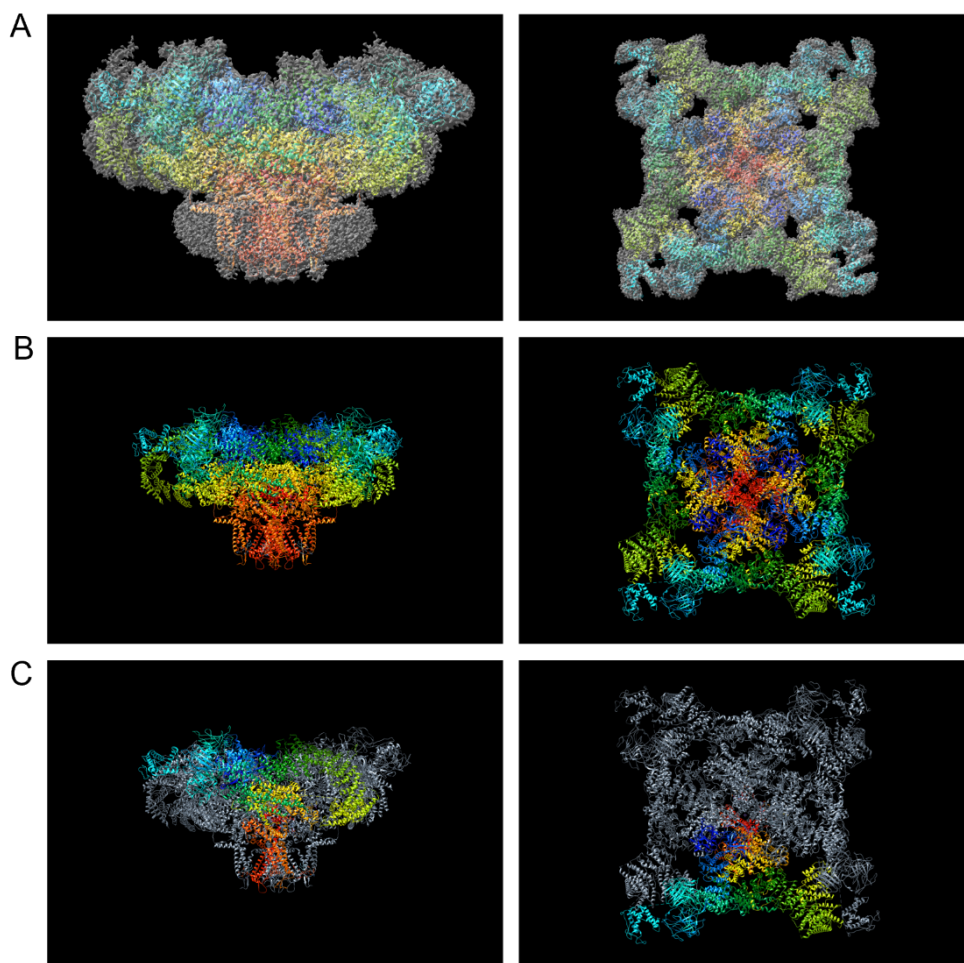


Figure 5.7: RYR1 structure shown as (A) surface (grey) and backbone (rainbow), (B) plain backbone and (C) monomer (rainbow).

sible drawbacks.

Another useful feature of Swiss website is SwissSimilarity. This feature allows to find compound with a similar structure to the one of interest and gives information on their characteristics (Figure 5.12B). These results can broaden the number of candidates to test in vitro.

In conclusion, only one candidate was selected to interact in Ca^{2+} release pathway in T cells: Di-indolyl-methane. This drug specifically interacts with the ER receptor RYR1, binding to the protein in the transmembrane region.

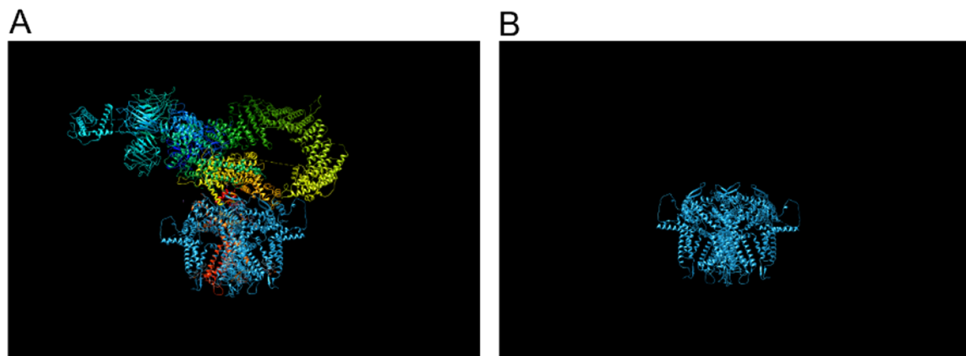


Figure 5.8: RYR1 transmembrane domain (in blue) shown (A) in relation with the monomer (rainbow) and (B) by itself.

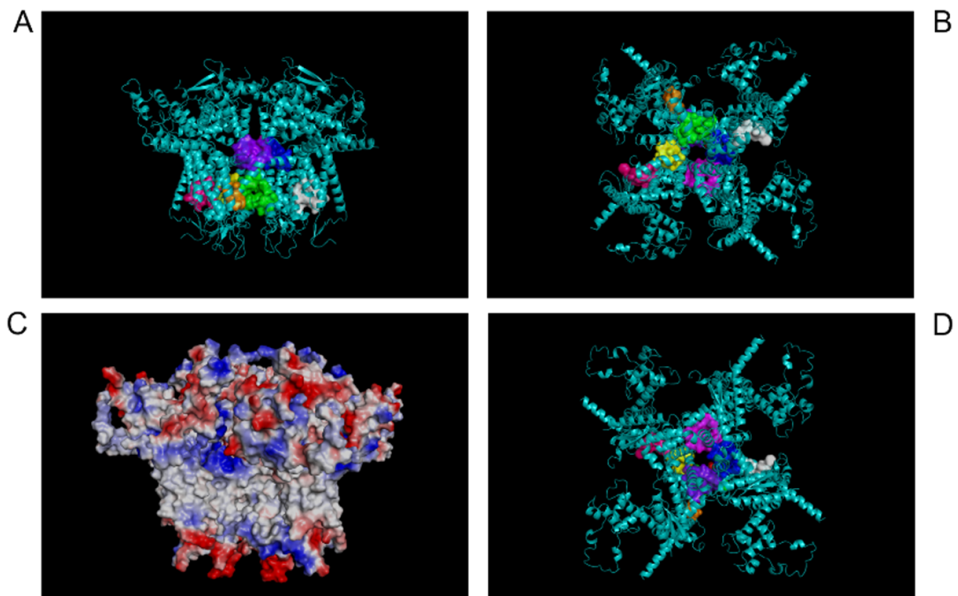


Figure 5.9: Potential binding sites in RYR1 transdomain (A, B and C) and charge distribution (C).

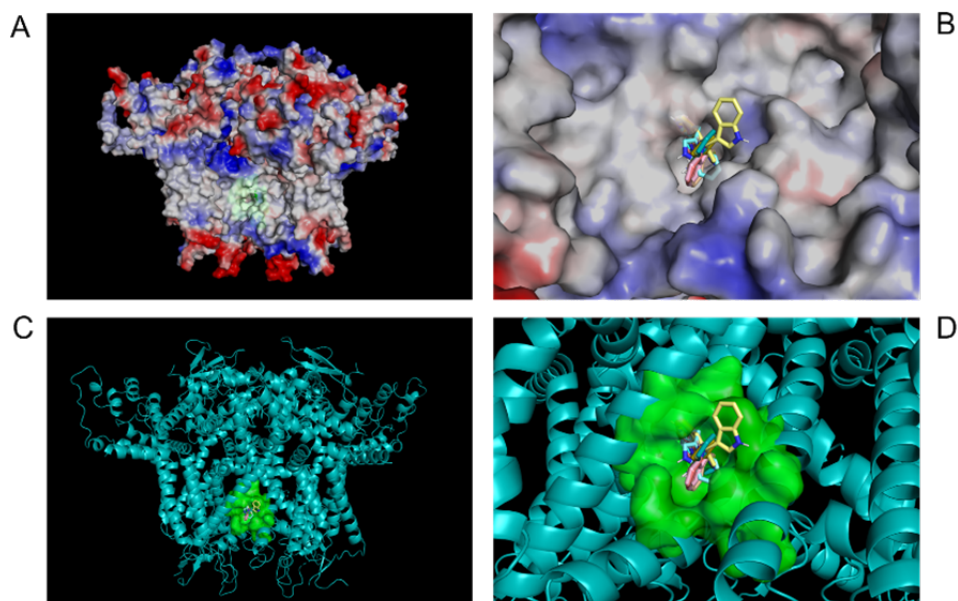


Figure 5.10: Potential drug candidates inside the binding site shown as (A and B) charged surface or (C and D) backbones.

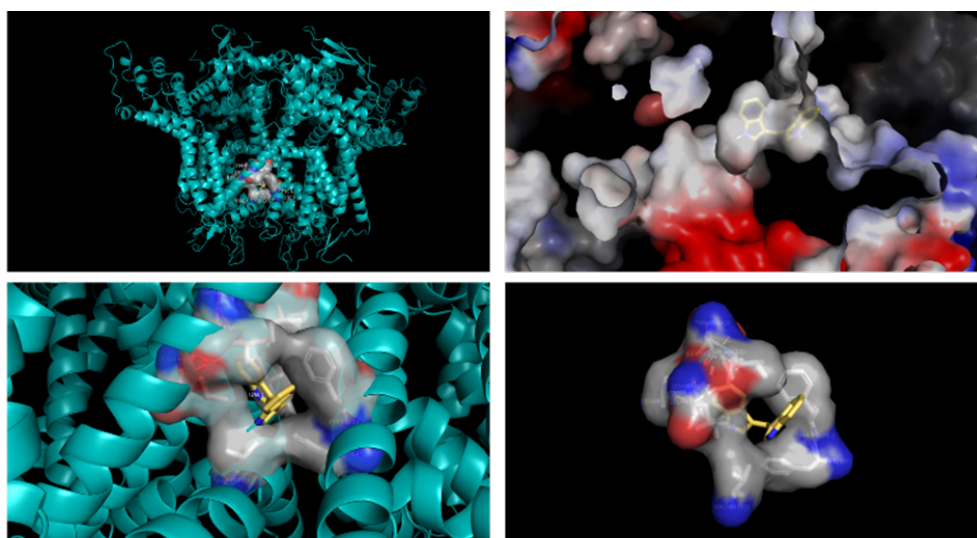


Figure 5.11: Representation of Di-indolyl-methane inside the binding site of RYR1.

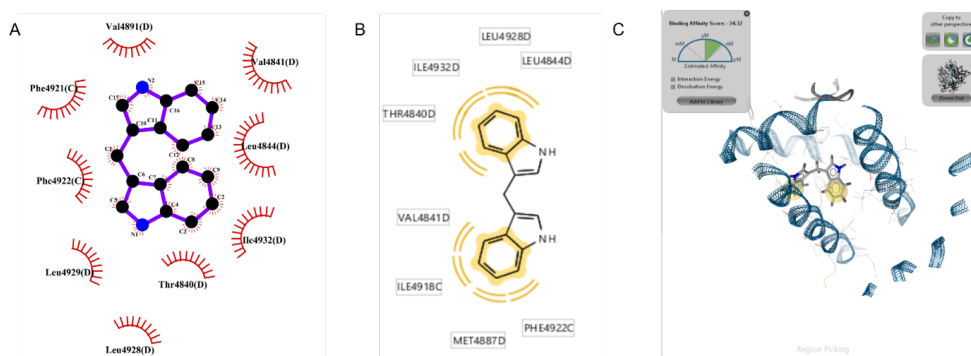


Figure 5.12: Di-indolyl-methane binding with RYR1 pocket. The residues involved in the Van der Waals interactions are shown using (A) LigPlot or (B) LigandScout programs. LigandScout is also able to (C) evaluate the binding affinity of the compound.

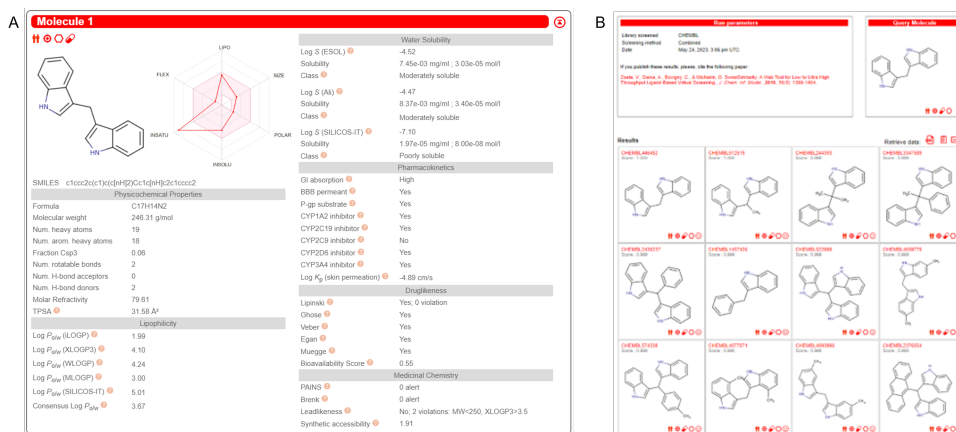


Fig. 12 SwissADME (A) and SwissSimilarity (B) results obtain for Di-indolyl-methane .

Figure 5.13: (A) SwissADME and (B) SwissSimilarity results obtained for Di-indolyl-methane.

Bibliography

- [1] Fabbri M, Smart C, Pardi R. T lymphocytes. *The international journal of biochemistry & cell biology*. 2003;35(7):1004-8.
- [2] Kumar BV, Connors TJ, Farber DL. Human T cell development, localization, and function throughout life. *Immunity*. 2018;48(2):202-13.
- [3] Boehmer H. The developmental biology of T lymphocytes. *Annual review of immunology*. 1988;6(1):309-26.
- [4] Starr TK, Jameson SC, Hogquist KA. Positive and negative selection of T cells. *Annual review of immunology*. 2003;21(1):139-76.
- [5] LaRosa DF, Orange JS. 1. Lymphocytes. *Journal of Allergy and Clinical Immunology*. 2008;121(2):S364-9.
- [6] Bromley SK, Burack WR, Johnson KG, Somersalo K, Sims TN, Sumen C, et al. The immunological synapse. *Annual review of immunology*. 2001;19(1):375-96.
- [7] Wells AD. New insights into the molecular basis of T cell anergy: anergy factors, avoidance sensors, and epigenetic imprinting. *The Journal of Immunology*. 2009;182(12):7331-41.
- [8] Adams NM, Grassmann S, Sun JC. Clonal expansion of innate and adaptive lymphocytes. *Nature Reviews Immunology*. 2020;20(11):694-707.
- [9] Luckheeram RV, Zhou R, Verma AD, Xia B, et al. CD4+ T cells: differentiation and functions. *Journal of Immunology Research*. 2012;2012.
- [10] Prete GD. Human Th1 and Th2 lymphocytes: their role in the pathophysiology of atopy. *Allergy*. 1992;47(5):450-5.
- [11] Sokol CL, Chu NQ, Yu S, Nish SA, Laufer TM, Medzhitov R. Basophils function as antigen-presenting cells for an allergen-induced T helper type 2 response. *Nature immunology*. 2009;10(7):713-20.
- [12] Annunziato F, Cosmi L, Santarlasci V, Maggi L, Liotta F, Mazzinghi B, et al. Phenotypic and functional features of human Th17 cells. *The Journal of experimental medicine*. 2007;204(8):1849-61.
- [13] Weaver CT, Harrington LE, Mangan PR, Gavrieli M, Murphy KM. Th17: an effector CD4 T cell lineage with regulatory T cell ties. *Immunity*. 2006;24(6):677-88.

- [14] Ivanov II, McKenzie BS, Zhou L, Tadokoro CE, Lepelley A, Lafaille JJ, et al. The orphan nuclear receptor ROR γ t directs the differentiation program of proinflammatory IL-17+ T helper cells. *Cell*. 2006;126(6):1121-33.
- [15] Fujio K, Okamura T, Yamamoto K. The Family of IL-10-secreting CD4+ T cells. *Advances in immunology*. 2010;105:99-130.
- [16] Valencia X, Lipsky PE. CD4+ CD25+ FoxP3+ regulatory T cells in autoimmune diseases. *Nature clinical practice Rheumatology*. 2007;3(11):619-26.
- [17] Jameson SC, Masopust D. Understanding subset diversity in T cell memory. *Immunity*. 2018;48(2):214-26.
- [18] Pennock ND, White JT, Cross EW, Cheney EE, Tamburini BA, Kedl RM. T cell responses: naive to memory and everything in between. *Advances in physiology education*. 2013;37(4):273-83.
- [19] Kim HR, Mun Y, Lee KS, Park YJ, Park JS, Park JH, et al. T cell microvilli constitute immunological synaptosomes that carry messages to antigen-presenting cells. *Nature communications*. 2018;9(1):3630.
- [20] Kono M, Takagi Y, Kawauchi S, Wada A, Morikawa T, Funakoshi K. Non-activated T and B lymphocytes become morphologically distinguishable after detergent treatment. *Cytometry Part A*. 2013;83(4):396-402.
- [21] Abraham RT, Weiss A. Jurkat T cells and development of the T-cell receptor signalling paradigm. *Nature reviews immunology*. 2004;4(4):301-8.
- [22] Hansen JA, Martin PJ, Nowinski RC. Monoclonal antibodies identifying a novel T-cell antigen and Ia antigens of human lymphocytes. *Immunogenetics*. 1980;10:247-60.
- [23] Martin P, Hansen J, Siadak A, Nowinski R. Monoclonal antibodies recognizing normal human T lymphocytes and malignant human B lymphocytes: a comparative study. *Journal of immunology (Baltimore, Md: 1950)*. 1981;127(5):1920-3.
- [24] Weiss A, Wiskocil RL, Stobo J. The role of T3 surface molecules in the activation of human T cells: a two-stimulus requirement for IL 2 production reflects events occurring at a pre-translational level. *Journal of immunology (Baltimore, Md: 1950)*. 1984;133(1):123-8.
- [25] Luan S, Wang C. Calcium signaling mechanisms across kingdoms. *Annual Review of Cell and Developmental Biology*. 2021;37:311-40.
- [26] Clapham DE. Calcium signaling. *Cell*. 2007;131(6):1047-58.
- [27] Eisner DA, Caldwell JL, Kistamás K, Trafford AW. Calcium and excitation-contraction coupling in the heart. *Circulation research*. 2017;121(2):181-95.
- [28] Gunter TE, Yule DI, Gunter KK, Eliseev RA, Salter JD. Calcium and mitochondria. *FEBS letters*. 2004;567(1):96-102.
- [29] Patergnani S, Danese A, Bouhamida E, Aguiari G, Previati M, Pinton P, et al. Various aspects of calcium signaling in the regulation of apoptosis, autophagy, cell proliferation, and cancer. *International journal of molecular sciences*. 2020;21(21):8323.

- [30] Puri BK. Calcium signaling and gene expression. *Calcium Signaling*. 2020;537-45.
- [31] Bootman MD, Bultynck G. Fundamentals of cellular calcium signaling: a primer. *Cold Spring Harbor perspectives in biology*. 2020;12(1):a038802.
- [32] Orrenius S, Zhivotovsky B, Nicotera P. Regulation of cell death: the calcium–apoptosis link. *Nature reviews Molecular cell biology*. 2003;4(7):552-65.
- [33] Mekahli D, Bultynck G, Parys JB, De Smedt H, Missiaen L. Endoplasmic-reticulum calcium depletion and disease. *Cold Spring Harbor perspectives in biology*. 2011;3(6):a004317.
- [34] Giorgi C, Danese A, Missiroli S, Patergnani S, Pinton P. Calcium dynamics as a machine for decoding signals. *Trends in cell biology*. 2018;28(4):258-73.
- [35] Cooper D, Dimri M. *Biochemistry, calcium channels*. 2020.
- [36] Bagur R, Hajnóczky G. Intracellular Ca²⁺ sensing: its role in calcium homeostasis and signaling. *Molecular cell*. 2017;66(6):780-8.
- [37] Badou A, Jha MK, Matza D, Mehal WZ, Freichel M, Flockerzi V, et al. Critical role for the β regulatory subunits of Cav channels in T lymphocyte function. *Proceedings of the National Academy of Sciences*. 2006;103(42):15529-34.
- [38] Wang H, Zhang X, Xue L, Xing J, Jouvin MH, Putney JW, et al. Low-voltage-activated CaV3.1 calcium channels shape T helper cell cytokine profiles. *Immunity*. 2016;44(4):782-94.
- [39] Calì T, Brini M, Carafoli E. Regulation of cell calcium and role of plasma membrane calcium ATPases. *International Review of Cell and Molecular Biology*. 2017;332:259-96.
- [40] Stafford N, Wilson C, Oceandy D, Neyses L, Cartwright EJ. The plasma membrane calcium ATPases and their role as major new players in human disease. *Physiological reviews*. 2017;97(3):1089-125.
- [41] Chemaly ER, Troncone L, Lebeche D. SERCA control of cell death and survival. *Cell calcium*. 2018;69:46-61.
- [42] Trebak M, Kinet JP. Calcium signalling in T cells. *Nature Reviews Immunology*. 2019;19(3):154-69.
- [43] Smith-Garvin JE, Koretzky GA, Jordan MS. T cell activation. *Annual review of immunology*. 2009;27:591-619.
- [44] Genot E, Cantrell DA. Ras regulation and function in lymphocytes. *Current opinion in immunology*. 2000;12(3):289-94.
- [45] Vallabhapurapu S, Karin M. Regulation and function of NF- κ B transcription factors in the immune system. *Annual review of immunology*. 2009;27:693-733.
- [46] Brandman O, Liou J, Park WS, Meyer T. STIM2 is a feedback regulator that stabilizes basal cytosolic and endoplasmic reticulum Ca²⁺ levels. *Cell*. 2007;131(7):1327-39.
- [47] Lunz V, Romanin C, Frischauf I. STIM1 activation of Orai1. *Cell calcium*. 2019;77:29-38.

- [48] Prakriya M, Lewis RS. Store-operated calcium channels. *Physiological reviews*. 2015.
- [49] Chin D, Means AR. Calmodulin: a prototypical calcium sensor. *Trends in cell biology*. 2000;10(8):322-8.
- [50] Gwack Y, Feske S, Srikanth S, Hogan PG, Rao A. Signalling to transcription: store-operated Ca²⁺ entry and NFAT activation in lymphocytes. *Cell calcium*. 2007;42(2):145-56.
- [51] Fracchia KM, Pai C, Walsh CM. Modulation of T cell metabolism and function through calcium signaling. *Frontiers in immunology*. 2013;4:62975.
- [52] Joseph N, Reicher B, Barda-Saad M. The calcium feedback loop and T cell activation: how cytoskeleton networks control intracellular calcium flux. *Biochimica et Biophysica Acta (BBA)-Biomembranes*. 2014;1838(2):557-68.
- [53] Kirichok Y, Krapivinsky G, Clapham DE. The mitochondrial calcium uniporter is a highly selective ion channel. *Nature*. 2004;427(6972):360-4.
- [54] Gilbert JA, Parekh AB. Respiring mitochondria determine the pattern of activation and inactivation of the store-operated Ca²⁺ current ICRAC. *The EMBO journal*. 2000.
- [55] Gilbert JA, Bakowski D, Parekh AB. Energized mitochondria increase the dynamic range over which inositol 1, 4, 5-trisphosphate activates store-operated calcium influx. *The EMBO Journal*. 2001.
- [56] Dimeloe S, Burgener AV, Grählert J, Hess C. T-cell metabolism governing activation, proliferation and differentiation; a modular view. *Immunology*. 2017;150(1):35-44.
- [57] Wang YH, Tao AY, Vaeth M, Feske S. Calcium regulation of T cell metabolism. *Current opinion in physiology*. 2020;17:207-23.
- [58] Ledderose C, Bao Y, Lidicky M, Zipperle J, Li L, Strasser K, et al. Mitochondria are gate-keepers of T cell function by producing the ATP that drives purinergic signaling. *Journal of Biological Chemistry*. 2014;289(37):25936-45.
- [59] Woehrle T, Yip L, Elkhali A, Sumi Y, Chen Y, Yao Y, et al. Pannexin-1 hemichannel-mediated ATP release together with P2X1 and P2X4 receptors regulate T-cell activation at the immune synapse. *Blood, The Journal of the American Society of Hematology*. 2010;116(18):3475-84.
- [60] Yip L, Woehrle T, Corriden R, Hirsh M, Chen Y, Inoue Y, et al. Autocrine regulation of T-cell activation by ATP release and P2X7 receptors. *The FASEB Journal*. 2009;23(6):1685.
- [61] Schenk U, Westendorf AM, Radaelli E, Casati A, Ferro M, Fumagalli M, et al. Purinergic control of T cell activation by ATP released through pannexin-1 hemichannels. *Science signaling*. 2008;1(39):ra6-6.
- [62] Schenk U, Westendorf AM, Radaelli E, Casati A, Ferro M, Fumagalli M, et al. Purinergic control of T cell activation by ATP released through pannexin-1 hemichannels. *Science signaling*. 2008;1(39):ra6-6.
- [63] Burnstock G, Boeynaems JM. Purinergic signalling and immune cells. *Purinergic signalling*. 2014;10(4):529-64.

- [64] Ruiz-Rodríguez VM, Cortes-García JD, de Jesús Briones-Espinoza M, Rodríguez-Varela E, Vega-Cárdenas M, Gómez-Otero A, et al. P2X4 receptor as a modulator in the function of P2X receptor in CD4+ T cells from peripheral blood and adipose tissue. *Molecular immunology*. 2019;112:369-77.
- [65] Junger WG. Immune cell regulation by autocrine purinergic signalling. *Nature Reviews Immunology*. 2011;11(3):201-12.
- [66] Turrens JF. Mitochondrial formation of reactive oxygen species. *The Journal of physiology*. 2003;552(2):335-44.
- [67] Sena LA, Li S, Jairaman A, Prakriya M, Ezponda T, Hildeman DA, et al. Mitochondria are required for antigen-specific T cell activation through reactive oxygen species signaling. *Immunity*. 2013;38(2):225-36.
- [68] Mak TW, Grusdat M, Duncan GS, Dostert C, Nonnenmacher Y, Cox M, et al. Glutathione primes T cell metabolism for inflammation. *Immunity*. 2017;46(4):675-89.
- [69] Premack BA, Gardner P. Signal transduction by T-cell receptors: mobilization of Ca and regulation of Ca-dependent effector molecules. *American Journal of Physiology-Cell Physiology*. 1992;263(6):C1119-40.
- [70] Carrasco MA, Hidalgo C. Calcium microdomains and gene expression in neurons and skeletal muscle cells. *Cell calcium*. 2006;40(5-6):575-83.
- [71] Scriven DR, Klimek A, Lee KL, Moore ED. The molecular architecture of calcium microdomains in rat cardiomyocytes. *Annals of the New York Academy of Sciences*. 2002;976(1):488-99.
- [72] Kunerth S, Mayr GW, Koch-Nolte F, Guse AH. Analysis of subcellular calcium signals in T-lymphocytes. *Cellular signalling*. 2003;15(8):783-92.
- [73] Alonso MT, Villalobos C, Chamero P, Alvarez J, García-Sancho J. Calcium microdomains in mitochondria and nucleus. *Cell calcium*. 2006;40(5-6):513-25.
- [74] Petersen OH, Courjaret R, Machaca K. Ca²⁺ tunnelling through the ER lumen as a mechanism for delivering Ca²⁺ entering via store-operated Ca²⁺ channels to specific target sites. *The Journal of physiology*. 2017;595(10):2999-3014.
- [75] Shuai J, Parker I. Optical single-channel recording by imaging Ca²⁺ flux through individual ion channels: theoretical considerations and limits to resolution. *Cell calcium*. 2005;37(4):283-99.
- [76] Demuro A, Parker I. Imaging single-channel calcium microdomains. *Cell calcium*. 2006;40(5-6):413-22.
- [77] Wolf IM, Guse AH. Ca²⁺ microdomains in T-lymphocytes. *Frontiers in Oncology*. 2017;7:73.
- [78] Diercks BP. The importance of Ca²⁺ microdomains for the adaptive immune response. *Biochimica et Biophysica Acta (BBA)-Molecular Cell Research*. 2024;119710.
- [79] Guse AH. NAADP signaling: New kids on the block. *Cells*. 2022;11(6):1054.

- [80] Roggenkamp HG, Khansahib I, Hernandez C LC, Zhang Y, Lodygin D, Krueger A, et al. HN1L/JPT2: A signaling protein that connects NAADP generation to Ca²⁺ microdomain formation. *Science signaling*. 2021;14(675):eabd5647.
- [81] Gunaratne GS, Brailoiu E, He S, Unterwald EM, Patel S, Slama JT, et al. Essential requirement for JPT2 in NAADP-evoked Ca²⁺ signaling. *Science signaling*. 2021;14(675):eabd5605.
- [82] Zhang J, Guan X, Shah K, Yan J. Lsm12 is an NAADP receptor and a two-pore channel regulatory protein required for calcium mobilization from acidic organelles. *Nature communications*. 2021;12(1):4739.
- [83] Gunaratne GS, Brailoiu E, Kumar S, Yuan Y, Slama JT, Walseth TF, et al. Convergent activation of two-pore channels mediated by the NAADP-binding proteins JPT2 and LSM12. *Science signaling*. 2023;16(799):eadg0485.
- [84] Saito R, Mu Q, Yuan Y, Rubio-Alarcón M, Eznarriaga M, Zhao P, et al. Convergent activation of Ca²⁺ permeability in two-pore channel 2 through distinct molecular routes. *Science signaling*. 2023;16(799):eadg0661.
- [85] Wolf IM, Diercks BP, Gattkowsky E, Czarniak F, Kempinski J, Werner R, et al. Frontrunners of T cell activation: Initial, localized Ca²⁺ signals mediated by NAADP and the type 1 ryanodine receptor. *Science Signaling*. 2015;8(398):ra102-2.
- [86] Diercks BP, Werner R, Weidemüller P, Czarniak F, Hernandez L, Lehmann C, et al. ORA1, STIM1/2, and RYR1 shape subsecond Ca²⁺ microdomains upon T cell activation. *Science signaling*. 2018;11(561):eaat0358.
- [87] Storni T, Bachmann MF. On the role of APC-activation for in vitro versus in vivo T cell priming. *Cellular immunology*. 2003;225(1):1-11.
- [88] Li Y, Kurlander RJ. Comparison of anti-CD3 and anti-CD28-coated beads with soluble anti-CD3 for expanding human T cells: differing impact on CD8 T cell phenotype and responsiveness to restimulation. *Journal of translational medicine*. 2010;8:1-15.
- [89] Abraham M, Karni A, Dembinsky A, Miller A, Gandhi R, Anderson D, et al. In vitro induction of regulatory T cells by anti-CD3 antibody in humans. *Journal of autoimmunity*. 2008;30(1-2):21-8.
- [90] Shi Y, Wu W, Wan T, Liu Y, Peng G, Chen Z, et al. Impact of polyclonal anti-CD3/CD28-coated magnetic bead expansion methods on T cell proliferation, differentiation and function. *International immunopharmacology*. 2013;15(1):129-37.
- [91] Trickett A, Kwan YL. T cell stimulation and expansion using anti-CD3/CD28 beads. *Journal of immunological methods*. 2003;275(1-2):251-5.
- [92] Chatila T, Silverman L, Miller R, Geha R. Mechanisms of T cell activation by the calcium ionophore ionomycin. *Journal of immunology (Baltimore, Md: 1950)*. 1989;143(4):1283-9.
- [93] Crawford TQ, Jalbert E, Ndhlovu LC, Barbour JD. Concomitant evaluation of PMA+ ionomycin-induced kinase phosphorylation and cytokine production in T cell subsets by flow cytometry. *Cytometry Part A*. 2014;85(3):268-76.

- [94] Pubill D, Dayanithi G, Siatka C, Andres M, Dufour MN, Guillon G, et al. ATP induces intracellular calcium increases and actin cytoskeleton disaggregation via P2x receptors. *Cell calcium*. 2001;29(5):299-309.
- [95] Berg I, Potter BV, Mayr GW, Guse AH. Nicotinic acid adenine dinucleotide phosphate (NAADP+) is an essential regulator of T-lymphocyte Ca²⁺-signaling. *The Journal of cell biology*. 2000;150(3):581-8.
- [96] Guse AH, Berg I, da Silva CP, Potter BV, Mayr GW. Ca²⁺ entry induced by cyclic ADP-ribose in intact T-lymphocytes. *Journal of Biological Chemistry*. 1997;272(13):8546-50.
- [97] Petrou T, Olsen HL, Thrasivoulou C, Masters JR, Ashmore JF, Ahmed A. Intracellular calcium mobilization in response to ion channel regulators via a calcium-induced calcium release mechanism. *Journal of Pharmacology and Experimental Therapeutics*. 2017;360(2):378-87.
- [98] Kang Y, Xu L, Dong J, Huang Y, Yuan X, Li R, et al. Calcium-based nanotechnology for cancer therapy. *Coordination Chemistry Reviews*. 2023;481:215050.
- [99] Li Y, Gong S, Pan W, Chen Y, Liu B, Li N, et al. A tumor acidity activatable and Ca²⁺-assisted immuno-nanoagent enhances breast cancer therapy and suppresses cancer recurrence. *Chemical Science*. 2020;11(28):7429-37.
- [100] Zhu D, Feng L, Feliu N, Guse AH, Parak WJ. Stimulation of local cytosolic calcium release by photothermal heating for studying intra-and intercellular calcium waves. *Advanced Materials*. 2021;33(24):2008261.
- [101] Nakatsuji H, Numata T, Morone N, Kaneko S, Mori Y, Imahori H, et al. Thermosensitive Ion Channel Activation in Single Neuronal Cells by Using Surface-Engineered Plasmonic Nanoparticles. *Angewandte Chemie International Edition*. 2015;54(40):11725-9.
- [102] Gardner P. Patch clamp studies of lymphocyte activation. *Annual review of immunology*. 1990;8(1):231-50.
- [103] Papp F, Hajdu P, Tajti G, Toth A, Nagy E, Fazekas Z, et al. Periodic membrane potential and Ca²⁺ oscillations in t cells forming an immune synapse. *International Journal of Molecular Sciences*. 2020;21(5):1568.
- [104] Bruton J, Cheng AJ, Westerblad H. Measuring Ca²⁺ in living cells. *Calcium Signaling*. 2020:7-26.
- [105] Vetter I, Carter D, Bassett J, Deuis JR, Tay B, Jami S, et al. High-throughput fluorescence assays for ion channels and GPCRs. *Calcium Signaling*. 2020:27-72.
- [106] Otten PA, London RE, Levy LA. A new approach to the synthesis of APTRA indicators. *Bioconjugate Chemistry*. 2001;12(1):76-83.
- [107] Minta A, Kao JP, Tsien RY. Fluorescent indicators for cytosolic calcium based on rhodamine and fluorescein chromophores. *Journal of Biological Chemistry*. 1989;264(14):8171-8.
- [108] Grynkiewicz G, Poenie M, Tsien RY. A new generation of Ca²⁺ indicators with greatly improved fluorescence properties. *Journal of biological chemistry*. 1985;260(6):3440-50.

- [109] Thomas D, Tovey S, Collins T, Bootman M, Berridge M, Lipp P. A comparison of fluorescent Ca²⁺ indicator properties and their use in measuring elementary and global Ca²⁺ signals. *Cell calcium*. 2000;28(4):213-23.
- [110] Kao J, Tsien RY. Ca²⁺ binding kinetics of fura-2 and azo-1 from temperature-jump relaxation measurements. *Biophysical Journal*. 1988;53(4):635-9.
- [111] Naraghi M. T-jump study of calcium binding kinetics of calcium chelators. *Cell calcium*. 1997;22(4):255-68.
- [112] Paredes RM, Etzler JC, Watts LT, Zheng W, Lechleiter JD. Chemical calcium indicators. *Methods*. 2008;46(3):143-51.
- [113] Gee KR, Brown K, Chen WU, Bishop-Stewart J, Gray D, Johnson I. Chemical and physiological characterization of fluo-4 Ca²⁺-indicator dyes. *Cell calcium*. 2000;27(2):97-106.
- [114] Lattanzio Jr FA. The effects of pH and temperature on fluorescent calcium indicators as determined with Chelex-100 and EDTA buffer systems. *Biochemical and biophysical research communications*. 1990;171(1):102-8.
- [115] O'Connor N, Silver RB. Ratio imaging: practical considerations for measuring intracellular Ca²⁺ and pH in living cells. In: *Methods in cell biology*. vol. 114. Elsevier; 2013. p. 387-406.
- [116] Lohr C. Monitoring neuronal calcium signalling using a new method for ratiometric confocal calcium imaging. *Cell calcium*. 2003;34(3):295-303.
- [117] Dustin LB. Ratiometric analysis of calcium mobilization. *Clinical and Applied Immunology Reviews*. 2000;1(1):5-15.
- [118] Morgan AJ, Thomas AP. Single-Cell and Subcellular Measurement of Intracellular Ca²⁺ Concentration. *Calcium Signaling Protocols*. 2005:87-117.
- [119] Floto R, Mahaut-Smith M, Somasundaram B, Allen J. IgG-induced Ca²⁺ oscillations in differentiated U937 cells; a study using laser scanning confocal microscopy and co-loaded fluo-3 and fura-red fluorescent probes. *Cell Calcium*. 1995;18(5):377-89.
- [120] Palmer AE, Jin C, Reed JC, Tsien RY. Bcl-2-mediated alterations in endoplasmic reticulum Ca²⁺ analyzed with an improved genetically encoded fluorescent sensor. *Proceedings of the National Academy of Sciences*. 2004;101(50):17404-9.
- [121] Perry JL, Ramachandran NK, Utama B, Hyser JM. Use of genetically-encoded calcium indicators for live cell calcium imaging and localization in virus-infected cells. *Methods*. 2015;90:28-38.
- [122] Mank M, Griesbeck O. Genetically encoded calcium indicators. *Chemical reviews*. 2008;108(5):1550-64.
- [123] Li ES, Saha MS. Optimizing calcium detection methods in animal systems: a sandbox for synthetic biology. *Biomolecules*. 2021;11(3):343.
- [124] Bird GS, DeHaven WI, Smyth JT, Putney Jr JW. Methods for studying store-operated calcium entry. *Methods*. 2008;46(3):204-12.

- [125] Gomes B, Cabral MD, Gallard A, Savignac M, Paulet P, Druet P, et al. Calcium channel blocker prevents T helper type 2 cell-mediated airway inflammation. *American journal of respiratory and critical care medicine*. 2007;175(11):1117-24.
- [126] Wu L, Lin W, Liao Q, Wang H, Lin C, Tang L, et al. Calcium channel blocker nifedipine suppresses colorectal cancer progression and immune escape by preventing NFAT2 nuclear translocation. *Cell reports*. 2020;33(4).
- [127] Veytia-Bucheli JI, Alvarado-Velázquez DA, Possani LD, González-Amaro R, Rosenstein Y. The Ca²⁺ channel blocker verapamil inhibits the in vitro activation and function of T lymphocytes: A 2022 Reappraisal. *Pharmaceutics*. 2022;14(7):1478.
- [128] Birx DL, Berger M, Fleisher TA. The interference of T cell activation by calcium channel blocking agents. *Journal of immunology (Baltimore, Md: 1950)*. 1984;133(6):2904-9.
- [129] Bourne G, Trifaró J. The gadolinium ion: a potent blocker of calcium channels and catecholamine release from cultured chromaffin cells. *Neuroscience*. 1982;7(7):1615-22.
- [130] Romano-Silva M, Gomez M, Brammer M. The use of gadolinium to investigate the relationship between Ca²⁺ influx and glutamate release in rat cerebrocortical synaptosomes. *Neuroscience letters*. 1994;178(1):155-8.
- [131] Waldherr L, Tiffner A, Mishra D, Sallinger M, Schober R, Frischauf I, et al. Blockage of store-operated Ca²⁺ influx by Synta66 is mediated by direct inhibition of the Ca²⁺ selective Orai1 pore. *Cancers*. 2020;12(10):2876.
- [132] Dynes JL, Amcheslavsky A, Cahalan MD. Genetically targeted single-channel optical recording reveals multiple Orai1 gating states and oscillations in calcium influx. *Proceedings of the National Academy of Sciences*. 2016;113(2):440-5.
- [133] Putney JW. Pharmacology of capacitative calcium entry. *Molecular Interventions*. 2001;1(2):84.
- [134] Lytton J, Westlin M, Hanley MR. Thapsigargin inhibits the sarcoplasmic or endoplasmic reticulum Ca-ATPase family of calcium pumps. *Journal of Biological Chemistry*. 1991;266(26):17067-71.
- [135] Zhao J, Pinchuk AO, McMahon JM, Li S, Ausman LK, Atkinson AL, et al. Methods for describing the electromagnetic properties of silver and gold nanoparticles. *Accounts of chemical research*. 2008;41(12):1710-20.
- [136] Huang X, El-Sayed MA. Gold nanoparticles: Optical properties and implementations in cancer diagnosis and photothermal therapy. *Journal of advanced research*. 2010;1(1):13-28.
- [137] Xia Y, Halas NJ. Shape-controlled synthesis and surface plasmonic properties of metallic nanostructures. *MRS bulletin*. 2005;30(5):338-48.
- [138] Lu X, Rycenga M, Skrabalak SE, Wiley B, Xia Y. Chemical synthesis of novel plasmonic nanoparticles. *Annual review of physical chemistry*. 2009;60:167-92.

- [139] Xia Y, Campbell DJ. Plasmons: why should we care? *Journal of chemical education*. 2007;84(1):91.
- [140] Chen Y, Ming H. Review of surface plasmon resonance and localized surface plasmon resonance sensor. *Photonic Sensors*. 2012;2:37-49.
- [141] Petryayeva E, Krull UJ. Localized surface plasmon resonance: Nanostructures, bioassays and biosensing—A review. *Analytica chimica acta*. 2011;706(1):8-24.
- [142] Chang H, Rho WY, Son BS, Kim J, Lee SH, Jeong DH, et al. Plasmonic Nanoparticles: Basics to Applications (I). *Nanotechnology for Bioapplications*. 2021:133-59.
- [143] Njoki PN, Lim IIS, Mott D, Park HY, Khan B, Mishra S, et al. Size correlation of optical and spectroscopic properties for gold nanoparticles. *The Journal of Physical Chemistry C*. 2007;111(40):14664-9.
- [144] Alvarez-Puebla R, Liz-Marzán LM, García de Abajo FJ. Light concentration at the nanometer scale. *The Journal of Physical Chemistry Letters*. 2010;1(16):2428-34.
- [145] Rodrigues MS, Borges J, Lopes C, Pereira RM, Vasilevskiy MI, Vaz F. Gas sensors based on localized surface plasmon resonances: Synthesis of oxide films with embedded metal nanoparticles, theory and simulation, and sensitivity enhancement strategies. *Applied Sciences*. 2021;11(12):5388.
- [146] El-Sayed MA. Some interesting properties of metals confined in time and nanometer space of different shapes. *Accounts of chemical research*. 2001;34(4):257-64.
- [147] Kelly KL, Coronado E, Zhao LL, Schatz GC. The optical properties of metal nanoparticles: the influence of size, shape, and dielectric environment. *The Journal of Physical Chemistry B*. 2003;107(3):668-77.
- [148] Burda C, Chen X, Narayanan R, El-Sayed MA. Chemistry and properties of nanocrystals of different shapes. *Chemical reviews*. 2005;105(4):1025-102.
- [149] Sivis M, Pazos-Perez N, Yu R, Alvarez-Puebla R, García de Abajo FJ, Ropers C. Continuous-wave multiphoton photoemission from plasmonic nanostars. *Communications Physics*. 2018;1(1):13.
- [150] Liebrau M, Sivis M, Feist A, Lourenço-Martins H, Pazos-Pérez N, Alvarez-Puebla RA, et al. Spontaneous and stimulated electron–photon interactions in nanoscale plasmonic near fields. *Light: Science & Applications*. 2021;10(1):82.
- [151] Deveci P. Synthesis, optical properties and phototherapy applications of gold nanostars. *Journal of Inclusion Phenomena and Macrocyclic Chemistry*. 2021;99(1):23-31.
- [152] Mehre A, Chaure NB. Precisely controlled shape and size of gold nanostructures by seed-mediated reduction reaction method. *Applied Physics A*. 2020;126:1-14.
- [153] Bigall NC, Haertling T, Klose M, Simon P, Eng LM, Eychmueller A. Monodisperse platinum nanospheres with adjustable diameters from 10 to 100 nm: synthesis and distinct optical properties. *Nano letters*. 2008;8(12):4588-92.

- [154] Barbosa S, Agrawal A, Rodríguez-Lorenzo L, Pastoriza-Santos I, Alvarez-Puebla RA, Kornowski A, et al. Tuning size and sensing properties in colloidal gold nanostars. *Langmuir*. 2010;26(18):14943-50.
- [155] Barnard AS, Young NP, Kirkland AI, Van Huis MA, Xu H. Nanogold: a quantitative phase map. *ACS nano*. 2009;3(6):1431-6.
- [156] Nehl CL, Liao H, Hafner JH. Optical properties of star-shaped gold nanoparticles. *Nano letters*. 2006;6(4):683-8.
- [157] De Silva Indrasekara AS, Johnson SF, Odion RA, Vo-Dinh T. Manipulation of the geometry and modulation of the optical response of surfactant-free gold nanostars: a systematic bottom-up synthesis. *Acs Omega*. 2018;3(2):2202-10.
- [158] Khlebtsov B, Panfilova E, Khanadeev V, Khlebtsov N. Improved size-tunable synthesis and SERS properties of Au nanostars. *Journal of nanoparticle research*. 2014;16:1-12.
- [159] Gherman A, Boca S, Vulpoi A, Cristea M, Farcau C, Tosa V. Plasmonic photothermal heating of gold nanostars in a real-size container: Multiscale modelling and experimental study. *Nanotechnology*. 2020;31(12):125701.
- [160] Cui X, Ruan Q, Zhuo X, Xia X, Hu J, Fu R, et al. Photothermal nanomaterials: a powerful light-to-heat converter. *Chemical Reviews*. 2023;123(11):6891-952.
- [161] Schulz F, Homolka T, Bastus NG, Puntès V, Weller H, Vossmeier T. Little adjustments significantly improve the Turkevich synthesis of gold nanoparticles. *Langmuir*. 2014;30(35):10779-84.
- [162] Schindelin J, Arganda-Carreras I, Frise E, Kaynig V, Longair M, Pietzsch T, et al. Fiji: an open-source platform for biological-image analysis. *Nature methods*. 2012;9(7):676-82.
- [163] Gasser A, Glassmeier G, Fliegert R, Langhorst MF, Meinke S, Hein D, et al. Activation of T cell calcium influx by the second messenger ADP-ribose. *Journal of Biological Chemistry*. 2006;281(5):2489-96.
- [164] Dammermann W, Zhang B, Nebel M, Cordiglieri C, Odoardi F, Kirchberger T, et al. NAADP-mediated Ca²⁺ signaling via type 1 ryanodine receptor in T cells revealed by a synthetic NAADP antagonist. *Proceedings of the National Academy of Sciences*. 2009;106(26):10678-83.
- [165] Lamas JA, Rueda-Ruzafa L, Herrera-Pérez S. Ion channels and thermosensitivity: TRP, TREK, or both? *International journal of molecular sciences*. 2019;20(10):2371.
- [166] Bertin S, Raz E. Transient receptor potential (TRP) channels in T cells. In: *Seminars in immunopathology*. vol. 38. Springer; 2016. p. 309-19.
- [167] Acharya TK, Sahu RP, Kumar S, Kumar S, Rokade TP, Chakraborty R, et al. Function and regulation of thermosensitive ion channel TRPV4 in the immune system. In: *Current Topics in Membranes*. vol. 89. Elsevier; 2022. p. 155-88.
- [168] Lin W, Suo Y, Deng Y, Fan Z, Zheng Y, Wei X, et al. Morphological change of CD4⁺ T cell during contact with DC modulates T-cell activation by accumulation of F-actin in the immunology synapse. *BMC immunology*. 2015;16:1-15.









- [169] Negulescu PA, Krasieva TB, Khan A, Kerschbaum HH, Cahalan MD. Polarity of T cell shape, motility, and sensitivity to antigen. *Immunity*. 1996;4(5):421-30.
- [170] Waugh RE, Lomakina E, Amitrano A, Kim M. Activation effects on the physical characteristics of T lymphocytes. *Frontiers in Bioengineering and Biotechnology*. 2023;11:1175570.
- [171] Bruno A, Constantino G, Sartori L, Radi M. The in silico drug discovery toolbox: applications in lead discovery and optimization. *Current Medicinal Chemistry*. 2019;26(21):3838-73.
- [172] Zhou Y, Hou Y, Shen J, Huang Y, Martin W, Cheng F. Network-based drug repurposing for novel coronavirus 2019-nCoV/SARS-CoV-2. *Cell discovery*. 2020;6(1):14.
- [173] Cheng F, Murray JL, Rubin DH. Drug repurposing: new treatments for Zika virus infection? *Trends in molecular medicine*. 2016;22(11):919-21.
- [174] Cheng F, Hong H, Yang S, Wei Y. Individualized network-based drug repositioning infrastructure for precision oncology in the panomics era. *Briefings in bioinformatics*. 2017;18(4):682-97.
- [175] Hirano Y, Takeda K, Miki K. Charge-density analysis of an iron-sulfur protein at an ultra-high resolution of 0.48 Å. *Nature*. 2016;534(7606):281-4.
- [176] Schmidt A, Teeter M, Weckert E, Lamzin VS. Crystal structure of small protein crambin at 0.48 Å resolution. *Acta Crystallographica Section F: Structural Biology and Crystallization Communications*. 2011;67(4):424-8.
- [177] Zhou H, Luo F, Luo Z, Li D, Liu C, Li X. Programming conventional electron microscopes for solving ultrahigh-resolution structures of small and macromolecules. *Analytical chemistry*. 2019;91(17):10996-1003.
- [178] Series WTR. The Selection and Use of Essential Medicines (2019). TRS. 2019;1021.
- [179] Irwin JJ, Sterling T, Mysinger MM, Bolstad ES, Coleman RG. ZINC: a free tool to discover chemistry for biology. *Journal of chemical information and modeling*. 2012;52(7):1757-68.
- [180] Kanehisa M, Goto S. KEGG: kyoto encyclopedia of genes and genomes. *Nucleic acids research*. 2000;28(1):27-30.
- [181] Wishart DS, Feunang YD, Guo AC, Lo EJ, Marcu A, Grant JR, et al. DrugBank 5.0: a major update to the DrugBank database for 2018. *Nucleic acids research*. 2018;46(D1):D1074-82.
- [182] Tian W, Chen C, Lei X, Zhao J, Liang J. CASTp 3.0: computed atlas of surface topography of proteins. *Nucleic acids research*. 2018;46(W1):W363-7.
- [183] Zhang Z, Li Y, Lin B, Schroeder M, Huang B. Identification of cavities on protein surface using multiple computational approaches for drug binding site prediction. *Bioinformatics*. 2011;27(15):2083-8.
- [184] Pettersen EF, Goddard TD, Huang CC, Couch GS, Greenblatt DM, Meng EC, et al. UCSF Chimera—a visualization system for exploratory research and analysis. *Journal of computational chemistry*. 2004;25(13):1605-12.

- [185] Morris GM, Huey R, Lindstrom W, Sanner MF, Belew RK, Goodsell DS, et al. AutoDock4 and AutoDockTools4: Automated docking with selective receptor flexibility. *Journal of computational chemistry*. 2009;30(16):2785-91.
- [186] Trott O, Olson AJ. AutoDock Vina: improving the speed and accuracy of docking with a new scoring function, efficient optimization, and multithreading. *Journal of computational chemistry*. 2010;31(2):455-61.
- [187] Vuorinen A, Schuster D. Methods for generating and applying pharmacophore models as virtual screening filters and for bioactivity profiling. *Methods*. 2015;71:113-34.
- [188] Daina A, Michielin O, Zoete V. SwissADME: a free web tool to evaluate pharmacokinetics, drug-likeness and medicinal chemistry friendliness of small molecules. *Scientific reports*. 2017;7(1):42717.
- [189] Bonnesen C, Eggleston IM, Hayes JD. Dietary indoles and isothiocyanates that are generated from cruciferous vegetables can both stimulate apoptosis and confer protection against DNA damage in human colon cell lines. *Cancer research*. 2001;61(16):6120-30.
- [190] Wiatrak BJ. Overview of recurrent respiratory papillomatosis. *Current opinion in otolaryngology & head and neck surgery*. 2003;11(6):433-41.
- [191] Biersack B, Schobert R. Indole compounds against breast cancer: recent developments. *Current drug targets*. 2012;13(14):1705-19.

Appendix A

List of GHS substances

Table A.1: List of chemicals and GHS classifications

Substance	Signal word	GHS-symbols	Hazard statements	Precautionary statements
Chloauric Acid	Danger		H290, H335, H314	P303+P361+P353, P305+P351+P338, P234, P261, P271, P280
Citric Acid	Warning		H319, H335	P304+P340+P312, P305+P351+P338, P261, P264, P271, P280
Ethanol	Danger		H225, H319	P305+P351+P338, P210, P233, P240, P241, P242
Ethylenediaminetetraacetic acid	Warning		H319	P305+P351+P338, P337+P313, P264, P280
Hydrochloric acid	Danger		H290, H314, H411, H302, H373	P303+P361+P353, P305+P351+P338, P260, P273, P280, P314
Silver Nitrate	Danger		H272, H314, H410, H290	P303+P361+P353, P304+P340+P310, P305+P351+P338, P210, P260, P280
Sodium Hydroxide	Danger		H290, H314	P303+P361+P353, P304+P340+P310, P305+P351+P338, P234, P260, P280
Thapsigargin	Danger		H315, H319, H334, H335	P302+P352, P305+P351+P338, P304+P340, P332+P313, P337+P313, P261

Acknowledgements

La strada è stata lunga ma sono giunta alla fine! Sono stati tre anni e mezzo infiniti e c'è tanto di cui ringraziare!

First of all, I want to thank Prof. Dr. Wolfgang Parak that give me the chance to pursue my PhD in his lab. I thank him again and Prof. Dr. Andreas Guse for their support and suggestions regarding my project. Thanks to Dr. Stefano Villa that performed all the data analysis of my thesis. I want also to thank Dr. Björn-Philipp Diercks, from Guse's group, for his constant availability to answer all my small practical questions. Thanks to Dr. Florian Schulz and Dr. Neus Feliu Torres to kindly agreed to be my assessor and member of commission, respectively. Thanks also to Prof. Dr. Thomas Devic and Prof. Dr. Patricia Horcajada and their teams to allow me to join their work for few months during my secondments in Nantes and Madrid, respectively. Thanks also to Pharmidex company and to Dr. Alejandro Peña for teaching me about in silico drug discovery. Thanks to the EU's Horizon 2020 research and innovation program, which funded my PhD.

Thanks for all my lab mates! Thanks to Juan that made possible to see my nanostars both with SEM and TEM (he said that they were beautiful, by the way!)! Thanks to the ICP-MS crew: Jili, Jinrui and Marvin. Thanks to all of you to made it possible to quantify my nanostars! A special mention to Marvin that was always there to reply to my questions about gold nanoparticles and calculations! Thanks to Martin that, not only answered to all my questions, but gossiped with me and listened to me when I complained (more than one time a day)! Thanks to Marie that helped me to split my cells and lended me the hood when I needed; I'll bring the crocheted cat with my everywhere! Thanks to Sarodi that cut out a countless amount of paper dice for our educational paper! Thanks to Hessam that shared the responsibility of the cell lab with me. Thanks also to Ben that shared the office with me. He and Hessam had no choice! I'm so sorry!. Whereas Ferdinand really wanted me to be in office with me to share anecdotes on dissertation writing! Thanks for choosing me! Thanks to Miao who was someone I could talk to during the writing of my thesis, even just to give us a bit of encouragement. Thanks to Saad, the best colleagues you can find when you start a PhD in the middle of a pandemic! You have welcomed and helped me from the very beginning, I cannot be grateful enough! Thanks to Maya and Mia that had the misfortune to have me as their supervisor and didn't plot against me! You taught me a lot about patience and how to be a better mentor!

Thanks to all of you, even if I didn't mention you directly, for your patience with my bad temper! a special thanks to whom gifted me with an animal in any form,

shape or material!!!

Thanks to all my friends near and far, new and old! You all supported me in different ways! Some of you helped to start a new life in foreign country and have had several Saturday night dinners (o tigellate) at home with me. Others didn't have the chance to see me (or hear from me) so often but they were always available for me (to gossip or complain) when I needed! Thank you all!

Thanks to all my big family! Now you can stop asking me when I'll submit my thesis!

Last, but not least, thanks a lot to my wonderful husband Stefano! I could not do it without you! From moving to another nation to analyzing all my data and making my Latex file work!!! You are truly the best and I cannot express in words how grateful I am to be married to you and to have the privilege to be your wife!

CE L'HO FATTA!

Si, Cazzo!!!!

Declaration of Authorship

Hiermit versichere ich an Eides statt, die vorliegende Dissertationsschrift selbst verfasst und keine anderen als die angegebenen Hilfsmittel und Quellen benutzt zu haben.

I hereby declare upon oath that I have written the present dissertation independently and have not used further resources and aids than those stated.

Mana Poter

Hamburg, 29.05.2024

Signature of the doctoral student